Alma Mater Studiorum · Università di Bologna

Scuola di Scienze
Dipartimento di Fisica e Astronomia
Corso di Laurea Magistrale in Fisica

Study of multiplicity dependence of J/ψ and $\psi(2\mathrm{S})$ yields and production ratios in p-p collisions at $\sqrt{s} = 7$ TeV with the CMS experiment at LHC

Relatore:
Prof. Renato Campanini

Correlatore:
Dott. Daniele Fasanella

Presentata da:
Giovanni Tenaglia

Anno Accademico 2015/2016

Sommario

La teoria dell'interazione forte, la Cromodinamica Quantistica, non è tuttora risolvibile completamente. Le sue proprietà emergenti in sistemi interagenti sono dunque il soggetto della maggior parte degli studi nella fisica degli ioni pesanti. Le collisioni protone-protone possono fornire un punto di vista alternativo su questo argomento, con differenti limitazioni ma anche differenti possibilità.
Questa tesi si propone di investigare su possibili indizi di fenomeni collettivi, come la formazione di plasma di quark e gluoni, in collisioni protone-protone. Per questo scopo, è stato effettuato uno studio sulla dipendenza dalla molteplicità delle produzioni di J/ψ and ψ(2S) e dei loro rapporti, all'energia di $\sqrt{s} = 7$ TeV nell'ambito dell'esperimento CMS al Large Hadron Collider. I risultati sono stati poi discussi e messi in relazione con altri recenti dati sperimentali.
La tesi è organizzata nel seguente modo:

- nel Capitolo 1 vengono presentate un'introduzione alla teoria della Cromodinamica Quantistica e una panoramica sulla fenomenologia del plasma di quark e gluoni;
- nel Capitolo 2 vengono introdotte le principali caratteristiche dell'esperimento CMS al Large Hadron Collider;
- nel Capitolo 3 viene descritta la valutazione dei valori di produzione di J/ψ and ψ(2S), e successivamente la separazione delle loro frazioni dirette e indirette;
- nel Capitolo 4 viene discusso il calcolo della molteplicità di tracce cariche, ovvero il numero di particelle cariche primarie prodotte nella collisione, che deve essere associato ad ogni coppia di muoni;
- nel Capitolo 5 si studia l'andamento in funzione della molteplicità carica dei valori di produzione di J/ψ and ψ(2S) e dei loro rapporti. Inoltre si studia l'andamento, sempre in funzione della moltpelicità carica, dell'impulso trasverso medio di J/ψ and ψ(2S);
- nel Capitolo 6 i risultati sono discussi e confrontati con altri recenti studi sperimentali.

Abstract

The theory of the strong interaction, Quantum Chromodynamics, is not completely solvable nowadays. Its emerging properties in interacting systems are therefore the topic of most studies in heavy-ion physics. Proton-proton collisions can provide an alternative point of view for this subject, with different limitations but also different possibilities.
This thesis aims to investigate possible clues of collective phenomena, such as the formation of Quark-Gluon Plasma, in proton-proton collisions. For this goal, study of multiplicity dependencies in J/ψ and ψ(2S) yields and production ratios in is performed, at the energy of $\sqrt{s} = 7$ TeV in the context of the CMS experiment at the Large Hadron Collider. The results have then been discussed and related to other recent experimental data.
The thesis is organized in the following way:

- in Chapter 1 the theoretical background of Quantum Chromodynamics and an introduction to Quark-Gluon Plasma phenomenology are presented;
- in Chapter 2 the main features of the CMS experiment at the LHC are presented;
- in Chapter 3 the extraction of the J/ψ and ψ(2S) yields are described, and subsequently the separation of their prompt and non-prompt fraction;
- in Chapter 4 the evaluation of charged track multiplicity is discussed, i.e. the number of primary charged particles produced in the collision, that has to be associated with each dimuon pair;
- in Chapter 5 the trend of J/ψ and ψ(2S) production yields and of their ratios as a function of charged multiplicity is studied. Moreover the trend, again as a funcion of charged multiplicity, of the average transverse momentum of J/ψ and ψ(2S) is also studied;
- in Chapter 6 the results are discussed and compared to other recent experimental studies.

Contents

Chapter 1

QCD and Quark-Gluon Plasma

In this chapter the theoretical background of Quantum Chromodynamics and an introduction to Quark-Gluon Plasma phenomenology will be presented.

1.1 The Standard Model

The Standard Model (SM) of particles and forces is a quantum field theory which describes the electromagnetic, weak and strong interactions between the elementary particles. Since an unification scale has been found between electromagnetic and weak interactions, they are both usually referred to as *electroweak force*.
Elementary particles are the point-like (up to the present experimental limit of 10^{-19} cm) constituents of matter and force carriers. All matter particles are fermions, which obey the Fermi-Dirac statistics and have half-integer spin. They are grouped into isospin doublets as they are sensitive to weak interactions; see Fig. 1.1a.
Moreover, charged leptons are sensitive to the electromagnetic force. Quarks are also affected by the strong interaction, thus they have an additional quantum number with respect to leptons, the color charge. For every fermion, a corresponding anti-particle exists, with opposite charge. The force carriers are bosons, which instead obey the Bose-Einstein statistics and have integer spin. The intermediate bosons are the carriers of the interactions. Electromagnetic interactions are mediated by photons, weak interactions are mediated by the vector bosons Z_0 and $W_{\pm}$, and strong interactions are mediated by eight gluons. A summary of the bosons is shown in Fig. 1.1b. This model aims to describe also gravitational interactions, which are thought to be mediated by the graviton, but this hypothesis is hard to test since at the energy scale of High Energy physics their effect would be negligible.
The Standard Model is based on a gauge symmetry: mathematically, every elementary particle is represented by a field, whose Lagrangian encodes all its possible interactions and is invariant under a continuous group of local transformations. The global symmetry

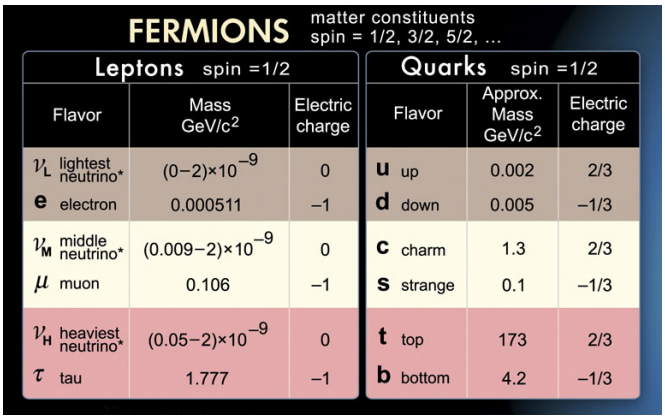

FERMIONS matter constituents spin = 1/2, 3/2, 5/2, ...

Leptons spin =1/2

Flavor	Mass GeV/c²	Electric charge
ν_L lightest neutrino*	$(0-2)\times10^{-9}$	0
e electron	0.000511	−1
ν_M middle neutrino*	$(0.009-2)\times10^{-9}$	0
μ muon	0.106	−1
ν_H heaviest neutrino*	$(0.05-2)\times10^{-9}$	0
τ tau	1.777	−1

Quarks spin =1/2

Flavor	Approx. Mass GeV/c²	Electric charge
u up	0.002	2/3
d down	0.005	−1/3
c charm	1.3	2/3
s strange	0.1	−1/3
t top	173	2/3
b bottom	4.2	−1/3

(a) The fermions of the Standard Model. Among the latter, only electrons, neutrinos and up and down quarks are stable in nature.

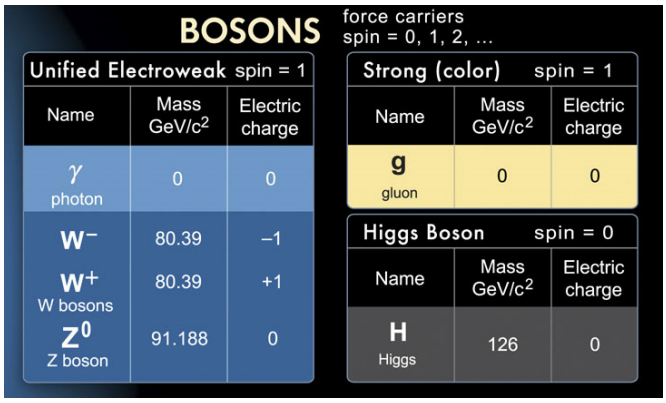

BOSONS force carriers spin = 0, 1, 2, ...

Unified Electroweak spin = 1

Name	Mass GeV/c²	Electric charge
γ photon	0	0
W^-	80.39	−1
W^+ W bosons	80.39	+1
Z^0 Z boson	91.188	0

Strong (color) spin = 1

Name	Mass GeV/c²	Electric charge
g gluon	0	0

Higgs Boson spin = 0

Name	Mass GeV/c²	Electric charge
H Higgs	126	0

(b) The bosons of the Standard Model.

Figure 1.1

group is $SU(3)_C \otimes [SU(2)_L \otimes U(1)_Y]$. This group includes:

- the three dimensional special unitary group $SU(3)_C$, where C stands for color (red, blue, green), the generator of the group, for the strong interaction;
- the two dimensional special unitary group composed with the one dimensional unitary group, $SU(2)_L \otimes U(1)_Y$, which unifies the electromagnetic and weak interactions. L indicates that this interaction affects only left-handed fermions and Y is the hypercharge, a combination of electrical charge and isospin.

1.2 Quantum Chromodynamics (QCD)

Quantum Chromodynamics (QCD) is the theory of the strong interaction. Its physical degrees of freedom are quarks and gluons, the quanta of gauge fields. The lagrangian density is:

$$L = \sum_j \overline{\Psi}_j (i\gamma_\mu \mathcal{D}^\mu - m_j)\Psi_j - \frac{1}{4} F_{a\mu\nu} F_a^{\mu\nu} \tag{1.1}$$

with

$$F_a^{\mu\nu} \equiv \partial^\mu A_a^\nu - \partial^\nu A_a^\mu - g_s f_{abc} A_b^\mu A_c^\nu \tag{1.2}$$

$$\mathcal{D}^\mu \equiv \partial^\mu + i\frac{g_s}{2} \boldsymbol{\tau}_a A_a^\mu \tag{1.3}$$

$$[\boldsymbol{\tau}^a, \boldsymbol{\tau}^b] = i f^{abc} \boldsymbol{\tau}^c \tag{1.4}$$

where the vector potential $A^\mu = A^\mu_a \boldsymbol{\tau}_a$ becomes under the gauge transformations $\Psi \to U_\omega \Psi = e^{i\frac{g_s}{2}\omega_a \boldsymbol{\tau}_a}\Psi$

$$A^\mu \to U_\omega A^\mu U^\dagger_\omega - \frac{2i}{g_s}(\partial^\mu U_\omega)U^\dagger_\omega \tag{1.5}$$

Ψ is the fermionic field bispinor triplet, m is its mass, j indicates the flavor, γ^μ are the gamma matrices, $\boldsymbol{\tau}_a$ are the generators of the fundametal representation of $SU(3)$, a, b, c are the color indices and g_s is the strong coupling constant. Aside from the quark masses, the coupling constant is the only free parameter of the theory.

QCD is structured like a generalization of Quantum Electrodynamics, with the $SU(3)$ symmetry instead of $U(1)$ and so three different kinds of charge instead of one, but there are a few crucial differences. First of all, the response of gluons to color charge, as measured by the QCD coupling constant, is much more vigorous than the response of photons to electric charge. Second, in addition to just responding to color charge, gluons can also change one color charge into another. All possible changes of this kind are allowed, as long as color charge is conserved. So the gluons themselves must be able to carry unbalanced color charges. Being coloured, gluons couple directly to each other, whereas photons do not. A consequence of the self-coupling is that the force between quarks does not vanish at large distances like electric force but grows asymptotically towards F $\approx$ 800 MeVfm^{-1} $\approx$ 15,000 N, similarly to a string tension. It would, thus, require a vast amount energy to separate quarks at a macroscopic distance. So vast that, before the separation becomes large enough, this causes the energy stored in the gluon field to "spark" into quark-antiquark pairs. This phenomenon of QCD explains why freely propagating quarks are not observed in nature, and it is called confinement. In other words this can be interpreted as the fact that in this case, unlike in electromagnetism, vacuum polarization has an antiscreening effect, it makes the coupling constant grow at longer distances; a perturbative analysis no longer makes sense once the distance is high enough. At short distances instead, or equivalently at high energies, the QCD coupling is small enough that perturbation theory can again be used and the quarks can even be considered free when bound "inside" the same particle [22].

The particles composed of quarks through the confining effect of the strong interaction are named hadrons. Hadrons are traditionally known in two topologies: those constituted by three quarks (the baryons, like protons and neutrons) and those constituted by a quark-antiquark pair (the mesons). Only recently there have been reports consistent with the observation of two other kinds of respectively baryonic and mesonic particles: the pentaquark [3] and the tetraquark [4]. The first are composed of four quarks and one antiquark, and have baryon number 1 as quarks have a baryon number of +1/3 and antiquarks of -1/3; the latter are composed of two pairs of quark and antiquark, thus they coincide with their antiparticle like all mesons.

All baryons and mesons are unstable, except for the protons, composed by two up quark and a down quark.

Outside the perturbative range, for specific problems effective theories may be developed

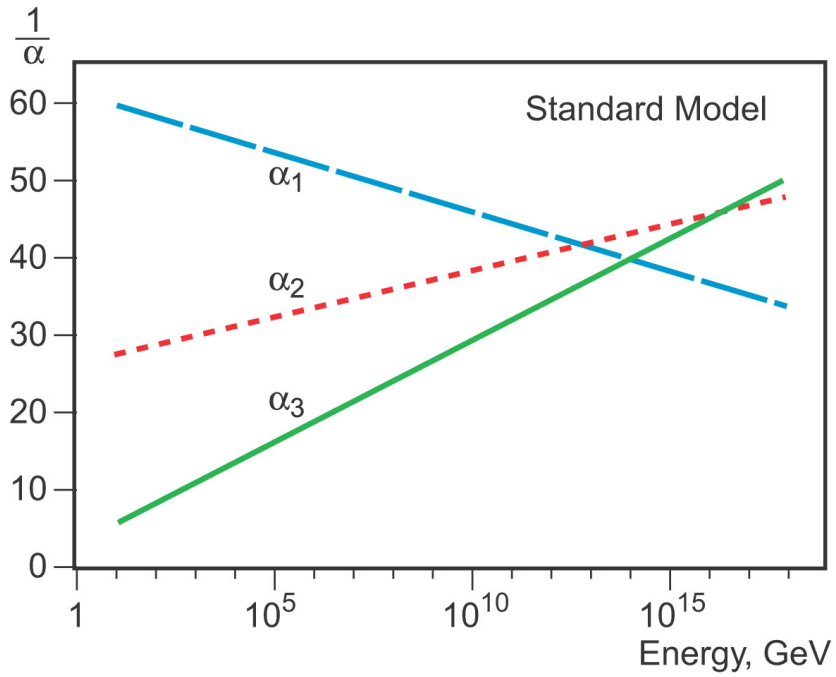

Figure 1.2: Energy dependence of the electromagnetic (α_1), weak (α_2) and strong (α_3) coupling constants

Mesons $q\bar{q}$

Mesons are bosonic hadrons.
There are about 140 types of mesons.

Symbol	Name	Quark content	Electric charge	Mass GeV/c^2	Spin
π^+	pion	$u\bar{d}$	+1	0.140	0
K^-	kaon	$s\bar{u}$	–1	0.494	0
ρ^+	rho	$u\bar{d}$	+1	0.770	1
B^0	B-zero	$d\bar{b}$	0	5.279	0
η_c	eta-c	$c\bar{c}$	0	2 .980	0

(a) The main mesons (ground states).

Baryons qqq and Antibaryons $\bar{q}\bar{q}\bar{q}$

Baryons are fermionic hadrons.
There are about 120 types of baryons.

Symbol	Name	Quark content	Electric charge	Mass GeV/c^2	Spin
p	proton	uud	1	0.938	1/2
$\bar{p}$	anti-proton	$\bar{u}\bar{u}\bar{d}$	–1	0.938	1/2
n	neutron	udd	0	0.940	1/2
Λ	lambda	uds	0	1.116	1/2
Ω^-	omega	sss	–1	1.672	3/2

(b) The main baryons (ground states).

Figure 1.3

to give qualitatively correct predictions in certain limits. In the best cases, these may then be obtained as systematic expansions in some parameter of the Lagrangian. In addition to effective theories, models like the Nambu–Jona-Lasinio model and the chiral model are often used when discussing general features.
Alternatively an approximation scheme can be used, the 1/N expansion, which starts from the premise that the number of colors is infinite, and makes a series of corrections to account for the fact that it is not. Until now, it has been the source of qualitative insight rather than a method for quantitative predictions, together with some modern variants. Moreover, one can also derive sets of relations that connect different observables with each other using an operator product expansion. But, among non-perturbative approaches to QCD, the most well established one is lattice QCD [5]. This approach uses a lattice of spacetime points to reduce the analytically intractable path integrals of the continuum theory to a numerical computation which can then be carried out on supercomputers. While it is a slow and resource-intensive approach, it has wide applicability, giving insight into parts of the theory inaccessible by other means, in particular into the explicit forces acting between quarks and antiquarks in a meson. However, the numerical sign problem, due to the presence of negative weights in the calculation of thermal averages [6], makes it difficult to use lattice methods to study QCD at high density and low temperature (e.g. nuclear matter or the interior of neutron stars).
It is according to some lattice calculations that appears that, if matter density and temperature become high enough, hadrons constituents become free to roam the system without being confined inside the original particle. This new state of matter is called a Quark-Gluon Plasma (QGP).

1.3 Quark-Gluon Plasma

The phase diagram of strongly interacting matter is shown in Fig. 1.4 as a function of temperature and net baryon density (the chemical potential μ_B). At low temperature and low density, quarks and gluons are confined into hadrons and the matter can be described as an hadronic gas. At low temperatures and high densities, the matter can be described as a degenerated gas of neutrons, and for $T \to 0$, as $\mu_B \to \infty$, the quarks are expected to begin the formation of color Cooper pairs and thus a color superconductive phase.
The typical separation between particles in a relativistic thermal system is proportional to the inverse of the temperature, and one therefore expects colored elementary constituents of hadrons to become weakly coupled at high enough temperatures (but this happens also at high densities). Hence the quarks and gluons gradually become deconfined and free to circulate forming a plasma, i.e. a colour charge conductor medium. The results from lattice QCD calculations at $\mu_B = 0$ show that the deconfinement transition occurs at a critical temperature $180 \leq T_c \leq 200$ MeV, and the corresponding critical

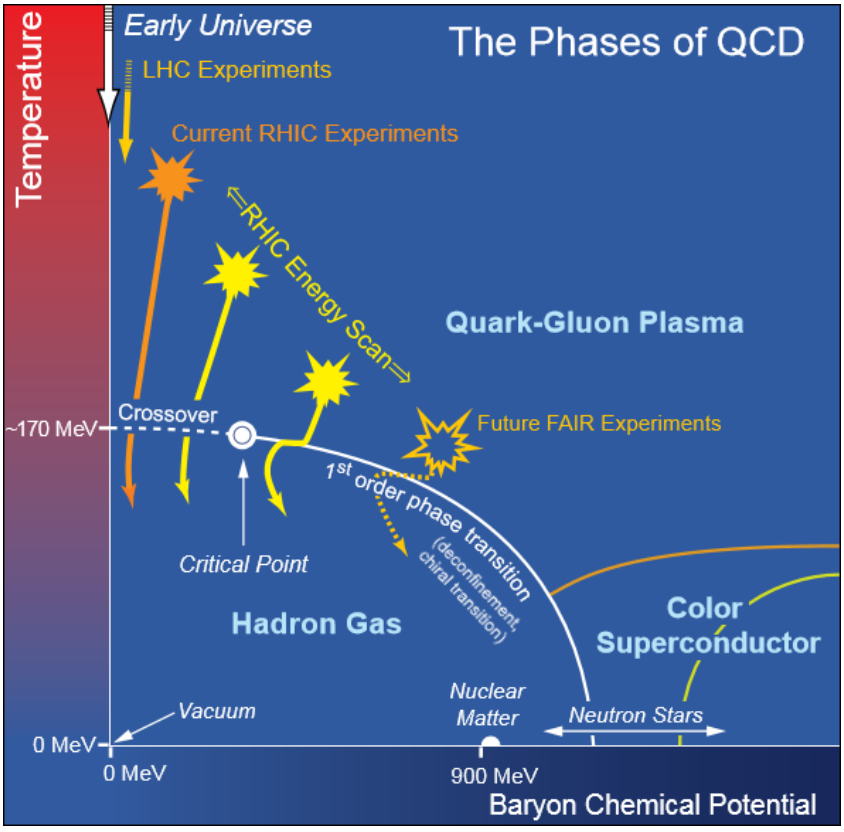

Figure 1.4: Phase diagram of QCD matter [14].

energy density has been determined to be about 0.5-1 GeV/fm^3 [10]. At higher μ_B the critical temperature is expected to be lower, as can be seen in the QCD phase diagram. Those results have also shown that the QGP does not behave as an ideal gas, since there is a residual interaction. Furthermore, the calculations also suggest that the deconfinement transition, reflected in the rapid increase of the system energy density, and a chiral phase transition, occur altogether at the same interval of temperatures. The latter is due to the negligibility of the quark masses at increasing energy densities and reflected in the sudden decrease of the chiral condensate; in fact it is the mass term in the Lagrangian, $m\bar{\Psi}\Psi = m(\bar{\Psi}_L\Psi_R + \bar{\Psi}_R\Psi_L)$ that breaks chiral symmetry explicitly. Thermodynamic calculations and lattice results [8, 40] have shown that at small or vanishing values of μ_B the deconfinement transition is not a phase transition but a continuous cross-over due to the non-zero mass of the u, d and s quarks (see Fig. 1.5).

The bulk of the matter forming a quark-gluon plasma in the central rapidity region of a

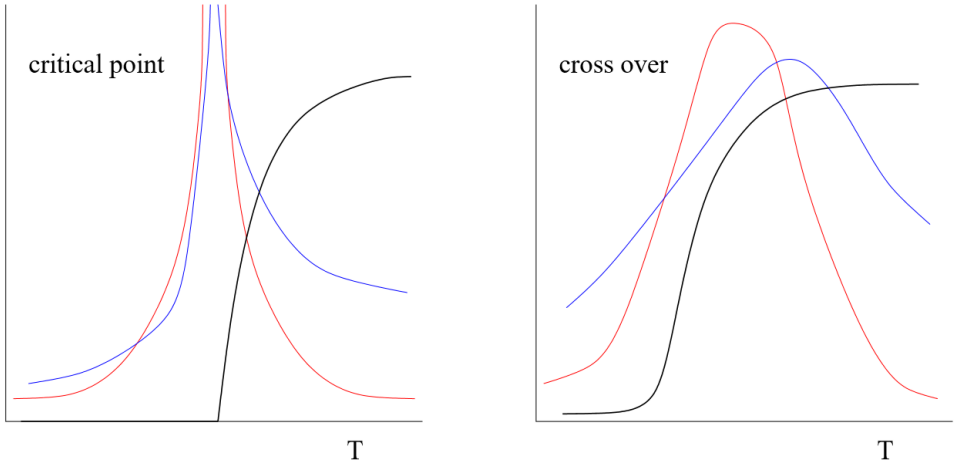

Figure 1.5: Examples of order parameters (red and blue) as a function of temperature in two different kinds of transition of a thermodynamical observable (black): first order (left) and cross-over (right). At a cross-over there are no singularities, and the order parameters may change continuously [40].

collider initially consists of gluons; even when the collision energy is large, the available phase space for gluon emissions compensates for the smallness of the coupling constant. These gluons are the result of multiple gluon emissions in an exponentially growing cascade that starts from the valence quarks. The probability to emit a gluon with a small momentum fraction x of its parent quark or gluon is parametrically $g_s\frac{dx}{x} = g_s dy$, where y is the rapidity of the gluon [8]. This cascade picture of weak coupling QCD therefore naturally leads to particles being produced in a boost-invariant way at leading order: at rapidity scales $\Delta y < \frac{1}{g_s}$ the distribution is independent of rapidity. This plateau, also seen experimentally, can be visualized as a stopping of the colliding nuclei followed by an

explosion that leads to a more isotropic distribution in the scattering angle, and leads to relatively simple solutions of the hydrodynamic equations. For momenta of the order of a characteristic momentum scale Q_s the system is dominated by the non linearities, represented by the interaction terms in the Yang-Mills Lagrangian. This typical transverse momentum scale Q_s is known as the saturation scale: below it the nonlinear interactions of gluons limit the exponential cascade of gluon emissions. At higher energies even more gluons can be emitted; the saturation scale thus grows with energy.

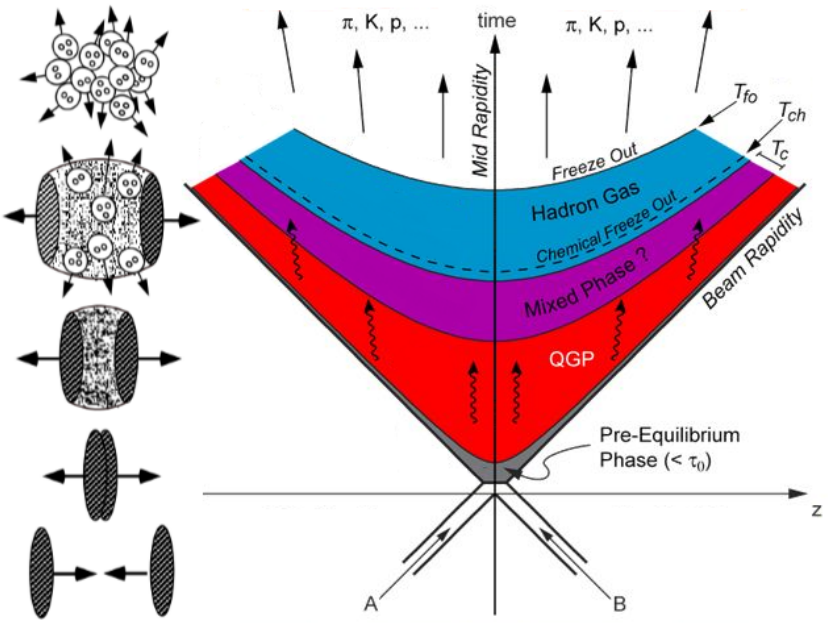

Figure 1.6: Steps in the formation of QGP. z indicates the radial direction.

Describing these relativistic collisions is a difficult task, but the so called "Bjorken scenario" [11] (considering heavy-ion collisions) highlights some stages:

1. pre-equilibrium ($0 < \tau < 1$ fm/c): in this phase, multiple interactions occur during the parton scattering, leading to the production of high-p_T and low-p_T particles;

2. thermalization ($\tau \sim 4$ fm/c): the re-scattering among quarks, gluons and particles produced during the collision, leads to a rapid increase of entropy which could eventually result in thermalization if the medium survives long enough;

3. QGP formation and hydrodynamic expansion ($1 < \tau < 10$ fm/c): assuming that the required energy density is achieved, the system reaches the deconfined phase and due to the pressure gradient between the high density medium and the surrounding vacuum the system starts to quickly expand with a "fireball". Its evolution is usually modelled according to relativistic hydrodynamics;

4. hadronization ($10 < \tau < 20$ fm/c): the expanding system cools down and below the critical temperature T_c, quarks and gluons confine again themselves into hadrons. This results in a mixed QGP and hadron gas phase (mixed phase);

5. hadronic gas phase ($\tau \geq 20$ fm/c): once all the quarks and gluons are again confined, the system can be described by an expanding hadronic gas;

6. freeze-out ($1 < \tau < 20$ fm/c):

   - chemical freeze-out: The relative abundances of hadrons are determined when the inelastic collisions between hadrons cease;
   - kinetic freeze-out: When the system further expands, the hadrons do not interact elastically anymore. The hadrons stream freely to the detectors.

The proper time predicted to be needed by the original Bjorken model for thermalization and QGP formation are too long to allow these to happen in small systems like p-p collisions, but other studies suggest that these times are actually shorter [12]. From all the stages of this process, various probes (hard partons or other electromagnetically interacting particles) can be emitted.

1.3.1 Charmonium production

In order to to be able to use charmonia as a probe for QGP, an accurate understanding of their production after the collision of two protons is needed.
In general, the production of a heavy $\bar{Q}Q$ pair involves energy scales ($2m_q$) where the pertubative QCD is applicable. However, the evolution of the $\bar{Q}Q$ pair into the quarko-

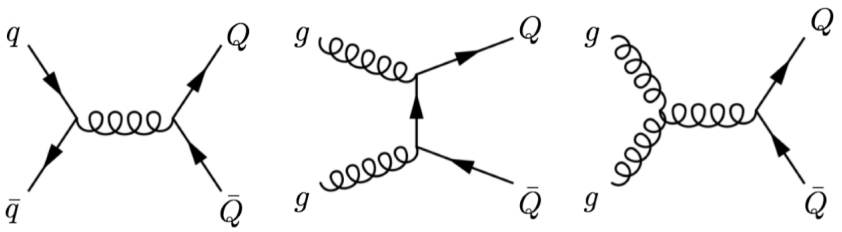

Figure 1.7: Heavy quark pair production at leading order through quark annihilation (left) and gluon fusion (middle and right).

nium state (hadronisation) involves energy scales of the order of the binding energy $m_q v^2$ (where v is the heavy quark velocity in the rest frame, considered to be non-relativistic) so it is a non-perturbative process. A $\bar{Q}Q$ pair can be created in 8 color states with a net color charge (color octet) and 1 state without color charge (color singlet), so the $\bar{Q}Q$ pair is usually created in a color octet state.

$$
\begin{array}{ll}
(r\bar{b} + b\bar{r})/\sqrt{2} & -i(r\bar{b} - b\bar{r})/\sqrt{2} \\
(r\bar{g} + g\bar{r})/\sqrt{2} & -i(r\bar{g} - g\bar{r})/\sqrt{2} \\
(b\bar{g} + g\bar{b})/\sqrt{2} & -i(b\bar{g} - g\bar{b})/\sqrt{2} \\
(r\bar{r} - b\bar{b})/\sqrt{2} & (r\bar{r} + b\bar{b} - 2g\bar{g})/\sqrt{6}
\end{array}
$$

$$
(r\bar{r} + b\bar{b} + g\bar{g})/\sqrt{3}
$$

Figure 1.8: One of the many ways to present the color octet states, plus the color singlet state.

In order to create a physical meson it is necessary to neutralize the color charge of the pair. This occurs through interaction with the surrounding color fields, but from a theoretical point of view the mechanism of color neutralisation is not yet fully understood [15]. Most of the available theoretical models (for example the Color Evaporation Model, the Color Singlet Model and the Color Octet Model) are based on the factorisation of the pair production and hadronization.
Since the mass of the charm quark is large ($m_c \simeq 1.3$ GeV), its velocity on the quarkonium rest frame can be considered to be small. Therefore, this can be approximated to a Schrödinger problem with a non-relativistic potential. The binding potential can be described by the Cornell potential:

$$V(r) = \sigma r - \frac{\alpha}{r} \tag{1.6}$$

with a string tension $\sigma \simeq 0.2$ GeV^2 and a Coulomb-like term with a gauge coupling $\alpha \simeq \frac{\pi}{12}$. The many solutions of the Schrödinger equation correspond to the different charmonia bound states.
The charmonium resonances and the possible transitions between them are shown in Fig. 1.10. The fundamental state 1S contains the J/ψ vector meson, which decays, among the other channels, into a dimuon pair with a probability of 5.93%. In hadronic collisions, all the resonances are formed in the initial hard collisions. The J/ψ can be produced from the hadronization of a c$\bar{\text{c}}$ pair (direct production), but it can also be produced by the decay of a higher mass state ψ(2S) or a χ_{cJ}(1P) ("feed-down"). The J/ψ sample from these processes is called "prompt". In hadronic collisions, approximately the 60% of the prompt J/ψ sample comes from direct production, the 30% from χ_{cJ} and the 10% from ψ(2S) decays. The J/ψ or ψ(2S) can also be produced from weak decays of B mesons ($\bar{\text{b}}$q and $\bar{\text{q}}$b) and in this case they are called "non-prompt". About 9% of the total J/ψ production, the so-called "B fraction", comes from B meson decays.
A polarization can be associated to these particles, defined as the alignment of a particular z quantization axis (usually the flight direction of the quarkonium in the laboratory

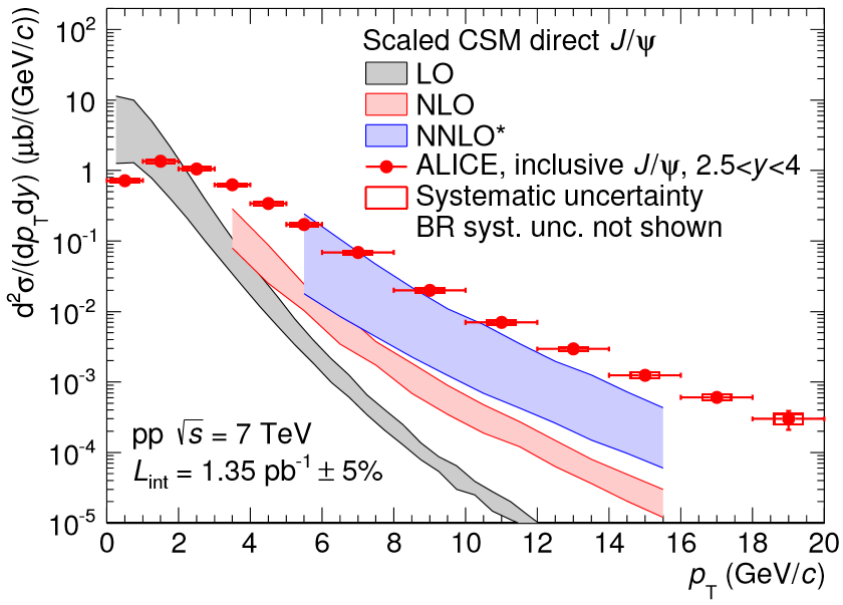

Figure 1.9: The J/ψ differential production cross section compared to the theoretical calculations performed in the Color Singlet Model at LO, NLO and NLO including the leading p_T contributions at NNLO [16]. It appears that improvements in the theoretical description are still needed.

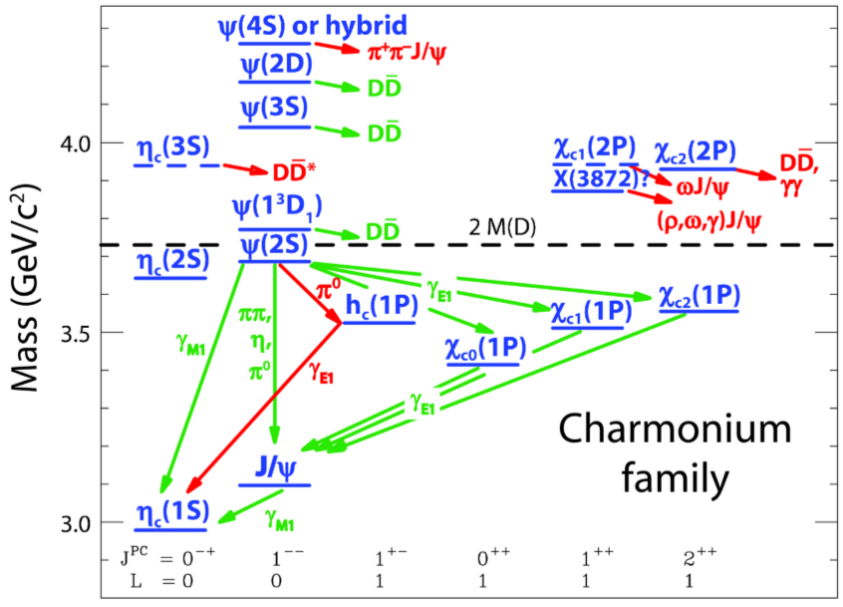

Figure 1.10: Spectroscopic diagram for charmonium family, with mass, spin, parity and charge conjugation.

frame) with their total angular momentum J. If J_z is -1 or $+1$ the polarization is "transverse", if $J_z = 0$ it is called "longitudinal" (see Fig. 1.11).

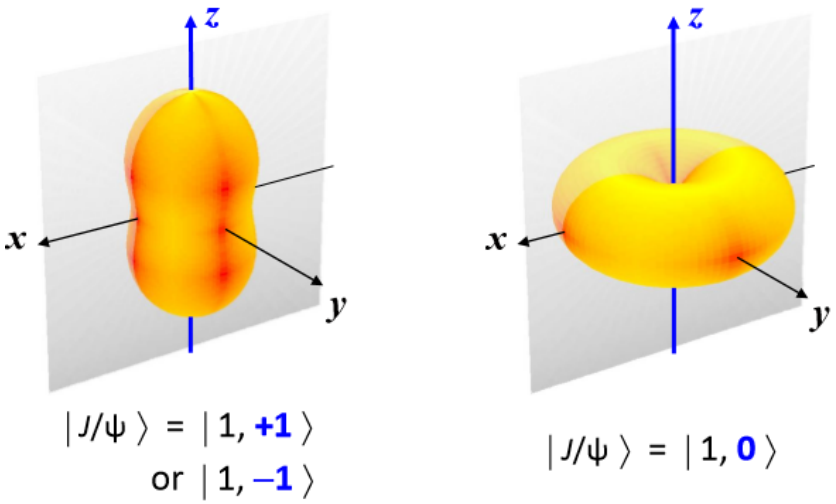

Figure 1.11: Angular distributions of the leptonic pair in a quarkonium$\rightarrow \ell^+\ell^-$ decay, for respectively transverse and longitudinal polarization.

1.3.2 Observable quantities

Due to the confinement property of the strong interaction the deconfined partons of a QGP cannot be observed directly. Only the indirect observation via the final products of the collision is possible. Many signals have been proposed to probe a phase transition to QGP. First of all, the general properties of the collision can be measured through the study of the global observables. The global observables provide information about the initial energy density, geometrical aspects of the collision and expansion dynamics. The initial energy density can be estimated through the measurement of the transverse energy and above all charged particle multiplicity. Moreover, the measurements of the charged particle multiplicity give also geometrical information such as the impact parameter of the collision, number of participating nucleons and number of binary nucleon-nucleon collisions. Particle spectra and azimuthal anisotropies can instead be used to determine the pressure gradient of the expanding medium, and thermal photons, directly emitted from the QGP, can give information about the initial temperature of the system. Furthermore, depending on the stage of the collision to be characterised, one can consider two classes of specific hints to the presence of QGP: the "hard probes", originated in the early stage of the collision and not affected by rescattering or system expansion, and the "soft probes", generated after the decay of the plasma. Examples of soft probes are:

- momentum distribution [18] the transition to QGP, as a phase transition, must imply a sudden change in the behaviour of state functions such as entropy, energy density and pressure as a function of temperature. After the formation of a QGP state the system can be modeled using relativistic hydrodynamics which involves collective motion. This results in a difference in the distribution of $\langle p_T \rangle$ as a function of charged multiplicity for different particle masses, explainable with an expansion of the medium. In fact, this provides a common velocity field for the entire medium along the radial direction, meaning a boost in particle momentum that is roughly proportional to the mass of the particle.
  Moreover "elliptic flow", an azimuthal anisotropy in momentum space, can be induced by the strong expansion of the initial almond-shaped overlap area of two nuclei/nucleons. The elliptic flow coefficients can provide a hallmark of collective final state interactions, i.e. the presence of a genuine matter whose spatial size and lifetime are large compared to the microscopic scales at this energy;

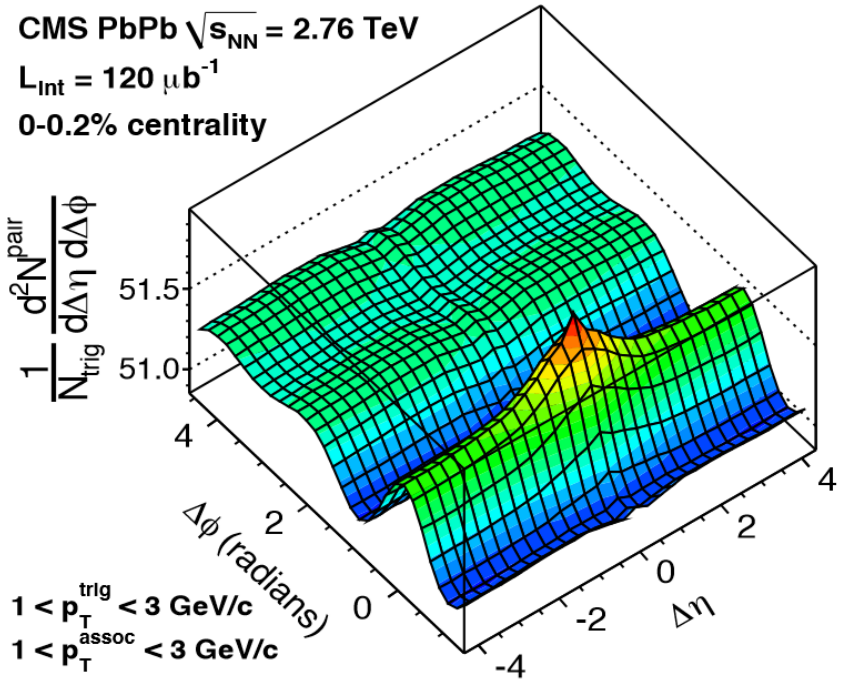

Figure 1.12: A pronounced near-side ($\Delta\varphi \sim 0$) collimation extending over a long range in $\Delta\eta$ is observed. This ridge-like correlation in heavy-ion collisions such as Au-Au at RHIC and Pb-Pb at the LHC is believed to be well understood: The overlap area of a heavy-ion collision at a finite impact parameter has an elliptic shape. The larger pressure gradients along the minor axis of the ellipse lead to a larger flow in this direction and therefore collimated production in both directions of this axis creating a near- and away-side ridge [18].

- strangeness enhancement: the production of strange particles in a normal hadronic environment has a higher production threshold, due to the higher mass of the s quark. But in a deconfined medium strange quarks are expected to be also abundantly produced via the gluon-gluon fusion process ($gg \rightarrow \bar{s}s$). This results in a higher yield of strange hadrons;

- jet quenching: when bound quarks separate, the strong confinement causes fragmentation and gluon radiation and then the formation of "jets" (high p_T hadronic showers), whose direction is defined by the momentum conservation. But within a QGP the quarks do not need to fragment; instead, as they travel through the dense medium, they lose energy by radiating gluons. For this reason the jets can be suppressed or even completely absorbed. This phenomenon is called "jet quenching", and it can be studied as a function of multiplicity or centrality which are used as estimators of the system density and temperature. However, it has been recently suggested that, instead of looking for jet quenching, the proper quantity to measure would be the energy loss per unit length [47], as the energy loss of hard partons depends in any case on the system size (perhaps too small in p-p);

- quarkonia suppression: the presence of a coloured medium affects the bound states of heavy quarks, weakening the effective potential that links quarks in a hadron. In analogy to what happens in electrically charged plasmas, in a QGP a quark pair will be in close proximity to other free quarks and gluons and their color charge will screen one quark from "feeling" the other; this phenomenon is known as "colour screening" and is reflected by the weakening of the string tension k of the strong potential. In this situation the Debye screening length can be defined, which depends on the temperature or density of the system. If the screening length is less than the $\bar{q}q$ Bohr radius, then approximately no quarkonium bound state can exist. This would lead to a reduced production probability, expecially for the excited states, that have a weaker bond. Also heavy flavor quark pairs such as $c\bar{c}$ (J/ψ) or $\bar{b}b$ (Υ) pairs, named quarkonia, are particularly sensible to QGP, because having large masses they can only be created in the primary nucleon-nucleon collisions. They are "fragile" objects, which easily interact inelastically with the medium and disappear being absorbed, so they are naturally suppressed for increasing transverse energy. But this kind of absorption increases smoothly with the energy, while QGP suppression implies something like an energy threshold, thus it is also important to inspect the dependency on the energy density.

In the framework of quark gluon plasma, there are also many observables that can be used to improve the modelization of these systems and to improve their understanding. For example [20, 21], one can look for a significant growth with the multiplicity, stronger than linear at higher multiplicities, of the prompt quarkonia relative yield. This departure from linearity, that should affect any hard observable, can be a consequence of

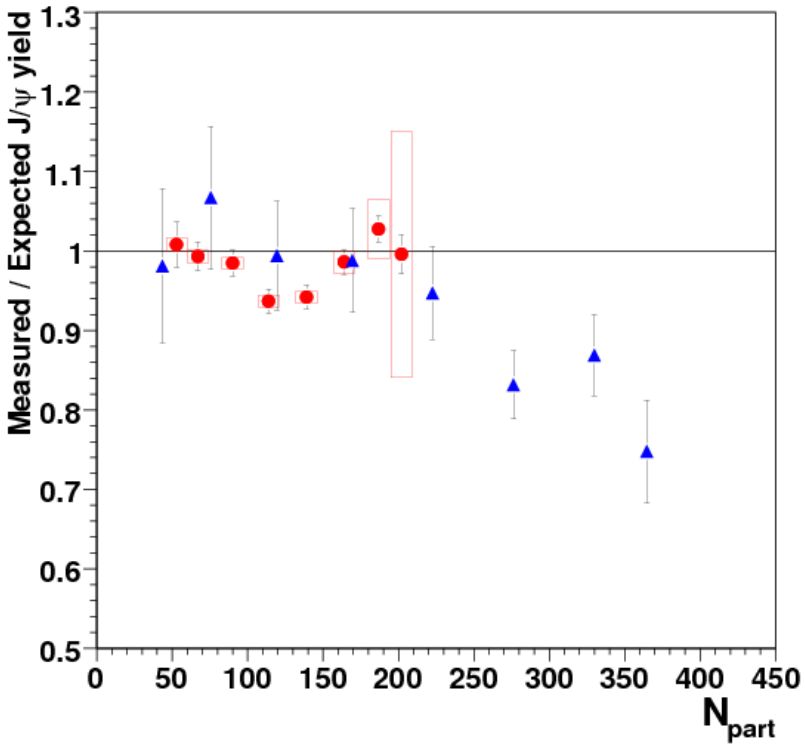

Figure 1.13: Anomalous J/ψ suppression in In+In (circles) and Pb+Pb collisions (triangles) as a function of the number of participating partons measured by the NA60 experiment [19].

processes like gluon shadowing or parton saturation, or maybe the strong *percolative* interaction among colour ropes that take place at LHC energies. Color ropes or flux tubes ("strings") are formed in each parton-parton collision and they constitute the elementary sources of particle production. Thus, the number of parton-parton collisions is reflected as the number of produced strings, N_s. These strings have non-negligible transverse size, of the order of 0.2-0.3 fm and different space-time rapidities, and they can interact overlapping, so reducing the effective number of sources. Their transverse size is determined by this transverse mass, since $r_T \propto 1/m_T$, so the softness of the source maximizes its possibility of interaction as its transverse size will be larger. The number of hard J/ψ, $n_{J/\psi}$, can be taken as proportional to the number of collisions, in analogy to any hard process. In the string-like models, this number corresponds to N_s. In presence of many strings they can interact thus reducing the effective number of sources, specially those concerning instead soft particle production (charged particle multiplicity), which agrees qualitatively with the concept of saturation. With these hypotheses about the different dependence on the number of strings of the soft and hard interactions, calculations predict a trend which is linear at low multiplicities and quadratic at high multiplicities. Some of the observables introduced above can be explained in some extent even without

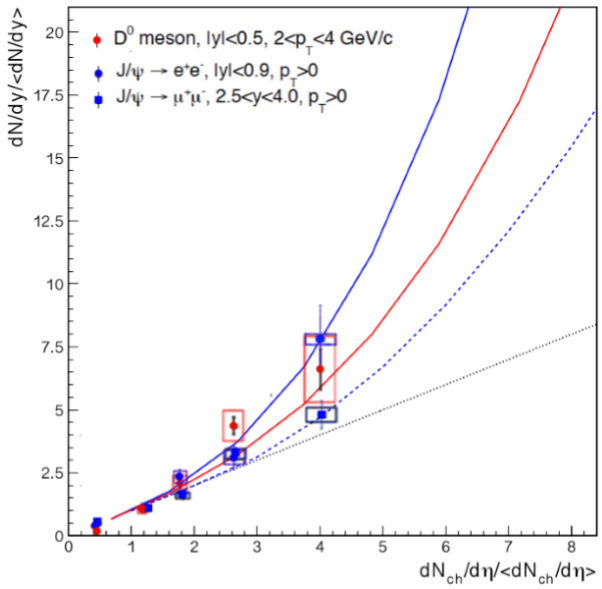

Figure 1.14: Predictions of the percolative model [21] on D meson production vs pseudorapidity density in the central rapidity range and on J/ψ production in the central and forward rapidity ranges for p-p collisions at 7 TeV, compared with the experimental data from the ALICE Collaboration. An initial linear behaviour (black line) is also plotted.

QGP, as the production of charmonium is altered during collisions already in absence of a hot medium, due to the presence of nuclear matter. These effects include the shad-

owing, due to the modification of the quark and gluon distribution functions inside the colliding nucleons, the coherent parton energy loss induced by the nuclear medium or nuclear absorption of the $c\bar{c}$ pair or resonances. Generally speaking, these effects are referred to as Cold Nuclear Matter (CNM) effects. Some examples are:

- parton energy loss: high energy parton travelling in a medium can radiate gluons induced by the elastic scatterings with the constituents of the medium;

- interaction with comovers: the dissociation due to interaction with a hadronic comover medium, through much or all of its geometric cross section. Its most recognizable feature is that the suppression increases continuously; there cannot be a sudden onset like in color deconfinement [13], although there may be a similarity with a cross-over type transition, depending on its graduality;

- Multiple-Parton Interactions (MPI): several parton-parton interactions occurring in a single p-p collision. They introduce a correlation of the J/ψ production with the underlying event. It is not clear if they affect also the hard scales relevant in quarkonium production, but if so this could explain the observed rise of the J/ψ yield in pp collisions as a function of multiplicity;

- quarkonium regeneration: the formation of charmonium states also from uncorrelated $c\bar{c}$ pairs in the hot medium. This is possible due to the increase of the $c\bar{c}$ cross section with the energy, competing with color screening.

QGP in p-p and heavy-ion collisions

Many experiments have been studying the possibility of QGP formation in heavy-ions collisions at high energy. In 1986 the Super Proton Synchrotron (SPS) at CERN, began the heavy-ion collision program and first tried to create the QGP, with center of mass energies from 8 to 20 GeV. In the 2000 the Relativistic Heavy-ion Collider (RHIC) started operations with energies of 130-200 GeV. In the last decade also the Large Hadron Collider at CERN, mainly with the ALICE experiment, started studying QGP formation. Since 2010, RHIC and LHC data on heavy-ion collisions have shown several important features which indicate the formation of a high density partonic medium with characteristic properties.
LHC in particular [14], with Pb–Pb collisions at $\sqrt{s_{NN}} = 2.76$ TeV (Run 1) and $\sqrt{s_{NN}} = 5.02$ TeV (Run 2, still in progress), has reached higher energies allowing to confirm that higher energy densities (accompanied by higher particle multiplicities) lead to a hotter, wider and longer-lived medium as well as to a more abundant production rate of hard probes. The medium created in these situations is found to be characterized by strong collectivity, behaving like an almost perfect liquid. It reacts to pressure gradients with little internal friction and is also extremely opaque to even very energetic coloured

particles that propagate through it.
Proton-proton systems have much smaller volume with respect to the nuclei, and they have been frequently used in heavy-ion physics for comparisons with collisions where QGP is not expected to be formed. But now, since the energy density achieved in high multiplicity events produced in pp collisions at LHC is comparable to the reached density in Cu-Cu central collisions or Au-Au peripheral collisions at $\sqrt{s} = 200$ GeV, it is pertinent to wonder about the possibility to obtain a similar high density medium which would be reflected in experimental observables, similar to heavy-ion collisions. It would be very interesting to study multiplicity dependencies here, since these collisions are not affected by nuclear effects that can shadow and mislead the measurements. p-p studies could contribute to measure the critical temperature and to define experimentally the properties of the possible change of phase. In small systems like p-p and p-A some of the typical hallmarks of collective behaviour in strongly interacting systems (like the elliptic flow described before) have been indeed observed, even if the latter can still be reproduced also with different models by now.
All these studies are expected to contribute to one of the main research objectives of heavy-ion physics: to understand how collective phenomena and macroscopic properties emerge in complex evolving systems from the microscopic laws of Standard Model QCD.

Chapter 2

The CMS experiment at the LHC

In the following chapter the main features of the CMS experiment at the LHC will be presented.

2.1 The LHC accelerator at CERN

The Large Hadron Collider (LHC) is a particle accelerator, currently the largest in the world, based at CERN laboratories near Geneva, between Switzerland and France. Its purpose is to help finding an answer to the main issues of particle physics, such as the differences between matter and antimatter, the consistency of the Standard Model at very high energies, the nature of dark matter and dark energy, the possible existence of extra dimensions, the origin of mass or the reason of the symmetry breaking in the electro-weak sector. The collider is a 27 Km underground hollow ring where two beams of protons or ions, circulating in opposite directions into separate pipes, are forced to collide in four points where the detectors of the four major experiments (ALICE, ATLAS, CMS and LHCb) are located. The detectors of other two experiments, TOTEM and LHCf, are placed along the beamline in proximity to respectively CMS and ATLAS.
The pipes are kept at ultrahigh vacuum to avoid collisions with air or gas molecules. LHC is endowed with more than 1600 superconductive magnets cooled with superfluid helium at temperatures below 2 K, able to produce a strong magnetic field up to 8.4 T. Among these magnets there are 1232 magnetic dipoles that curve the beam, 392 magnetic quadrupoles aimed to focus the beam, and various smaller correcting magnets. A section of one dipole magnet is shown in Fig. 2.1.
The LHC is supplied with protons obtained from hydrogen atoms initially accelerated by the linear accelerator Linac 2 or lead positive ions by another linear accelerator, Linac 3. These two machines are only the beginning of the injection chain ending in the main ring: Linac - Low Energy Ion Ring (LEIR), only for the ions - Proton Synchrotron Booster (PSB) - Proton Synchrotron (PS) - Super Proton Synchrotron (SPS) - LHC, as shown

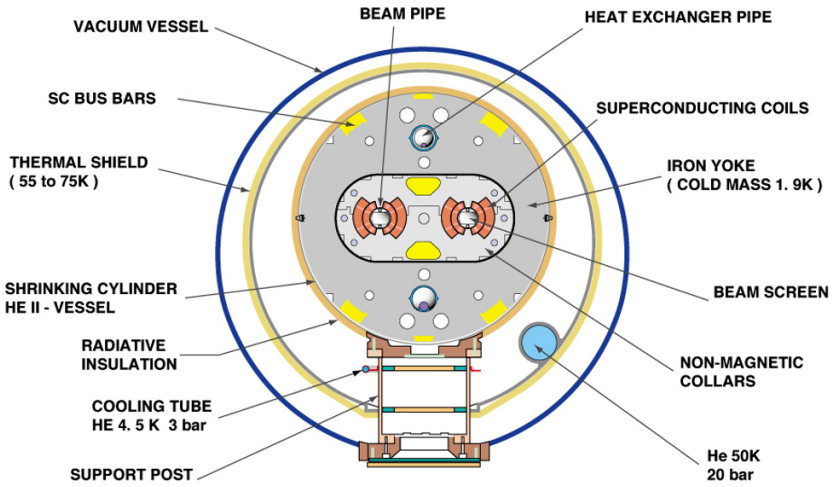

Figure 2.1: Cross section of a LHC dipole.

in Fig. 2.2.

Tthe chain is designed to meet the strict LHC requirement of 2808 high intensity proton bunches in the ring. Inside the LHC, radiofrequency (RF) cavities accelerate particles and keep them in controlled bunches. RF cavities are metallic chambers in which an electromagnetic field is made to oscillate at a given frequency able to accelerate the particles to the same maximum energy and keep it fixed, also correcting for the loss of energy through synchrotron radiation. When particles reach the designed energy they will feel no accelerating voltage, otherwise they are accelerated or decelerated. There are 16 RF cavities (8 per beam) along the LHC, operating in a superconducting regime and driven by high-power klystrons. Each cavity can deliver up to 2 MV, resulting in 16 MV for each beam.

The number of events of a given process produced per second (event rate) is given by:

$$R = L\sigma_{proc} \tag{2.1}$$

where σ_{proc} is the cross-section of the physics process under study, and L is the instantaneous luminosity, an important operational characteristic expressed by:

$$L = \frac{f_{rev} n_b N_b^2 \gamma}{4\pi\epsilon_n \beta^*} F \tag{2.2}$$

in which f_{rev} is the revolution frequency, n_b is the number of bunches per beam, N_b is the number of particles in each colliding bunch, ϵ_n is the normalized transverse beam emittance, β^* is the beta function at the collision point, γ is the relativistic factor and F the geometric luminosity reduction factor.

At each step of the particle acceleration chain the energy of the particles is increased,

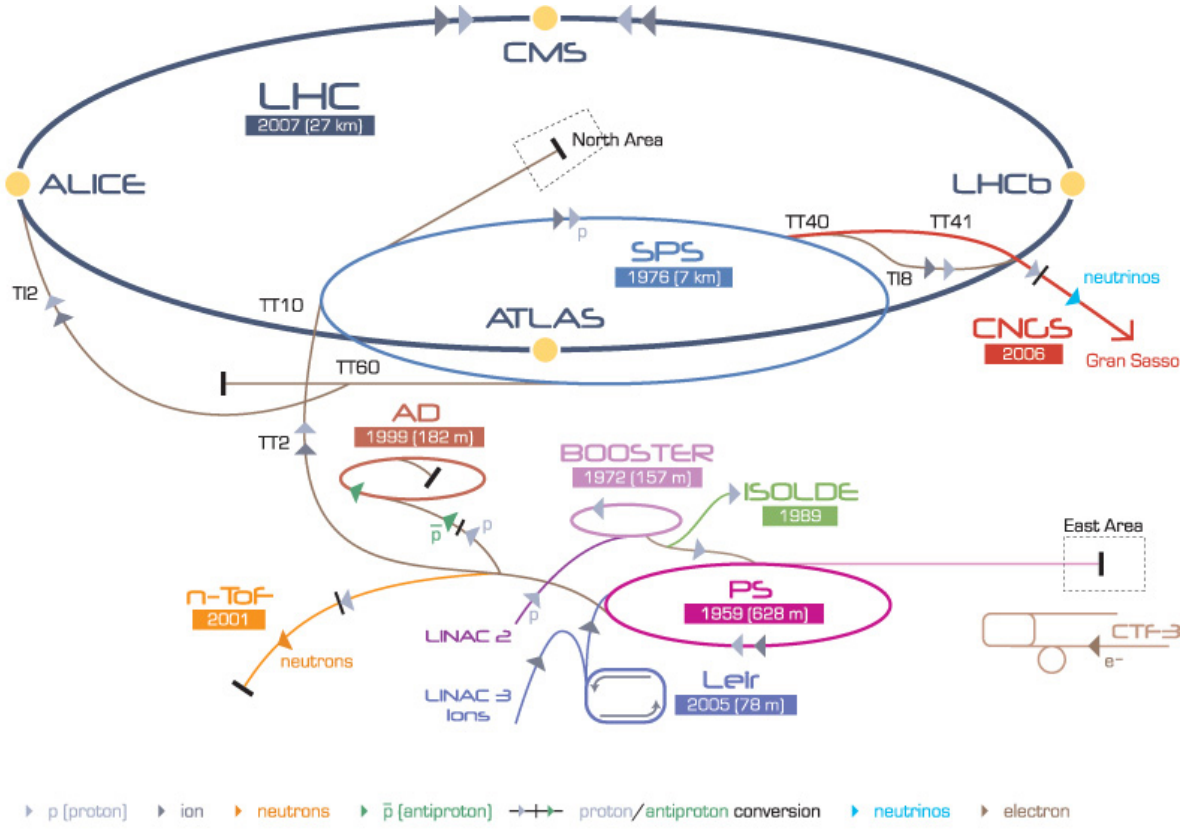

Figure 2.2: Scheme of the CERN accelerator chain.

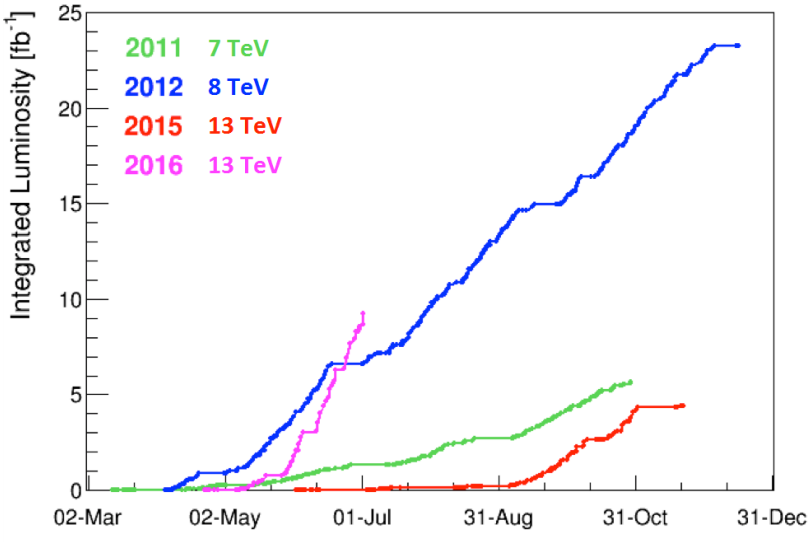

Figure 2.3: Integrated luminosity collected at LHC during its years of activity.

allowing to reach the final energy of currently about 6.5 TeV for protons and above 500 TeV for lead ions, thus above 5 TeV per nucleon pair. Its current peak luminosity is about 0.07 nb/s, while the integrated luminosity collected since 2011 at various operating energies is shown in Fig. 2.3.

2.2 The CMS experiment

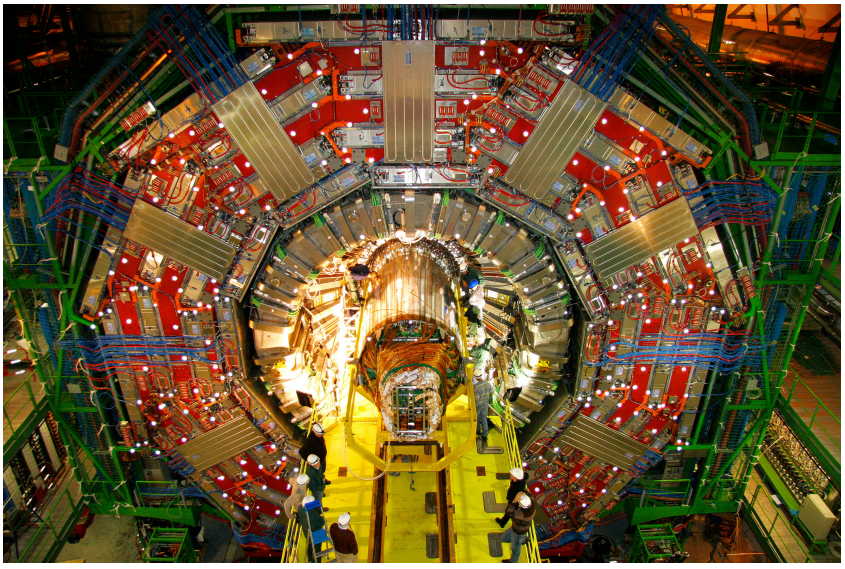

Figure 2.4: Installation of the silicon tracking detector in CMS.

The Compact Muon Solenoid (CMS) detector is installed at the LHC point 5, in French territory, and its purpose is to observe a wide variety of phenomena in proton-proton and heavy-ion collisions. It is composed by five "layers" with a cylindrical shape and sealed by two endcaps, equally endowed with detectors. In Fig. 2.5 is sketched a wedge of the detector: the silicon pixel and strip tracker, the electromagnetic calorimeter, the hadron calorimeter, the superconducting solenoid and the muon detectors embedded in the steel return yoke. A detailed description of the detector can be found in ref. [24].

2.2.1 Coordinate System

A cylindrical coordinate system is used to describe the positions and directions in CMS, because of the detector symmetries and also for the symmetry of physics itself, which is supposed to be uniform in the transverse plane. The origin is the geometrical center of

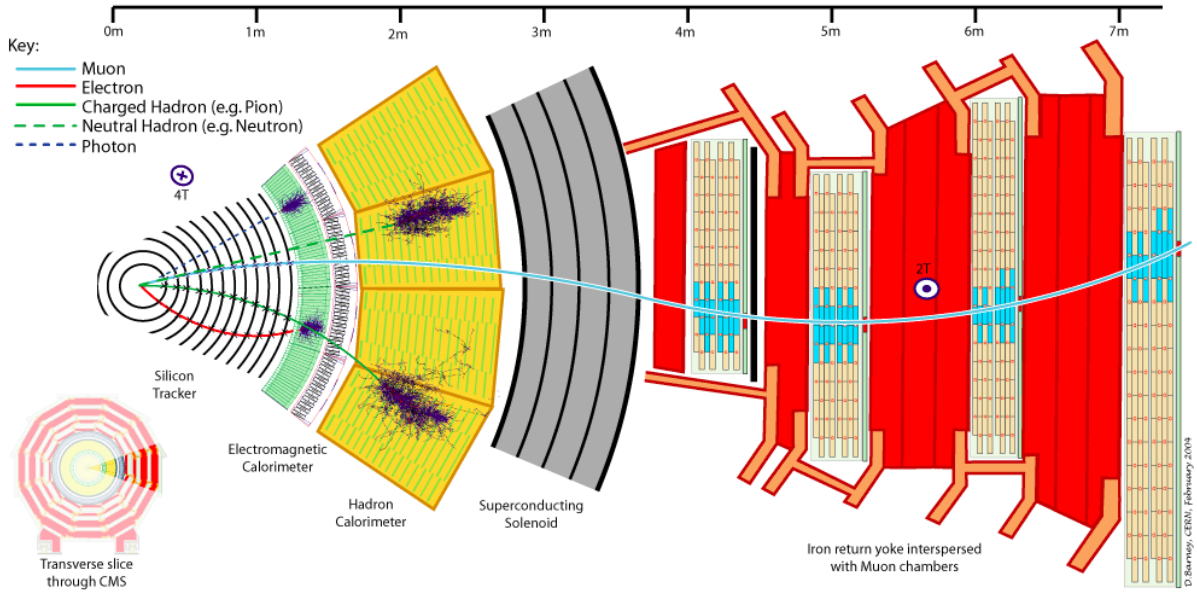

Figure 2.5: Section of the CMS detector.

CMS corresponding to the interaction point, the z axis is at the center of the barrel along the beam line, the x axis is pointing to the centre of LHC ring and the y axis is vertical upward. The polar angle θ is measured from the z axis, the azimuthal angle ϕ is defined in the xy plane starting from the x axis and r is the distance from the origin. A quantity very much used in particle physics is the rapidity. Given a particle with momentum of p and energy E, its rapidity is defined as

$$y = \frac{1}{2} \ln \frac{E + p_z c}{E - p_z c} \tag{2.3}$$

Using $p_z = p\cos(\theta)$ and $p = \beta E$, in the approximation of particles travelling at the speed of light ($\beta \sim 1$), the rapidity can be approximated by the "pseudorapidity", which depends only on the polar angle:

$$\eta = -\ln \tan \frac{\theta}{2} \tag{2.4}$$

This variable can be useful if the information about the particle mass is not available. The CMS coordinate system is represented in Fig. 2.6.

Some other useful quantities are:

- particle transverse momentum: $p_T = \sqrt{p_x^2 + p_y^2}$;
- transverse energy: $E_t = E\sin(\theta)$;
- transverse mass: $m_t = \sqrt{m^2 + p_T^2}$.

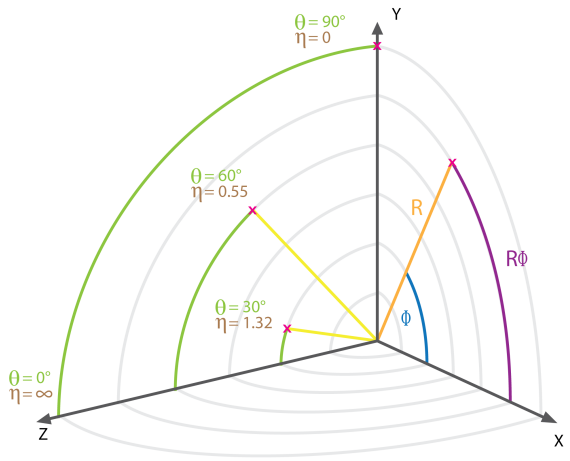

Figure 2.6: The CMS coordinate system.

2.2.2 Tracker

At the heart of the detector lays the tracker, whose task is to track the charged particles produced in the collision. The tracker covers a cylindrical region of 115 cm in radius and 540 cm in length, and it is composed by a silicon-based pixel detector with three barrel layers, 4, 7, and 11 cm away from the beam, closest to the collision point, and a silicon micro-strip tracker with 10 barrel detection layers. Here even the decays vertices of very short-living particles can be seen. Pixels are also placed on the endcaps, with two layers constituted of modular detector units and divided in 24 sections tilted to take into account the Lorenz drift angle. The active area of each pixel is 150×100 μm^2. Each pixel generates around 50 μW, so that an integrated cooling system is needed.

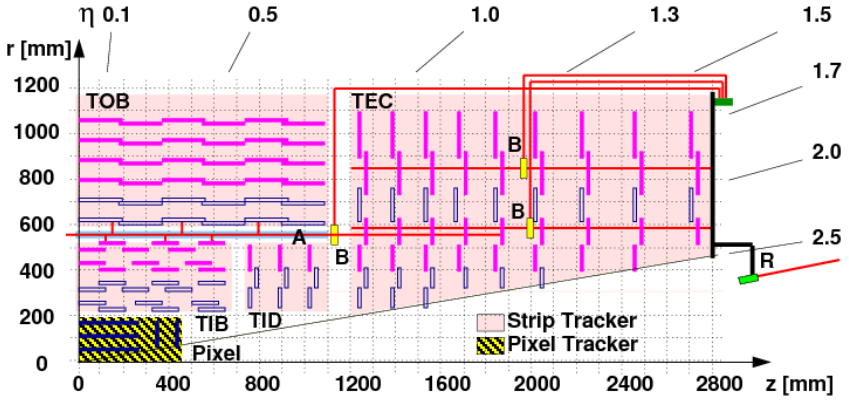

Figure 2.7: Scheme of the tracker.

The pixels consist of about 66 millions modules, which contain a sensor plate attached to

highly integrated readout chips; the microstrip system instead contains 15,200 sensitive modules clustered in 10 million detector strips. All the modules are attached to 80,000 readout microelectronic chips, thus the micro-strip region needs a much lower quantity of readout electronics per unit area. The core part of the pixels and the micro-strips is essentially a rectifying junction that is activated by when traversed by a charged particle. The signals are then transmitted through optic fibers cables outside the detectors. Furthermore, the energy loss in the tracker material is used for particle identification.
The algorithms used for tracking reconstruct tracks over the full pseudorapidity range covered by the tracker $|\eta| < 2.5$, detecting charged particles with $p_T > 0.1$ GeV. For isolated muons with $p_T > 0.9$ GeV/c, the reconstruction efficiency is essentially 100%. In the central region ($|\eta| < 1.4$), where the resolution is the best, muons of $p_T = 100$ GeV have resolutions of approximately 2.8% in p_T and 10 μm and 30 μm, respectively in the transverse and longitudinal impact parameters. The resolution progressively degrades as η increases.

2.2.3 Electromagnetic Calorimeter

The electromagnetic calorimeter (ECAL) is used to measure precisely the energy of photons and electrons. This task is performed by measuring the light, proportional to the particle energy, produced by the scintillation of lead tungstate crystals due to the passage of a particle. The light detection is performed by avalanche photodiodes in the barrel crystals and vacuum phototriodes in the endcaps. A preshower detector consisting of two planes of lead and several silicon sensors is placed at the end of the ECAL to distinguish single high-energy photons from pairs of low-energy photons.
The energy resolution of the electromagnetic calorimeter is described by the following formula:

$$\left(\frac{\sigma}{E}\right)^2 = \left(\frac{a}{\sqrt{E}}\right)^2 + \left(\frac{\sigma_n}{E}\right)^2 + c^2 \tag{2.5}$$

where a accounts for the stochastic contribution, σ_n the noise and c^2 is a constant. For E expressed in GeV , the constants for the energy resolution for electrons in beam tests are: $a = 2.8\%$, $\sigma_n = 12\%$, $c^2 = 0.3\%$ [27].

2.2.4 Hadron Calorimeter

The hadronic calorimeter (HCAL) is important for the measurement of hadronic jets, and indirectly exotic particles or neutrinos resulting in missing transverse energy. Its structure consists of 20° wedges inside the magnet and is able to detect particles up to $|\eta| = 5$. Other two calorimeters are placed outside the calorimeter to complement its coverage for lower angles. Also these calorimeters are based on scintillation: fluorescent scintillators plus hybrid photodiodes. Here the scintillators detect particles only indirectly, through hadronic showers produced into layers absorbers placed between them.

These absorbers are made of plates of brass and steel and the interaction length associated to them varies with η. The scintillators and the photodiodes are connected by wavelength-shifting fibers.
The energy resolutions vary in the different regions of the hadronic calorimeter, but they are described by the same formula:

$$\frac{\sigma}{E} = \frac{a}{\sqrt{E}} + c \tag{2.6}$$

where E is measured in GeV, c is equal to 5% and a is equal to 65% in the barrel, 85% in the endcap, and 100% in the forward hadronic calorimeter.

2.2.5 Forward detectors

Two devices are placed in the forward regions of CMS: CASTOR (Centauro And Strange Object Research) and ZDC (Zero Degree Calorimeter). CASTOR is an electromagnetic and hadronic calorimeter based on plates made out of tungsten and quartz layers. Its physics motivation is to complement the analysis of both pp and heavy-ion events, search for exotic events that are likely to appear in the very forward region of the CMS detector. It covers the pseudorapidity range $5.2 < |\eta| < 6.6$. ZDC is a set of two calorimeters with a pseudorapidity coverage of $|\eta|$ from 8.3 to close to the beam pipe for neutral particles, designed to complement CMS in the very forward region for the measurement of neutrons and very forward photons. It is composed by two calorimeters, respectively hadronic and electromagnetic, located on the opposite sides of CMS.

2.2.6 Magnet

The solenoidal magnet is a superconducting solenoid, made of four windings of Niobium-Titanium cables, in which a current of 19500 A flows, generating a uniform magnetic field up to 4 T. In order to maintain this magnetic field, the solenoid is constantly kept at a temperature of 4 K. The whole magnet is 12.5 m long with an inner diameter of 6 m. At more than 5m from the beam pipe is placed an external iron yoke, to close the lines of the magnetic field.
The magnet is fundamental to distinguish different charged particles by allowing the determination of the charge/mass ratio, bending their trajectory with a different curvature radius with its magnetic field. The magnets also provides mechanical stability to the detector.

2.2.7 Muon detectors

The muon detectors identifies muon tracks, measures their momentum and performs the trigger, thanks to a response time of only 3 ns. It is composed by detectors of three

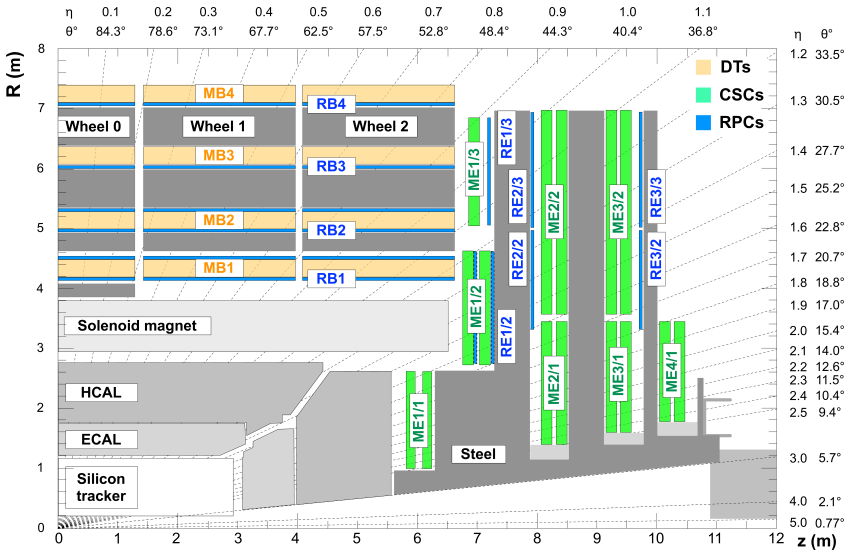

Figure 2.8: Scheme of the muon system.

kinds: 250 drift tubes (DT), 540 cathode strip chambers (CSC) and 610 resistive plate chambers (RPC). DTs and RPCs are placed in the barrel whereas CSCs and RPCs complete the endcaps disks at both ends of the barrel. The first ones are organized in cells with an area of 6.24 cm^2 and contain stretched positively-charged wires within a gas of Ar (85%) and CO_2 (15%), and work as tracking detectors. Consecutive DT layers are misaligned by half cell in order to improve coverage and reduce blind spots. The second ones are placed in the endcap region, and provide pattern recognition for rejection of non-muonic backgrounds and matching of hits to those in other stations and to the CMS inner tracker. CSCs are similar to DTs but in addition they have negative charged (cathode) strips to collect positive ions from a gas of Ar (30%), CO2 (50%) and CF_4 (20%). Strips and wires are perpendicular, so they provide a bidimensional position information. The RPCs consist of two parallel plates, one positively-charged and another negatively-charged, both made of a very high resistivity plastic material. They collect the electrons and ions produced in the gas layer separating them, which consists of $C_2H_2F_4$ (96.5%) and C_4H_10 (3.5%). These electrons in turn hit other atoms causing an avalanche. The electrons resulting are then picked up by external metallic strips, to give a quick measurement of the muon momentum, which is then used by the trigger to make immediate decisions as of whether the data are worth keeping. The joint operation of all the components described above enables the CMS detector to provide a full reconstruction of the events, as shown in Fig. 2.9.

Moreover, the outer muon chamber system provides a second measurement for the transverse momentum of the muon which can be combined with the measurement obtained by the tracker in order to improve the overall resolution. This feature allows to reconstruct

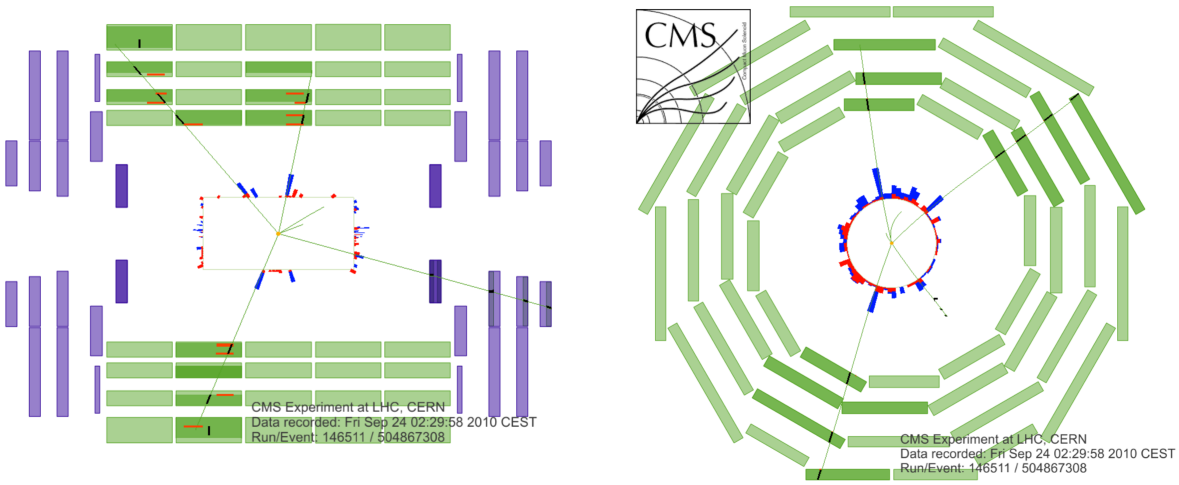

Figure 2.9: The longitudinal and transverse views of a collision event in which the tracks of four muons were reconstructed.

muons with an efficiency above 98%. The spatial resolution per chamber is 80–120 μm in the DTs, 40–150 μm in the CSCs and 0.8–1.2 cm in the RPCs; for $p_T < 100$ GeV/c the relative p_T resolution is between 1.3% to 2.0% for muons in the barrel and lower than 6% in the endcaps, while for higher p_T up to 1 TeV/c is still lower than 10%.

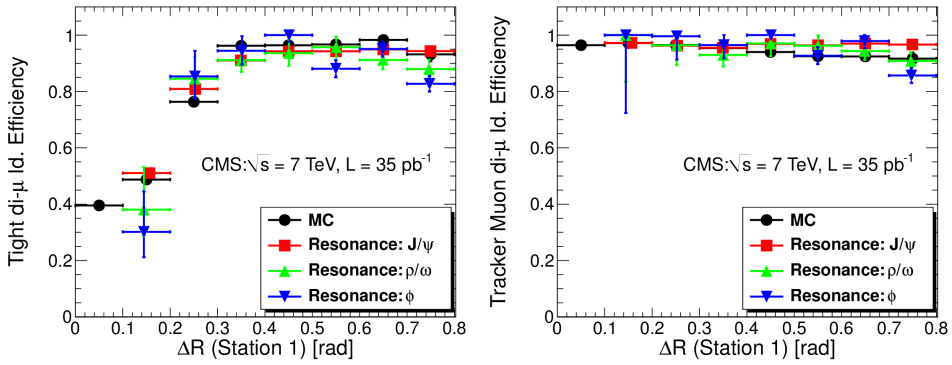

Figure 2.10: Efficiency for identifying both muons in the dimuon pair as Tight muons and Tracker muons (all those reconstructed in the tracker) as a function of the angular separation of the two tracks computed at the surface of the first muon station.

The muon identification can be carried out by different algorithms, like Particle-Flow Muon selection, Soft Muon selection or Tight Muon selection, the most selective thus also the less efficient. Misidentification is lower than 1% for the loosest selection and below 0.1% for the tightest.

2.2.8 Beam Monitoring System

The CMS detector monitoring system is composed by several subdetectors whose primary purpose is to detect and limit the damage due to unexpected beam losses, while allowing for quick post-mortem analysis should a large loss occur. But one of these elements, the Beam Pick-up Timing for the eXperiments (BPTX), is also used to trigger the detector readout on minimum bias or zero bias events. The two BPTX devices, located around the beam pipe at a distance of 175 m from the interaction point on both sides, are designed to provide precise information on the bunch structure and timing of the incoming beam, with a time resolution better than 0.2 ns. The readout is achieved through a commercial 5 GigaSamples/second oscilloscope. Comparisons of the relative timing from the electrodes allows the monitoring group to ensure that the data taken come from collisions very close to the interaction point.

2.2.9 Trigger system

At LHC there are on average over twenty inelastic pp collisions per bunch crossing, and since the bunches are only 25 ns apart, the total data output is too big to be stored. However, the events of physical interest are only a small fraction of the total. The Trigger and Data Acquisition System's task is to make a first selection so that data can be stored at the archival storage capability of about 102 Hz at data rates of about 102 MB/s, rejecting roughly 105 events for every accepted one. The first CMS trigger that selects data to be retained or discarded is the Level 1 Trigger (L1), a hardware system which analyses informations about particle tracks mainly obtained by the calorimeters and the muon system and filters only the events where some particular quantities pass a certain threshold, reducing the rate of data flow to about 100 kHz. It is constituted by three primary components: the L1 calorimeter trigger, the L1 muon trigger, and the L1 global trigger. They all have to decide whether to save the event or not within 3 μs after each collision, because after that time the data temporally saved in the buffers are overwritten. The High Level Trigger (HLT) is constituted by a computer farm of commercially available processors that analyze one event each, where a preliminar reconstruction of the events is performed, and if at least one of the trigger conditions of this level is satisfied, all the data of this event are saved and the event is classified according to the triggers passed. The HLT trigger paths can be grouped according to the topology of the event they select: "muon triggers" and "electron triggers", for instance, select events where the HLT can identify at least one (or more) muon or electron satisfying well defined requirements; "multijet triggers" are instead characterized by high jet multiplicity. Data streams are then composed from series of events that have passed triggers which can be grouped by some feature. These only later are saved in separate datasets, where they can be accessed for various kinds of analyses. When the HLT evaluates a L1 candidate, firstly it continues the L1 reconstruction, then, if the candidate

is not discarded, it reconstructs its tracks with also the information from the tracker. At the end, the rate of data is reduced to about 100 Hz.
For example, minimum bias pp events are triggered by requiring the coincidence of signals from both BPTX devices, indicating the presence of two proton bunches crossing at the interaction point (zero bias condition). Triggers of this kind are called HLT ZeroBias in CMS, as no particular physics is required. Also some HLT MinBias triggers are available, which require some basic properties for tracks, for example at least two tracks. Since ZeroBias triggers save in principle every event, they have the highest trigger rate, thus they are normally very pre-scaled (two orders of magnitude) in order to deliver a reasonable amount of data. Moreover, since 2010 CMS enabled also some high multiplicity triggers, which trigger events with a high number of particles with $p_T > 0.4$ GeV/c and $|\eta| < 2.4$. These events can be used to rise the statistics at high multiplicities.

2.2.10 Software

The CMS Software (CMSSW) is a set of tools and algorithms that are used for the event simulation and/or reconstruction. The event reconstruction chain is common to both real and simulated events: it is used to interpret the various electronic signals from the event readout into physical quantities or objects. At the end of the reconstruction, the particle tracks in the inner tracking system and muon system have usually been identified and the energy released by particles in the calorimeter cells is aggregated to form energy clusters. These data can then be analyzed in a second time by users, running algorithms to extract and save the desired physics plots and numbers. The whole CMSSW framework is based on an Event Data Model (EDM) for the analysis on real data and simulated Monte-Carlo data. The core program is written in C++, with some Python scripts calling C++ modules. Data are stored as a single entity in memory in a C++ container named Event, which contains every information about what happened in the detector during the collisions, such as tracks, energy reconstructed from calorimeter and so on, about a collision. This analysis has been performed using CMSSW, versions 4.4.2(patch 2), 5.3.8 and 7.6.3, in order to create files containing all the needed information, then the ROOT framework, versions 5.34/00-rc1 and 6.02/13, to analyse physics data.

Chapter 3

Charmonium candidates reconstruction

In this chapter the extraction of the J/ψ and ψ(2S) yields will be described, and subsequently the separation of their prompt and non-prompt fraction. These charmonia are detected thorugh their decay channel into two muons, reconstructed matching track data from the core tracker and the outer muon detectors.

3.1 Data selection

This analysis uses data taken by CMS during the 2011 proton-proton run at $\sqrt{s} = 7$ TeV, during which an integrated luminosity of 5.55 fb^{-1} was collected. This choice is motivated by the lower p_T trigger threshold and the good gathered statistics, in a lower pile-up environment with respect to more recently collected data.

Data were collected using specific trigger paths developed by the B-physics group, trying to maximise the available bandwidth. The resulting total collected dimuon spectrum is shown in Fig. 3.2. During 2011 the instantaneous luminosity kept increasing (see Fig. 3.1) and different trigger threshold were applied. The High Level Trigger path sets ("menus") used are displayed in Tab. 3.1. They are named after the instant luminosity (in cm^{-2}s^{-1}) in their run period.

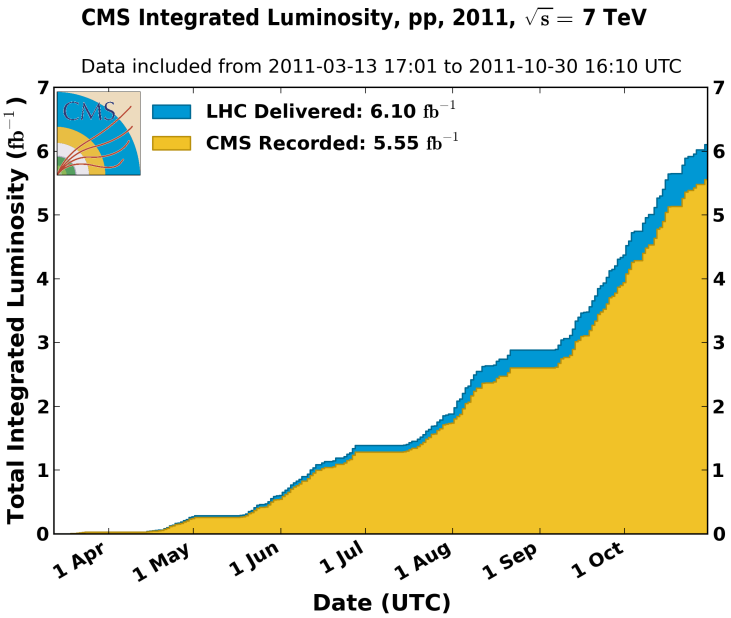

Figure 3.1: Proton-proton total Integrated Luminosity in 2011.

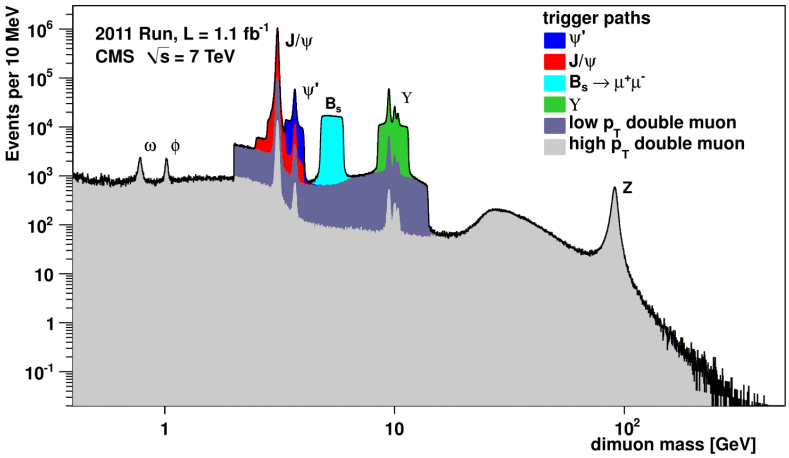

Figure 3.2: Dimuon invariant mass distribution collected with various dimuon triggers.

Menu	Trigger path	L_{int} (pb^{-1})
5E32	*DoubleMu3_Quarkonium*	55.9
	Dimuon6p5_Barrel_Jpsi	165.6
	Dimuon6p5_Barrel_PsiPrime	165.6
1E33	*Dimuon10_Jpsi_Barrel*	660
	Dimuon7_PsiPrime	660
1.4E33	*Dimuon10_Jpsi_Barrel*	255
	Dimuon7_PsiPrime	255
2E33	*Dimuon10_Jpsi_Barrel*	693
	Dimuon7_PsiPrime	
3E33	*Dimuon10_Jpsi_Barrel*	2082.9
	Dimuon13_Jpsi_Barrel	
	Dimuon9_PsiPrime	
	Dimuon11_PsiPrime	
5E33	*Dimuon10_Jpsi_Barrel*	819.5
	Dimuon13_Jpsi_Barrel	
	Dimuon9_PsiPrime	
	Dimuon11_PsiPrime	

Table 3.1: Trigger paths with respective versions for J/ψ and ψ(2S) (the *Quarkonium* trigger collects data of both).

The *DoubleMuX* and *DimuonX* triggers select only dimuon events with $p_T \geq X$. The first operated only at the beginning of data taking, applied the p_T cuts at the single muon level, while the second triggers work on the pair p_T. The mass windows were $2.5 < M < 4.0$ GeV wide for the J/ψ and $3.35 < M < 4.0$ GeV for the ψ(2S) during the 5E32 menu, and were changed to $2.8 < M < 3.35$ GeV and $3.35 < M < 4.05$ GeV from the 1E33 trigger menu onwards. The term "Barrel" refers to a dimuon rapidity cut of $|y| < 1.3$, during the 5E32 trigger menu, while for the trigger menus from 1E33 onwards they refer to $|y| < 1.25$. From trigger menu 1E33 onwards all paths have a pile-up protection through a Distance of Closest Approach (DCA) cut between the two muons of < 0.5 cm, and use a cut on the vertex χ^2 probability of 0.5%. From the 2E33 trigger menu onwards all paths reject, because of their worse efficiency, "cowboy" dimuons: muons with tracks bending towards each other, as opposed to "seagull" dimuons. In the 3E33 trigger menu the unprescaled lower p_T dimuon trigger path becomes inactive if the instantaneous luminosity reaches $L = 4 \cdot 10^{33}\text{cm}^{-2}\text{s}^{-1}$ for the J/ψ triggers or $L = 5 \cdot 10^{33}\text{cm}^{-2}\text{s}^{-1}$ for the ψ(2S) ones. With these triggers, $5.73 \cdot 10^7$ events are collected, which correspond to an integrated luminosity of 4.9 fb^{-1}.
The number of events passing all these triggers is shown in Fig. 3.3.

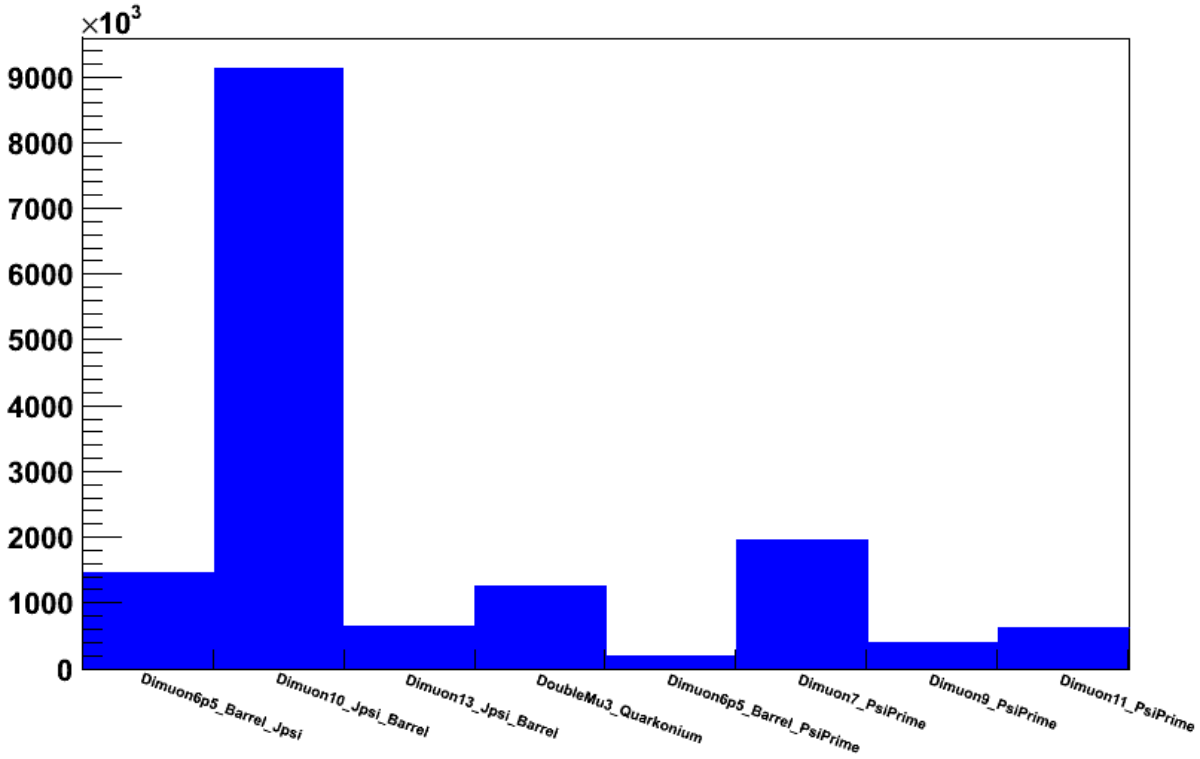

Figure 3.3: Number of events passing the trigger selection.

3.2 Dimuon selection

The standard CMS *Soft* track selection for 2011 data has been applied:

- tracker track matched with at least one muon segment (in any station) in both x and y coordinates (within 3σ);
- number of tracker layers with hits > 5;
- number of pixel layers with hits > 0;
- *HighPurityTrack* flag, with requirements defined by the CMS experiment [28];
- *loose* transverse and longitudinal impact parameter cuts: $d_{xy} < 0.3$ cm and $d_z < 20$ cm with the primary vertex.

The consecutive effects of these cuts on the dataset is shown in Fig. 3.4.
Reconstructed muons were then discarded for $|\eta| > 2.4$ and if they did not fulfill these

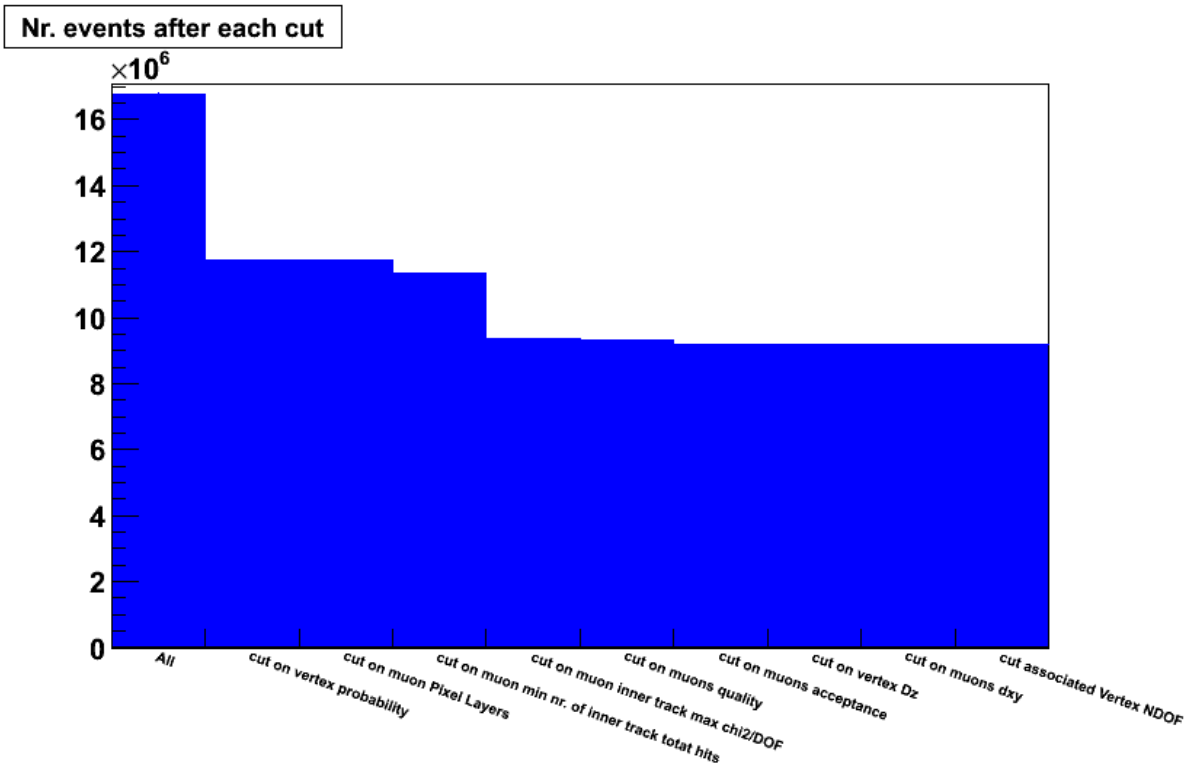

Figure 3.4: The effect of the *Soft* cuts on data.

requirements in GeV for p_T: $p_T > 3.5$ for $|\eta| < 1.2$; $p_T > -\frac{15}{4}|\eta| + 8$ for $1.2 < |\eta| < 1.6$; $p_T > 2$ for $1.6 < |\eta| < 2.4$. To minimize reconstruction inefficiencies only the dimuon

pairs with $|\eta| < 1.2$ were actually employed for the invariant mass fits of section 3.3.
In the inclusive results, for every run period the available dimuon transverse momentum has been cut in order to have the same p_T range ($8 < p_T < 72$ GeV/c) for J/ψ and ψ(2S). The resulting dataset consisted of $4.65 \cdot 10^6$ events.

3.3 Mass fit

The invariant mass distribution was fitted in order to estimate the background and signal contributions. Two different mass ranges for J/ψ and ψ(2S) were defined, due to differences between the triggers used in the two cases. The detector resolution for the dimuon reconstructed mass depends on the transverse momentum: higher p_T leads to a better resolution. To fit inclusively in p_T, a combination of two Crystal Ball distributions was chosen to model this effect. The Crystal Ball function is defined as follows:

$$C(x;\bar{x},\sigma,n,\alpha) = N \cdot \begin{cases} e^{-\frac{(x-\bar{x})^2}{2\sigma^2}} & \text{for } \frac{x-\bar{x}}{\sigma} > -\alpha \\ \left(\frac{n}{|\alpha|}\right)^n e^{-\frac{|\alpha|^2}{2}} \left(\frac{n}{|\alpha|} - |\alpha| - \frac{x-\bar{x}}{\sigma}\right)^{-n} & \text{for } \frac{x-\bar{x}}{\sigma} \leq -\alpha \end{cases} \qquad (3.1)$$

$$\text{where } N = \frac{1}{\sigma\left(\frac{n}{|\alpha|}\frac{1}{n-1}e^{-\frac{|\alpha|^2}{2}} + \sqrt{\frac{\pi}{2}}\left(1+\text{erf}\left(\frac{|\alpha|}{\sqrt{2}}\right)\right)\right)}$$

It consists of a Gaussian core portion and a power-law low-end tail, below a certain threshold, to account for radiation losses. The parameters α and n were keeped fixed respectively at 1.8 and 2.5 (values chosen from Monte Carlo), and the mean $\bar{x}$ was imposed to be the same for both distributions. Also the width (σ) of one of the two distribution was fixed to limit the number of floating parameters: 0.018 for J/ψ and 0.021 for ψ(2S). These values were determined fitting on the whole range of p_T and multiplicity. Thus, the only difference between them is in their widths σ_1 and σ_2.
The background instead was fitted with a decreasing exponential function $E(x;\lambda) = e^{-\lambda x}$, so that the final function was:

$$F = N_{SIG}C + N_{BKG}E \qquad (3.2)$$

An extended maximum likelihood fit has been used, to directly extract the number of signal and background events and their statistical errors.

3.4 Prompt/non-prompt separation

The data, together with background dimuons, include prompt and non-prompt ψ mesons. The non-prompt ψ mesons originate from decays of B^+, B^0 and B_s mesons or Λ^b baryons.

Given their lifetimes, these b-hadrons typically travel distances of the order of 500 μm before they decay to a ψ meson. Knowing this, the discrimination between prompt and non-prompt ψ mesons can be made thanks to the lifetime distribution [37], measured with very good accuracy in CMS. The variable used to resolve the prompt and non-prompt components is the "pseudo-proper lifetime" of the b-hadrons ("pseudo" because the full decay is not reconstructed) [39], defined as

$$\ell = L_{xy} m_{\psi} / p_T \tag{3.3}$$

where m_ψ is the ψ meson mass and L_{xy} is the most probable transverse decay length in the laboratory frame.

$$L_{xy} = \frac{\mathbf{u}^T \sigma^{-1} \mathbf{x}}{\mathbf{u}^T \sigma^{-1} \mathbf{u}} \tag{3.4}$$

where $\mathbf{x}$ the vector in the transverse plane from the primary vertex to the vertex generating the two muons, $\mathbf{u}$ the unit vector of the ψ meson p_T,and σ the sum of the covariance matrices of the primary and secondary vertices. The measurement of the prompt and non-prompt yields requires both the subtraction of the continuum background and the separation of the prompt and non-prompt signal components. The discrimination between the prompt and non-prompt signal can be made thanks to the fact that ℓ is distributed differently in the two cases, with a high exponential tail populated only by non-prompt charmonia, while both species are present next to $\ell = 0$. Furthermore, the presence of mass ranges with only background allows to evaluate separately its ℓ distribution.
The non-prompt distribution therefore has been modeled with a decreasing exponential function, and the background with a combination of five functions: a zero lifetime component, two positive slope exponential functions, a negative slope exponential function, and a symmetric exponential function with both positive and negative slopes. One positive slope exponential function is chosen to model the background from other long lived b-hadron events that produce opposite sign muons. The zero lifetime component is chosen to be a Dirac delta at $\ell = 0$, as well as the prompt component. The other exponential functions are added to parameterize the remaining components of the background pseudo-proper decay time distributions originating from unknown sources. Due to the resolution uncertainty the sum of all these three distributions have been convoluted with a resolution model function composed of two gaussians (only one for the ψ(2S)) and depending in width on the per-event error information:

$$\mathcal{F}_{TOT} = f_{BKG}\mathcal{F}_{BKG} + (1 - f_{BKG})(f_b \mathcal{F}_{NP} + (1 - f_b)\mathcal{F}_{PR}) \tag{3.5}$$

with

$$\begin{aligned}\mathcal{F}_{BKG} = \mathcal{F}_{res} \otimes ((f_{living}(f_{pm}(f_0 e^{-\ell\lambda_1}\theta(\ell) + (1 - f_0)e^{-\ell\lambda_2}\theta(\ell)) + (1 - f_{pm})e^{\ell\lambda_3}\theta(-\ell)) \\ +(1 - f_{living})(e^{\ell\lambda_4}\theta(-\ell) + e^{-\ell\lambda_4}\theta(\ell))))))(1 - f_3) + f_3\delta(0))\end{aligned} \tag{3.6}$$

$$\mathcal{F}_{NP} = \mathcal{F}_{res} \otimes e^{-\lambda_{NP}\ell}\theta(\ell) \tag{3.7}$$

$$\mathcal{F}_{PR} = \mathcal{F}_{res} \otimes \delta(0) \tag{3.8}$$

Where θ is the step function and the fractions f are used to parametrize all the various components.
To facilitate the fitting procedure some of the initial parameters were taken from Monte Carlo samples.

3.5 Sideband subtraction

Observable quantities (such as p_T) have been separately measured for the signal and the background by means of a "sideband subtraction". This is a subtraction of the observable distribution in the mass ranges containing only background ("sidebands") to the one obtained in the ψ(2S) and J/ψ zones, proportionally to the percentage of background present there, estimated thanks to the invariant mass distribution fit. The resulting distribution thus can be taken as the distribution of the signal only, and is the one used to calculate the mean p_T value.
The chosen mass boundaries for the signal were $2.95 < m < 3.21$ for J/ψ and $3.56 < m < 3.82$ for ψ(2S) (in GeV/c^2).
The same procedure has been applied to separate observables distributions from prompt and non-prompt signal, defining sidebands in the ℓ distribution instead. The chosen superimposition ranges, found to be p_T-dependent, of the prompt and non-prompt components were, in mm, $-0.21 < \ell < 0.41$ for J/ψ ($-0.15 < \ell < 0.21$ for $p_T \geq 17$ GeV/c) and $-0.08 < \ell < 0.18$ for ψ(2S) ($-0.06 < \ell < 0.11$ for $p_T \geq 17$ GeV/c).
Thanks to the mass fit, it is therefore possible to distinguish between background, J/ψ signal and ψ(2S) signal. In Fig. 3.5 and 3.6 the transverse momentum and rapidity of the two charmonium candidates are plotted as examples. An example of the difference between the signal and background p_T spectra is shown in Fig. 3.7: the background p_T is higher on average.

3.6 Acceptance

The acceptance corrections are needed to compensate the signal missed by the detectors for geometrical reasons. It is defined as:

$$A = \frac{events\ with\ two\ muons\ in\ acceptance}{all\ events} \tag{3.9}$$

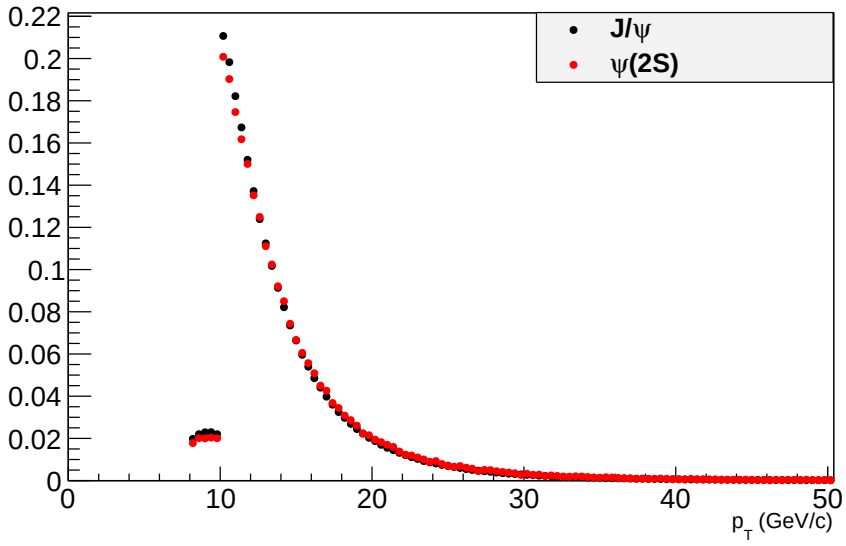

Figure 3.5: The resulting normalized p_T plot of the ψ(2S) and J/ψ candidates. The small values for $p_T < 10$ GeV/c are due to the lower integrated luminosity of the triggers used in this range.

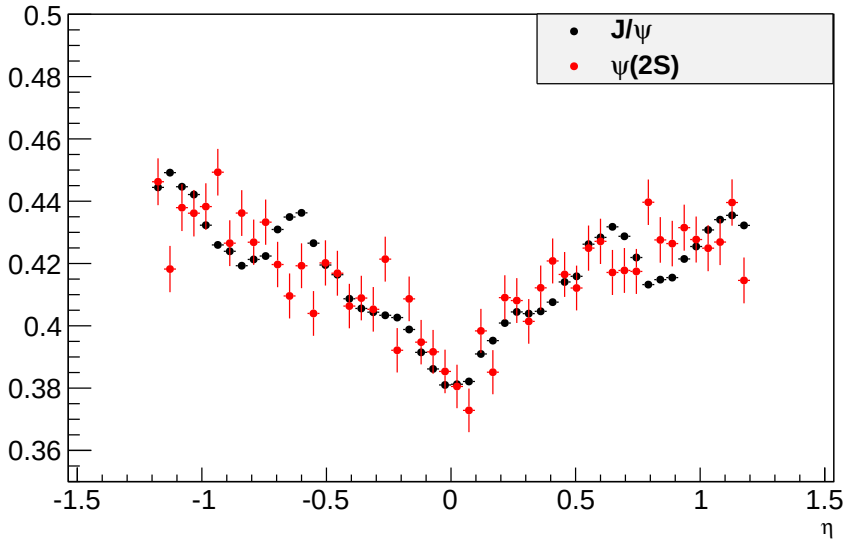

Figure 3.6: The resulting normalized η plot of the ψ(2S) and J/ψ candidates.

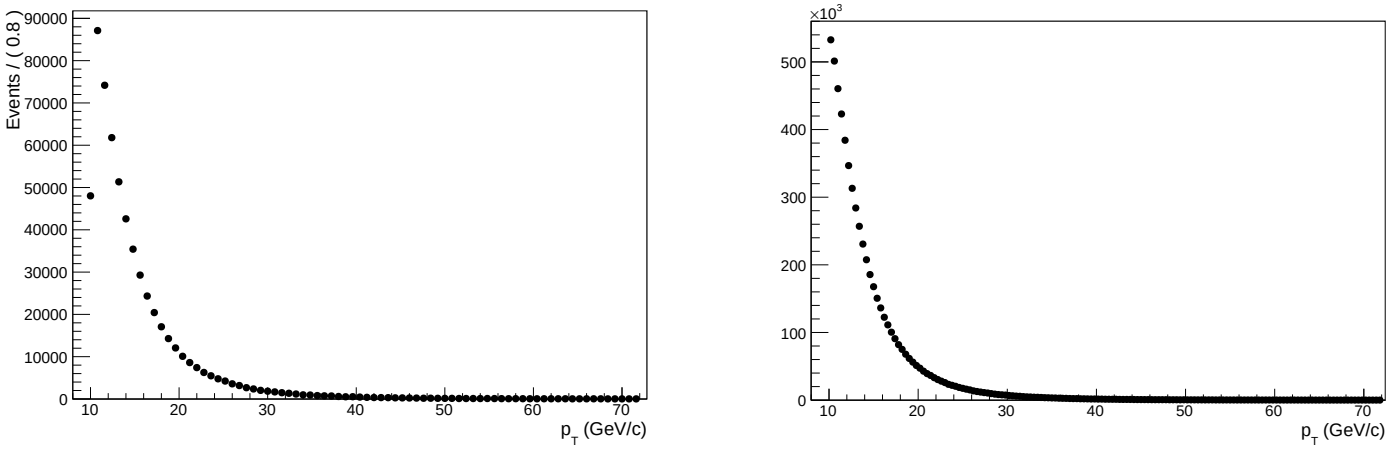

(a) (b)

Figure 3.7: An example of the p_T distributions for the background (a) and inclusive J/ψ (b) in the same bin.

They have been obtained estimating the signal loss for J/ψ and ψ(2S) with two different *particle gun* Monte Carlo, respectively. These latter consist of distributions of particles artificially generated without the initial interaction stages. They were produced with a uniform rapidity distribution in the range $|\eta| < 1.2$, according to the trends of previous J/ψ and ψ(2S) cross section measurements [35], and a realistic p_T distribution also obtained by previous analyses. The decay is simulated with EvtGen, using an isotropic decay, i.e. no preferred polarization, as no evidence for large polarizations has been found in the ranges used for this analysis [38]. The acceptance ranges applied on muons, as anticipated in section 3.2, are: $p_T > 3.5$ for $|\eta| < 1.2$; $p_T > -\frac{15}{4}|\eta| + 8$ for $1.2 < |\eta| < 1.6$; $p_T > 2$ for $1.6 < |\eta| < 2.4$, and in general $|\eta| < 2.4$. While on the dimuon pairs $|\eta| < 1.2$. The resulting values for J/ψ and ψ(2S) are shown in Fig. 3.8 (including the $|\eta|$ dependence) and 3.9, and the evaluation of the difference between their acceptances is shown in Fig. 3.10.

3.7 Efficiency

The efficiency represents the fraction of signal actually reconstructed by the detectors, while the loss is due to the applied selections and to recostruction inefficiencies of the detectors. It is defined as:

$$\varepsilon = \frac{reconstructed\,events}{in\text{–}acceptance\,events} \tag{3.10}$$

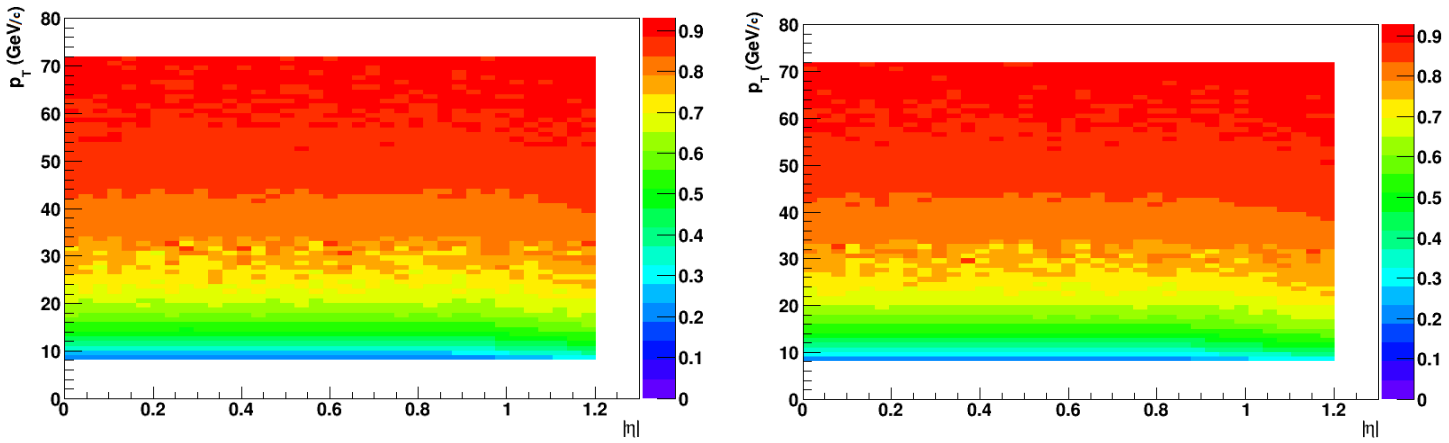

(a) (b)

Figure 3.8: Acceptance for J/ψ (a) and ψ(2S) (b) as a function of $|\eta|$ and p_T.

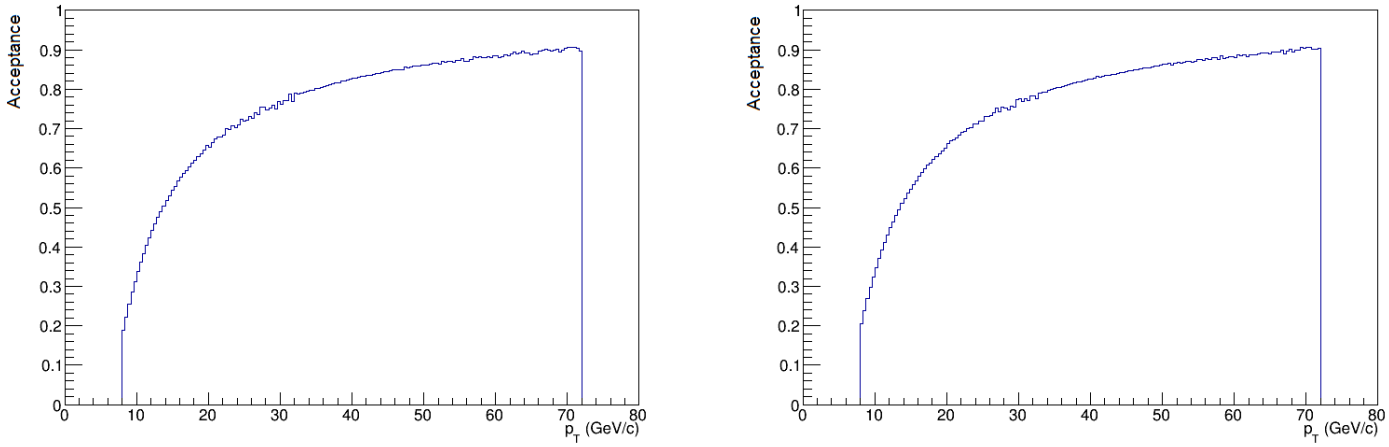

(a) (b)

Figure 3.9: Acceptance for J/ψ (a) and ψ(2S) (b) as a function of p_T.

First of all the reconstruction efficiency is evaluated for the single muons. The combined trigger and offline-reconstruction efficiency for a single muon is factorized as

$$\epsilon = \epsilon_{track} \cdot \epsilon_{ID} \cdot \epsilon_{trig} \tag{3.11}$$

where ϵ_{track} is the tracking efficiency, ϵ_{ID} is the muon identification efficiency in the muon systems for a tracker-reconstructed muon, and finally ϵ_{trig} is the probability for an offline

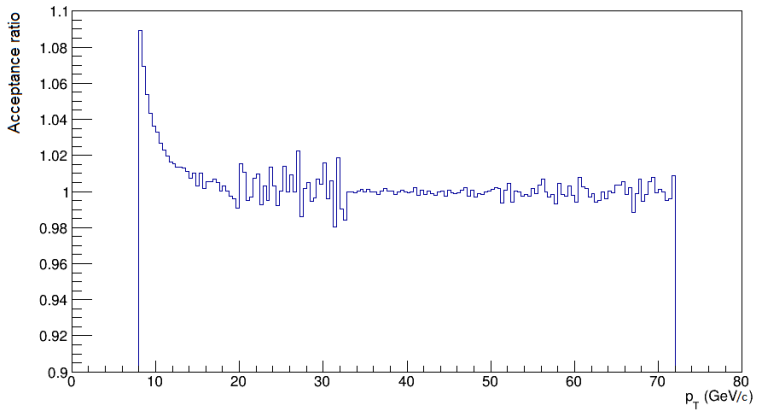

Figure 3.10: Ratio of $\psi(2S)$ and J/ψ acceptances as a function of p_T.

reconstructed muon to have also fired the trigger. The informations on the efficiency corrections for J/ψ and $\psi(2S)$ have been collected from efficiency maps obtained with the "Tag and Probe" method. Using this technique, valid for the reconstruction of any dimuon resonance, events are selected with strict selection requirements on one muon (the "tag" muon), and with a more relaxed selection on the other muon (the "probe" muon), such that the selection applied to the probe muon does not bias the efficiency that one wants to measure. The probe muons are separated into two categories depending on whether they pass or fail the more restrictive selection. For example, to measure

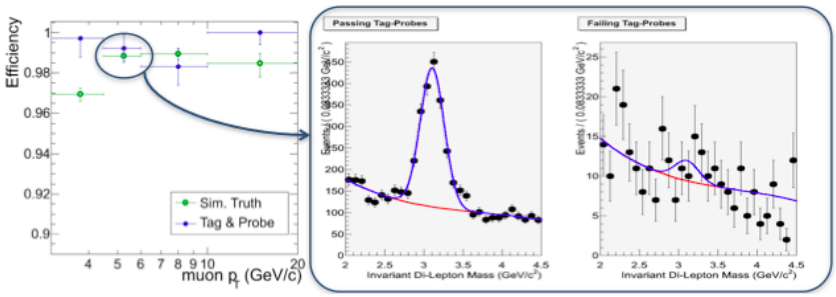

Figure 3.11: Difference between passing and non passing probes in the invariant mass fit.

trigger efficiency, probe muons would be separated into those that pass or fail the given trigger requirements. To measure tracking efficiency, probe muons are reconstructed using information only from the muon detector system, and then are defined passing and failing as those that are or are not matched to tracks in the inner tracker, respectively. At the end, the efficiency is computed as the ratio of the two signal yields, fitting the distributions with a signal plus background model, like in Fig. 3.11. The tag and

probe categories are not mutually exclusive: in cases where both muons of a dimuon pair satisfy both criteria the two combinations are considered independently, to produce more statistical information. The efficiency values obtained in this way are shown in Fig. 3.12, and their p_T profile in Fig. 3.13.

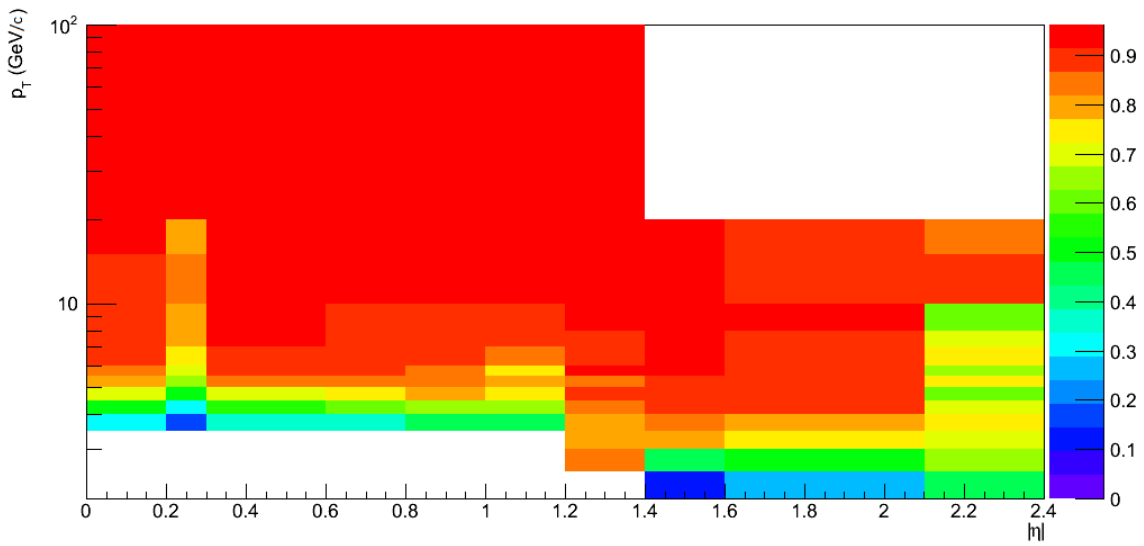

Figure 3.12: The resulting combined efficiency for muons.

This efficiency is then multiplied to the ρ factor (see Fig. 3.14), a correction to the factorization hypothesis evaluated from a Monte Carlo simulation. It is expressed as a function of $\Delta R^{elliptic}_{\Delta p_T} = \sqrt{(0.00157(p_{TH} - p_{TS}))^2 + (\eta_H - \eta_S)^2 + (\phi_H - \phi_S)^2}$, where the H and S labels are for the muons with higher and lower p_T. The deviations from unity of ρ are mainly due to the relatively large bin sizes used to determine the muon efficiencies, that lead to a larger degree of approximation.

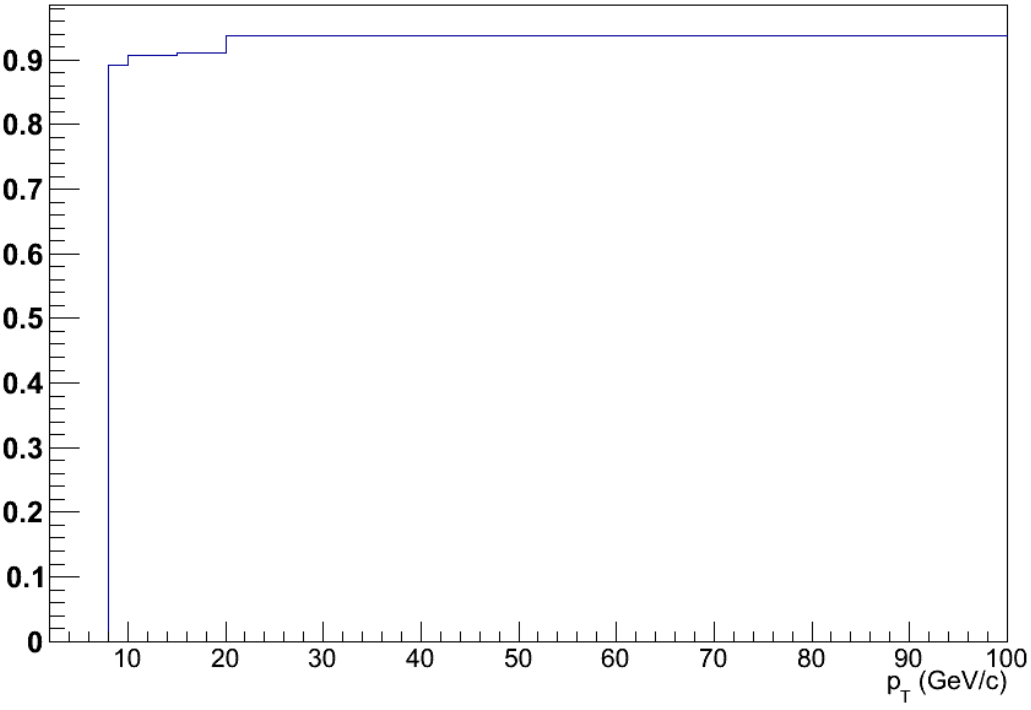

Figure 3.13: The p_T profile of the efficiency, calculated in the same ranges of the acceptance.

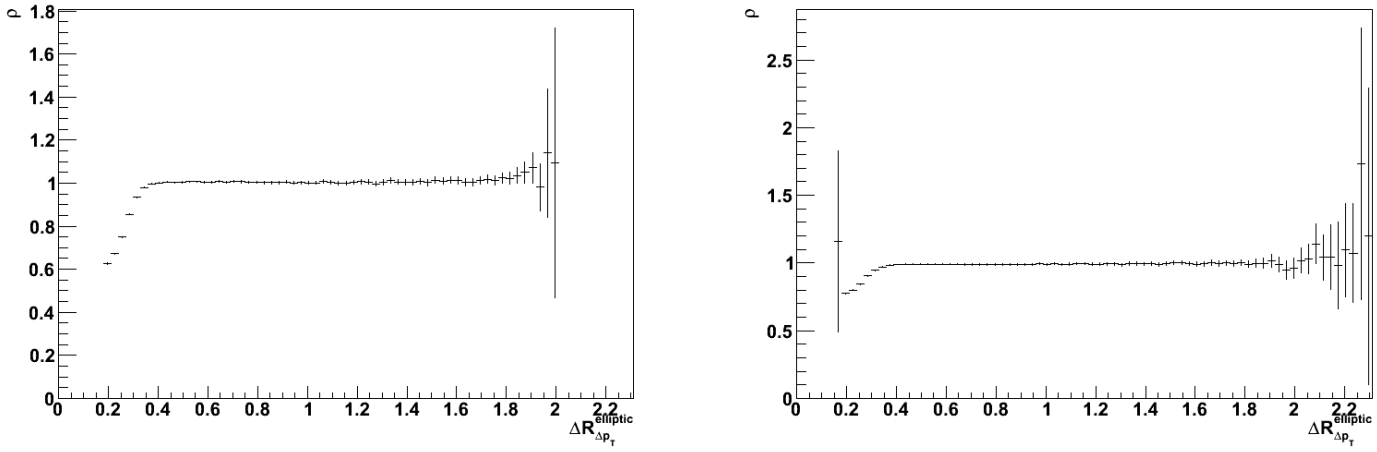

(a) (b)

Figure 3.14: ρ factors for $|y| < 0.6$. (a) and $|y| \geq 0.6$ (b).

3.8 Comparison with published results

In Fig. 3.15 the ratio between the prompt ψ(2S) and J/ψ yields has been evaluated as a function of p_T, and compared with a previous published result also obtained with data from the CMS experiment [39], see Tab. 3.2. The focus of that study was the p_T dependence of charmonium production, therefore it makes use of yields collected with different trigger choices aiming at higher transverse momenta. However, the ψ(2S)/J/ψ ratio approximately cancels out the effects of these selections, so that they are still eligible for a comparison.
The two results are compatible except for the last bins, but this could be due to the lower statistics in the datasets used for this analysis.

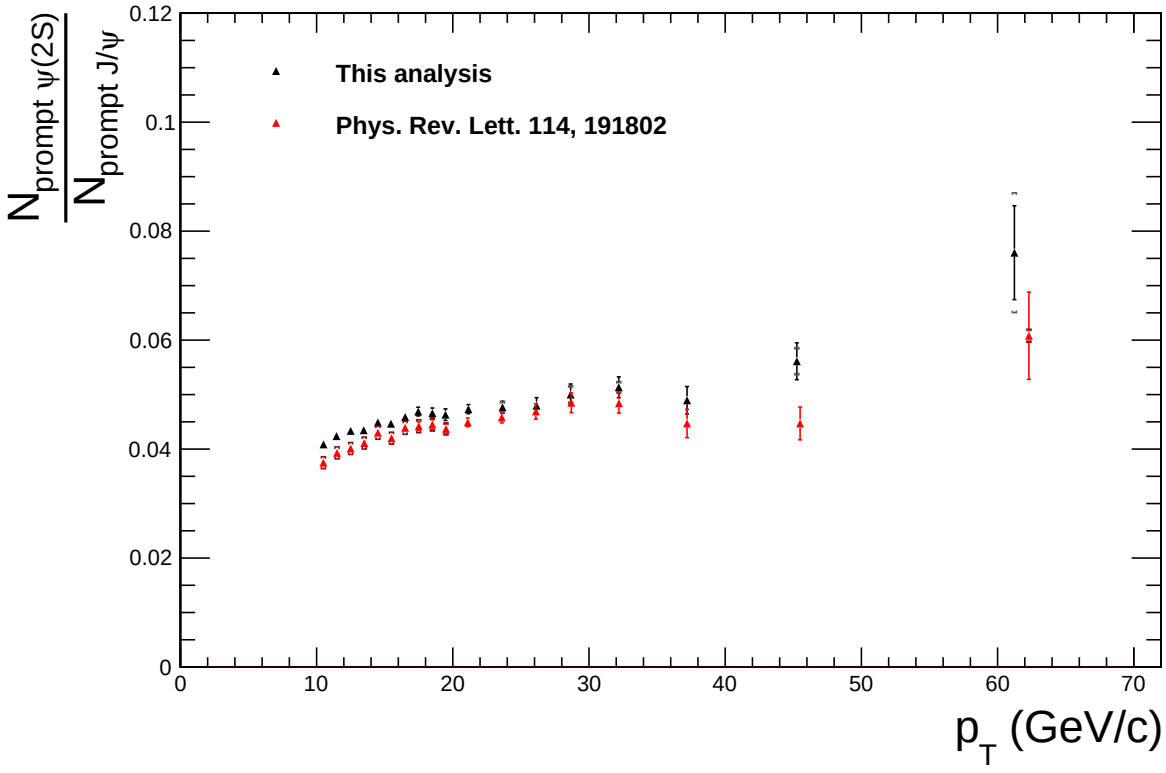

Figure 3.15: Comparison of the ψ(2S)/J/ψ ratios with previous results.

$\mathbf{p_T}$ bin	$\langle \mathbf{p_T} \rangle$	Ratio	$\langle \mathbf{p_T} \rangle$	Ratio
10-11	10.5	0.0389±0.0003±0.0005	10.5	0.0375±0.0003±0.0011
11-12	11.5	0.0413±0.0004±0.0002	11.5	0.0393±0.0003±0.0011
12-13	12.5	0.0429±0.0004±0.0003	12.5	0.0401±0.0004±0.0011
13-14	13.5	0.04331±0.00045±0.00005	13.5	0.0411±0.0004±0.0011
14-15	14.5	0.04478±0.00053±0.00019	14.5	0.043±0.0005±0.0012
15-16	15.5	0.0444±0.0006±0.0002	15.5	0.042±0.0006±0.0011
16-17	16.5	0.0453±0.0007±0.0007	16.5	0.0439±0.0007±0.0012
17-18	17.5	0.04592±0.00079±0.00018	17.5	0.0442±0.0008±0.0012
18-19	18.5	0.04516±0.00090±0.00019	18.5	0.0445±0.0009±0.0012
19-20	19.5	0.0444±0.0010±0.0005	19.5	0.0437±0.001±0.0011
20-22.5	21.1	0.0444±0.0008±0.0005	21.1	0.0449±0.0008±0.0005
22.5-25	23.6	0.0435±0.0010±0.0010	23.6	0.0458±0.001±0.0005
25-27.5	26.1	0.04289±0.00132±0.00001	26.1	0.0469±0.0014±0.0004
27.5-30	28.7	0.0444±0.0017±0.0015	28.7	0.0485±0.0018±0.0005
30-35	32.2	0.0460±0.0017±0.0010	32.2	0.0484±0.0018±0.0005
35-40	37.2	0.04229±0.00228±0.00010	37.2	0.0447±0.0026±0.0005
40-55	45.3	0.0352±0.0036±0.0014	45.5	0.0447±0.003±0.0004
55-75	61.2	0.049±0.011±0.006	62.3	0.0608±0.008±0.0012

Table 3.2: Data from Fig. 3.15. p_T is expressed in GeV/c

Chapter 4

Multiplicity evaluation

In this chapter the evaluation of charged particle multiplicity will be discussed, i.e. the number of primary charged particles produced in the collision, that has to be associated with each dimuon pair. Primary particles are defined as prompt particles produced in the collision, including also decay products, except those from directly observable decays, with a measurable decay length. In particular, the latter consist of weak decays of strange particles.
A production vertex is associated to each dimuon candidate, choosing in the collection of primary vertices the most fitting to the reconstructed 3D path of the candidate. The events will be classified according to the multiplicity of charged tracks coming from the primary vertex and the transverse momentum of the charmonium. Efficiency and acceptance corrections will be applied to the yields sorted in this way.

4.1 Track reconstruction

The track reconstruction method [28] is decisive for the evaluation of the charged multiplicity. This analysis is based on the standard CMSSW reconstruction procedure.
The first step is the clustering of signals above specified thresholds from pixel and strip tracker layers into "hits", and then estimating the cluster positions and their uncertainties with a local orthogonal coordinate system in the plane of each sensor. To reconstruct the trajectories using the hits, the tracking software used at CMS is the Combinatorial Track Finder (CTF), which is based on the *Kalman filter* [25]. After each iteration of this algorithm, hits associated with tracks are removed, thereby simplifying subsequent iterations in a search for more difficult classes of tracks, having lower p_T or a greater displacement from the beam spot.
Each iteration proceeds in four steps:

- seed generation provides initial track candidates found using only a few hits. A "seed" defines the initial estimate of the trajectory parameters and their uncertain-

ties. They are constructed in the inner part of the tracker starting from three 3D hits (or two plus the origin), and then track candidates are built by searching outwards for additional matching hits. To limit the number of hit combinations, seeds are required to satisfy certain weak restrictions, for example, on their minimum p_T and their compatibility with the interaction point;

- track finding, using a Kalman filter. It begins with a coarse estimate of the track parameters provided, extrapolating the seed trajectories along the expected flight path of a charged particle. Then it determines which adjacent layers of the detector can be intersected (with enough relevance) and adds one hit from successive layers with a χ^2 test, considering also the possibility of creating a "ghost hit" to represent a possible undetected hit. The track parameters are updated at each layer;

- the track fitting module is used to provide the best possible estimate of the parameters of each track by means of a Kalman filter refitting and a Runge-Kutta propagator to extrapolate and smooth the trajectory from one hit to the next. After this a search is made for spurious hits incorrectly associated to the track. This step is also important to avoid the estimate to be biased by constraints, such as the ones applied during the seeding stage;

- track selection sets quality flags, and discards tracks that fail certain specified criteria to reduce fake rate. The requirements are on the number of layers with or without hits, the trajectory χ^2, and how compatible they are with originating from a primary interaction vertex, considering all of them.

The iterations are not performed in the same way; they differ mainly in the configuration of the seed generation and in the final track selection. Variants of this software are also used for more specialized purposes, for example fast track reconstruction for the high-level trigger.

4.2 Vertex reconstruction

Primary vertices are reconstructed measuring the location, and the associated uncertainty, of all proton-proton interaction vertices in each event. Any vertex from "pile-up" collisions is included, using the available reconstructed tracks. These are events where multiple collisions occur, consequently making the vertex reconstruction more problematic.
This procedure also consists of some steps:

- selection of the tracks consistent with being produced promptly in the primary interaction region, with requirements on the transverse impact parameter, the number of hits associated with a track and the trajectory χ^2;

- clustering of the tracks that appear to originate from the same interaction vertex on the basis of their z coordinates at their point of closest approach to the centre of the beam spot. It is performed using a *deterministic annealing* (DA) algorithm [26], finding the global minimum for a problem with many degrees of freedom, in an analogous way to that of a physical system approaching a state of minimal energy through a series of gradual temperature reductions. To minimize track misassignments, candidate vertices are retained only if at least two of their tracks are incompatible with originating from other vertices, then the rejected tracks are reassigned;

- fitting for the position of each vertex using its associated tracks with an *adaptive vertex fitter*. Other parameters obtained and saved are the covariance matrix, the indicators for the quality of the fit, such as the number of degrees of freedom for the vertex, and weights of the tracks used in the vertex. The latter quantify the consistency of the track with a vertex and thus how much it contributed to its reconstruction, varying between 0 and 1. The more a track is consistent with the position of the reconstructed vertex, the more its weight is close to 1.

The resulting vertex number, nearest vertex distance and z axis distributions, obtained with the conditions listed in the next section except for the last four, are shown in Fig. 4.1 and 4.2.

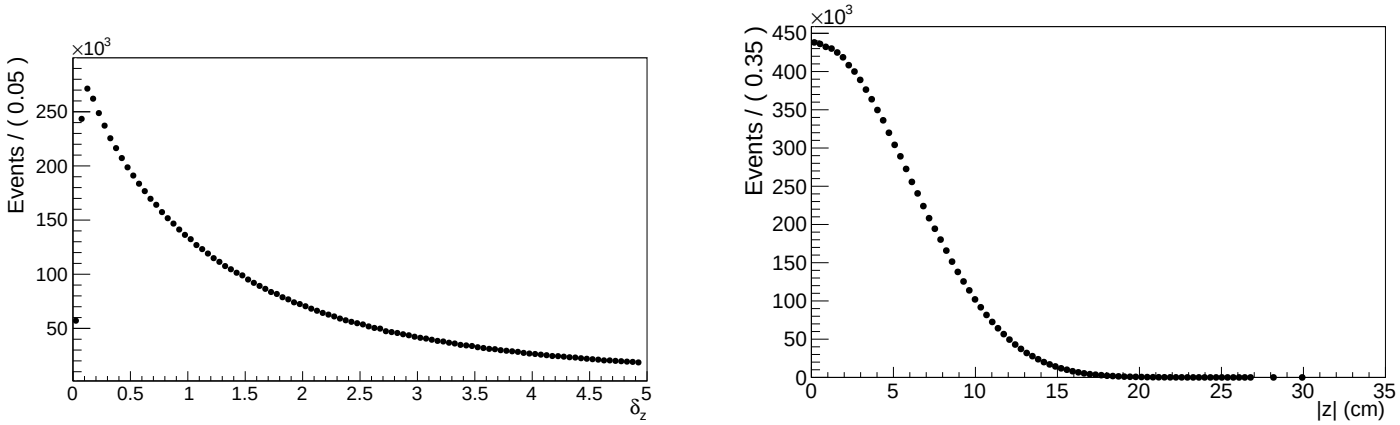

Figure 4.1: The distributions of the nearest vertex distance (a) and z axis position (b) in the analyzed dataset.

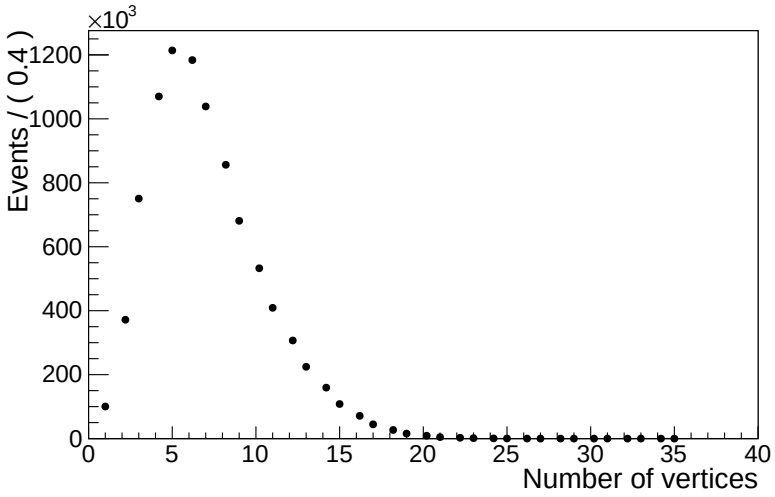

Figure 4.2: The distribution of the vertices number in the analyzed dataset.

4.3 Vertex and track selection

In the last step of the reconstruction, the variable number of degrees of freedom (N_{DOF}) is defined as the sum over the weights associated to the tracks of a vertex:

$$N_{DOF} = 2 \sum_i w_i - 3 \tag{4.1}$$

where w_i are the track weights. Thus, the number of degrees of freedom of the vertex can be used to select likely real proton-proton interactions. In this analysis the minimum N_{DOF} cut has been set to $N_{DOF} > 0.5$. In a second time, additional selections on vertices are added:

1. distance to the nearest vertex $\delta_z \leq 0.2$ cm;
2. distance of the vertex from the detector center $|z| \leq 10$ cm;
3. number of vertices ≤ 15;

Thanks to the second condition, only vertices in the central part of the detector z, where track reconstruction efficiency is higher, are selected. The other two conditions are meant to counteract the effects of track pile-up: the first avoids misassignment of tracks, the third reduces the risk of vertex merging. Once only events with valid vertices pass the selection, conditions are imposed on the collection of the tracks used for their reconstruction:

1. track $\delta p_T / p_T < 10\%$;

2. track $|\eta| < 2.4$;

3. track $p_T > 0.4$ GeV/c;

4. track $w_i > 0.5$;

5. w_i for the vertex associated to the charmonium should be the highest with respect to its weights for the other vertices in the event;

6. the track weighted distance to the vertex associated to the charmonium (thus to the dimuon pair) should be the lowest with respect to the other vertices in the event.

The multiplicity distribution from a 2011 Minimum Bias dataset has also been used as a reference in the following analysis. Minimum Bias is a generic term which refers to events that are selected with a loose trigger, in this case *HLT_ZeroBias*, that accepts a large fraction of the overall inelastic cross section.
The number of tracks obtained after these cuts, for the nearest primary vertex associated to the charmonium candidate is referred to as the observed multiplicity, N_{ch}. $\frac{dN_{ch}}{d\eta}$ will correspond on average to $N_{ch}/4.8$, as the tracks $|\eta| < 2.4$.
After this procedure, the charged multiplicity distribution varied as shown in Fig. 4.3. As can be seen, the mean value changes significantly.

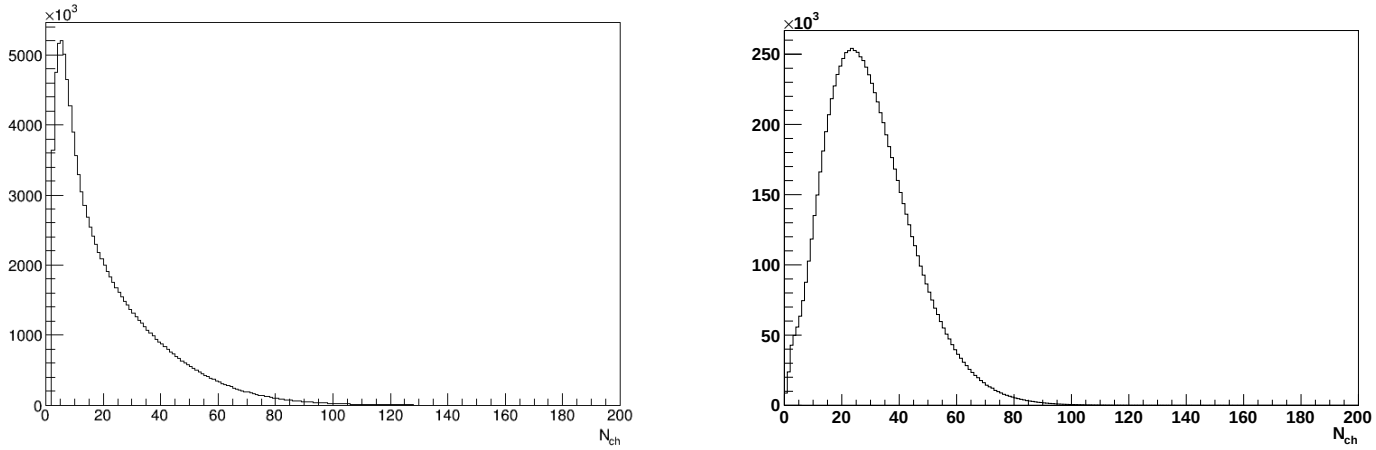

(a) (b)

Figure 4.3: Multiplicity distribution before (a) and after (b) the selections for the data.

4.4 Efficiency corrections

A Monte Carlo simulation has been used to associate recostructed tracks with "true" ones. Reconstructed tracks that do not correspond to a real particle path are referred to as fake tracks, and their fraction on the total is called fake rate; the ineffieciency is instead represented by the fraction of real particles not reconstructed. In this way, p_T vs $|\eta|$ map of the efficiencies and fake rates of the reconstructed tracks (with the same selections above) has been obtained (Fig. 4.4) and used to correct the number of tracks, with the following weight:

$$w_{track} = \frac{1 - track_{fake}}{track_{eff}} \tag{4.2}$$

The final multiplicity distribution after these corrections is shown in Fig. 4.5. The same

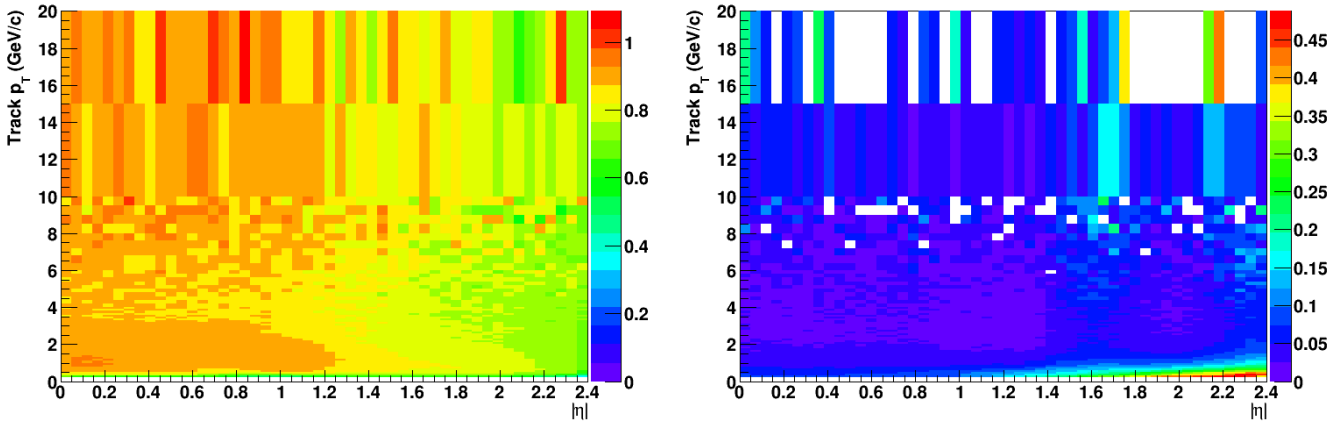

(a) (b)

Figure 4.4: Efficiencies (a) and fake rate (b) maps for the tracks.

corrections, together with the conditions described in the previous section, have been applied to the Minimum Bias dataset (Fig. 4.6).

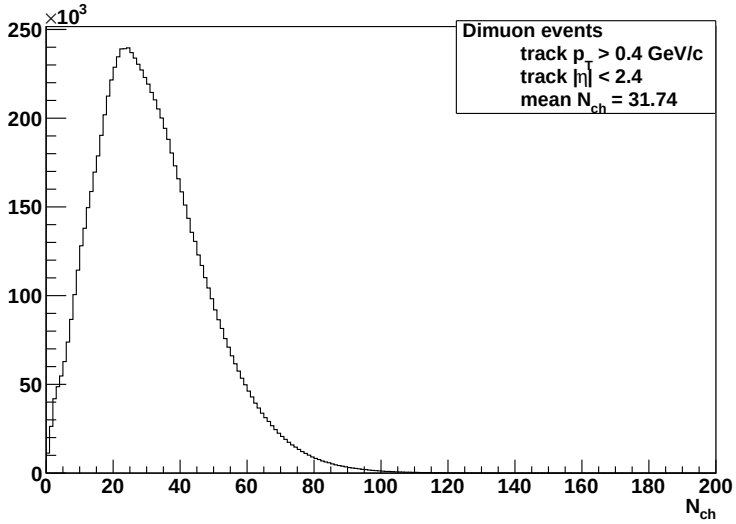

Figure 4.5: The final multiplicity distribution after the efficiency and fake rate corrections.

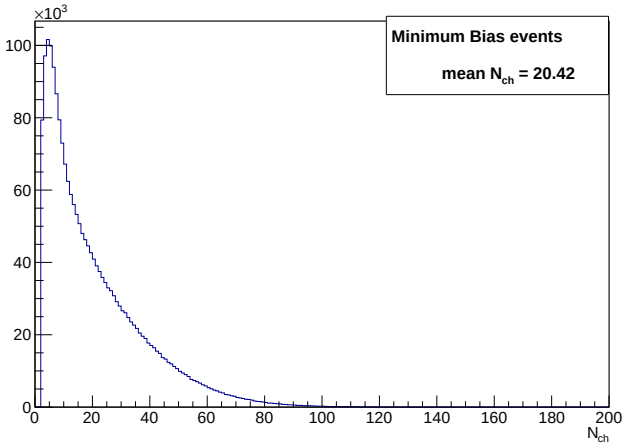

(a)

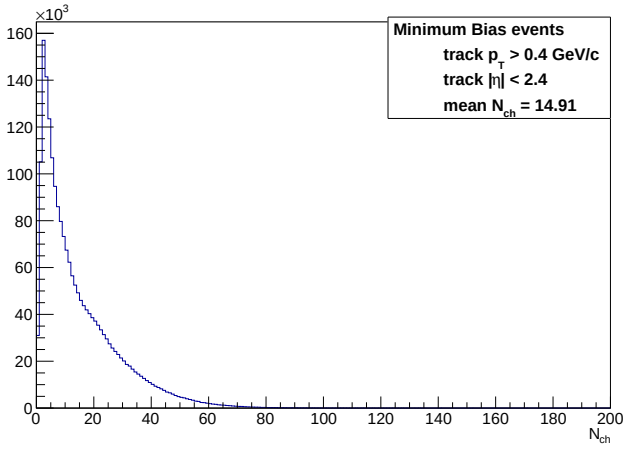

(b)

Figure 4.6: Multiplicity distribution and number of events before and after the selections and corrections for the Minimum Bias dataset.

4.5 Monte Carlo comparison

To understand the effect of the previously described selections and corrections, they have been applied to a Monte Carlo dataset and the deviations from truth have been plotted in Fig. 4.7. This dataset had been generated with PYTHIA 6 - tune Z2, which contains a tune on LEP and Tevatron data.
The multiplicity bins used in the following data analysis are listed in Table 4.1, together with their mean value and the respective original value extrapolated from the map in Fig. 4.7a. The mean has been calculated as a weighted mean with respect to J/ψ and ψ(2S) yields.
This comparison aims to reconstruct the contribution of tracks with $p_T < 0.4$ GeV/c, excluded by the track selections. In Fig. 4.7b instead the p_T cut is also used for the generated tracks; this makes the correspondence quasi-linear at 45°, as expected.

Bin	0-7	7-13	13-18	18-22	22-25	25-30	30-35	35-45	45-55	55-150
Measured average	4.5	10.4	15.6	20.0	23.5	27.5	32.4	39.6	49.5	66.3
MC truth ($p_T > 0$)	17.6	27.7	35.5	41.4	47.4	53.2	60.2	69.7	81.6	98.5
MC truth ($p_T > 0.4$)	8.2	15.1	20.7	25.1	29.8	34.3	39.8	47.4	57.6	71.8

Table 4.1: Multiplicity bins, mean values and respective true values.

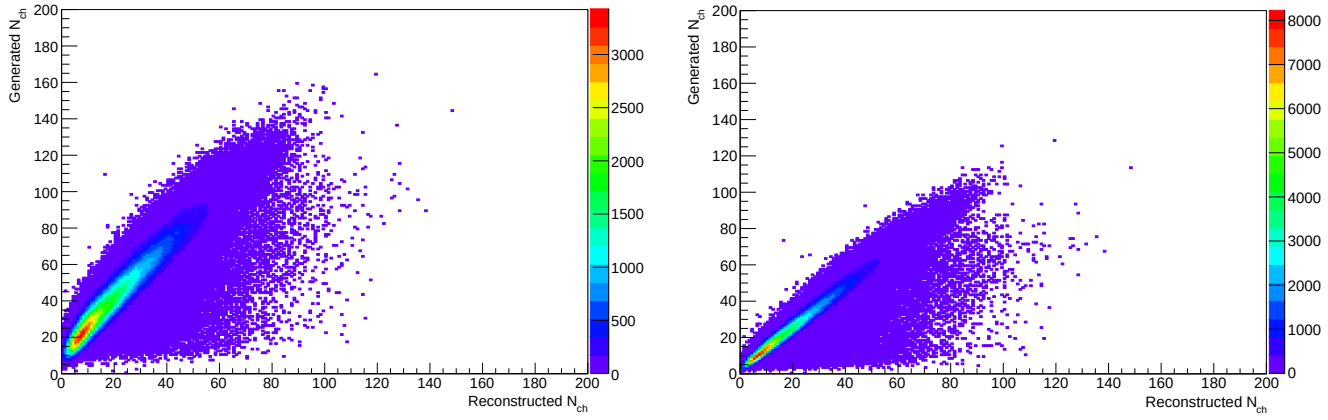

(a) (b)

Figure 4.7: Maps of generated multiplicity vs reconstructed multiplicity, the latter with respectively $p_T > 0$ and > 0.4 GeV/c for the tracks. All the other selections used for the data were applied.

Chapter 5

Results

In this chapter, the selected data will be classified and studied according to the event multiplicity, whose evaluation is described in chapter 4. The various yields are extracted as described in chapter 3. Efficiency and acceptance corrections will be subsequently applied as explained in sections 3.6 and 3.7.
In the following analysis, systematic uncertainties will be indicated by horizontal delimiters for every plot point (if not negligible) and by the second error in tables.

5.1 Inclusive prompt studies

First of all, the multiplicity bins have been chosen in order to keep enough information, according to the distribution of Fig. 4.5, for every interval to obtain acceptable statistical errors. Their reference value is the average multiplicity in the bin, calculated as a weighted mean with respect to J/ψ and ψ(2S) yields.
Some examples of the fit results on data are shown in Fig. 5.1 and 5.2.

5.1.1 Efficiency corrections

After having computed the efficiencies for the single muons as described in section 3.7, they have been multiplied two by two to obtain dimuon efficiencies, and then the ρ factor has been applied for every candidate. An efficiency distribution has thus been obtained for every data range (see Fig. 5.3), from which the average value has been calculated for every multiplicity bin (Tab. 5.1). Also the ratio between ψ(2S) and J/ψ efficiencies has been evaluated, proving to be rather constant. The effect of efficiency corrections on results can be visualized in Tab. 5.2, applied to the ψ(2S)/J/ψ ratio and to the ratio between this value at lower multiplicities ($N_{ch} \leq 12$) and the one at higher ($N_{ch} > 30$).

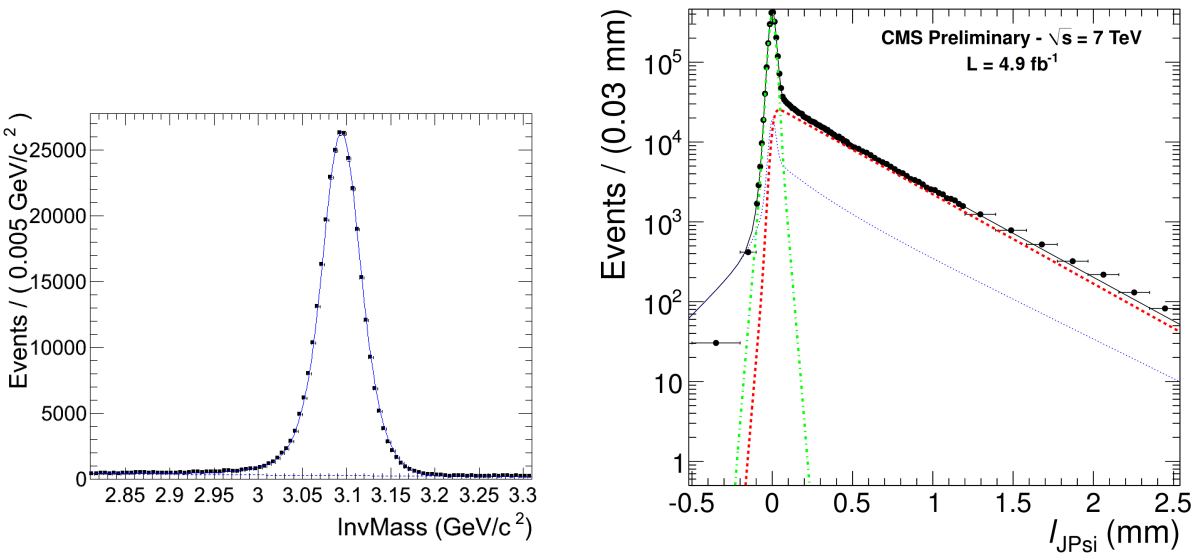

(a) (b)

Figure 5.1: Examples of mass and ℓ fit for J/ψ at low (12-18) multiplicity.

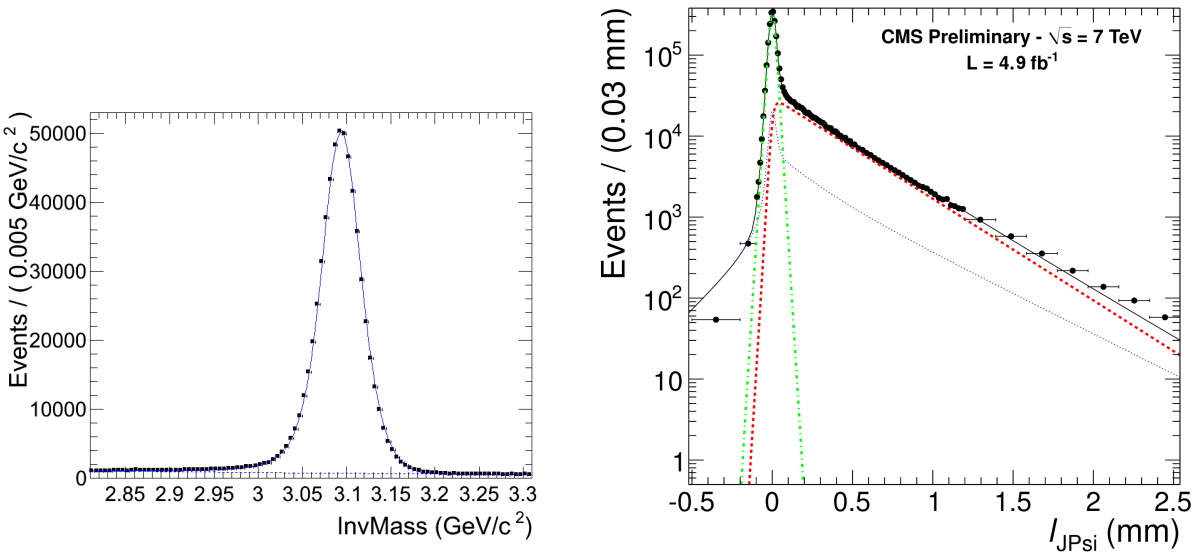

(a) (b)

Figure 5.2: Examples of mass and ℓ fit for J/ψ at high (55-150) multiplicity.

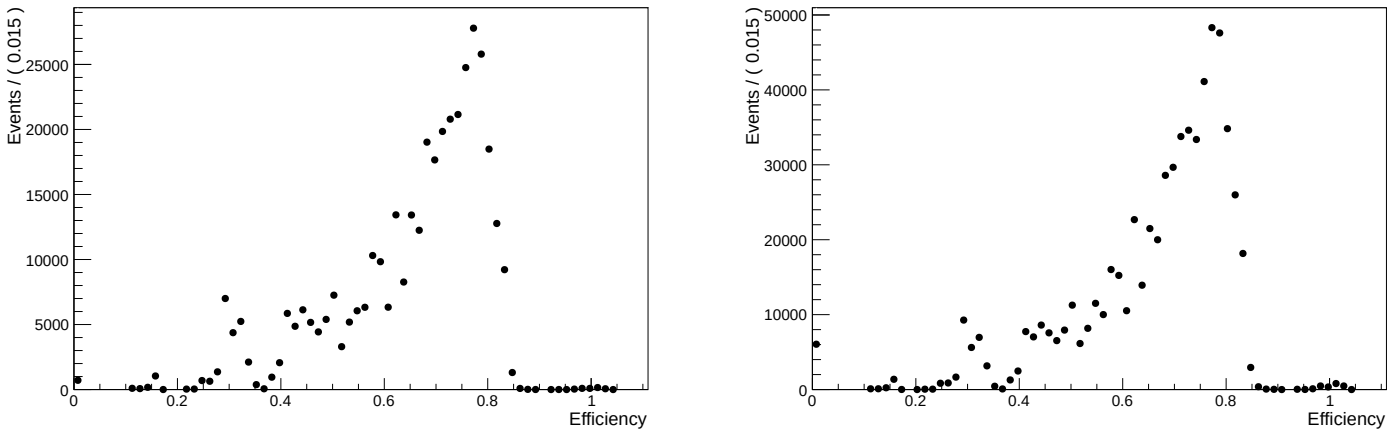

(a) (b)

Figure 5.3: Two examples of the dimuon efficiency distributions within a bin, for the J/ψ.

$\mathbf{N_{ch}}$ **bin**	J/ψ **efficiency**	ψ(2S) **efficiency**	$\mathbf{eff}_{\psi(2S)}/\mathbf{eff}_{J/\psi}$
0-7	0.6587±0.0013	0.6704±0.0012	1.018±0.003
7-13	0.6593±0.0011	0.6713±0.0010	1.018±0.002
13-18	0.6597±0.0009	0.6720±0.0009	1.0186±0.0019
18-22	0.6601±0.0008	0.6726±0.0008	1.0190±0.0018
22-25	0.6604±0.0008	0.6731±0.0008	1.0192±0.0017
25-30	0.6608±0.0008	0.6737±0.0007	1.0195±0.0016
30-35	0.6612±0.0008	0.6743±0.0008	1.0199±0.0017
35-45	0.6618±0.0010	0.6753±0.0009	1.020±0.002
45-55	0.6627±0.0013	0.6767±0.0012	1.021±0.003
55-150	0.6641±0.0019	0.6791±0.0018	1.022±0.004

Table 5.1: Efficiency corrections for J/ψ and ψ(2S).

$\mathbf{N_{ch}}$ **bin**	**Uncorrected** ψ(2S)/J/ψ **ratio**	**With efficiency corrections**
0-7	0.0491±0.0011	0.0483±0.0011
7-13	0.0477±0.0005	0.0469±0.0006
13-18	0.0464±0.0005	0.0456±0.0005
18-22	0.0461±0.0005	0.0453±0.0005
22-25	0.0444±0.0005	0.0435±0.0005
25-30	0.0440±0.0004	0.0431±0.0004
30-35	0.0431±0.0004	0.0422±0.0004
35-45	0.0418±0.0003	0.0409±0.0003
45-55	0.0409±0.0004	0.0401±0.0004
55-150	0.0403±0.0005	0.0394±0.0005
High/Low ratio	0.885±0.008	0.883±0.008

Table 5.2: Efficiency correction on "raw" prompt ψ(2S)/J/ψ ratios.

5.1.2 Acceptance corrections

The starting dimuon acceptance definition has been described in section 3.6. In this analysis for every p_T and N_{ch} interval its mean acceptance correction is considered (averaged also in the whole η interval as its distribution is approximately uniform), distinguishing between ψ(2S) and J/ψ. A weighted mean was thus used, with weights deriving from the prompt/non-prompt/inclusive signal yields as a function of p_T, obtained as explained in section 3.5. For p_T plots the acceptance distribution has been instead applied bin by bin. The acceptance corrections and their effect on results can be visualized in Tab. 5.3 and 5.4. Similarly to the efficiency, the ratio between ψ(2S) and J/ψ acceptances has been evaluated, and resulted to be quite constant too. For this reason the trend of the ψ(2S)/J/ψ ratio can be considered independent from acceptance and efficiency corrections.

$\mathbf{N_{ch}}$ **bin**	J/ψ **acceptance**	ψ(2S) **acceptance**	$\mathbf{acc_{\psi(2S)}/acc_{J/\psi}}$
0-7	0.467±0.003	0.477±0.002	1.022±0.008
7-13	0.471±0.002	0.482±0.002	1.022±0.006
13-18	0.4752±0.0018	0.4858±0.0017	1.022±0.005
18-22	0.4785±0.0016	0.4893±0.0015	1.022±0.005
22-25	0.4812±0.0015	0.4921±0.0014	1.023±0.004
25-30	0.4843±0.0013	0.4952±0.0013	1.023±0.004
30-35	0.4881±0.0013	0.4992±0.0012	1.023±0.004
35-45	0.4934±0.0014	0.5049±0.0014	1.023±0.004
45-55	0.5011±0.0019	0.5127±0.0019	1.023±0.005
55-150	0.514±0.003	0.526±0.003	1.023±0.008

Table 5.3: Acceptance corrections on prompt J/ψ and ψ(2S).

$\mathbf{N_{ch}}$ **bin**	**Without acceptance corrections**	**With acceptance corrections**
0-7	0.0483±0.0011	0.0472±0.0011
7-13	0.0469±0.0006	0.0458±0.0006
13-18	0.0456±0.0005	0.0446±0.0005
18-22	0.0453±0.0005	0.0443±0.0005
22-25	0.0435±0.0005	0.0426±0.0005
25-30	0.0431±0.0004	0.0422±0.0004
30-35	0.0422±0.0004	0.0413±0.0004
35-45	0.0409±0.0003	0.0400±0.0004
45-55	0.0401±0.0004	0.0392±0.0005
55-150	0.0394±0.0005	0.0385±0.0006
High/Low ratio	0.883±0.008	0.883±0.008

Table 5.4: Acceptance correction on prompt ψ(2S)/J/ψ ratios, already corrected with the efficiency.

5.1.3 Inclusive prompt results

First of all, the non-prompt fraction (the "B fraction", obtained fitting on ℓ) has been evaluated for all the multiplicity bins except the first one, where the ℓ fit was not correctly appliable because the reduced number of tracks gave rise to an inaccurate ℓ distribution due to vertex misidentifications. For this reason it has been extrapolated from the other bins with a polynomial fit (see Fig. 5.4).
The number of the prompt J/ψ and ψ(2S) produced has been obtained (see Tab. 5.5).

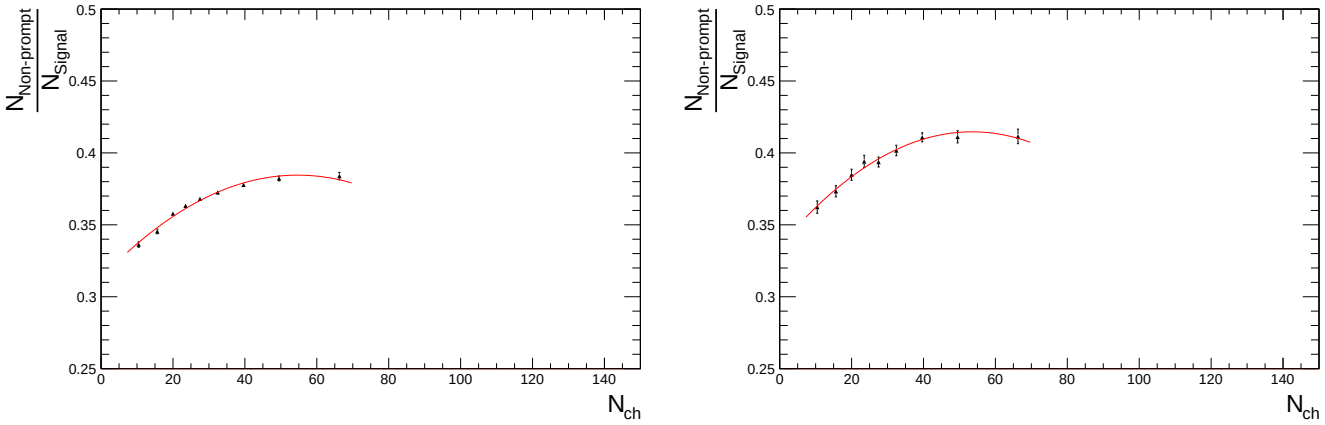

(a) (b)

Figure 5.4: B fraction for J/ψ (a) and ψ(2S) (b), excluding the first point.

N_{ch} bin	J/ψ **yield** ($\times 10^3$)	ψ(2S) **yield** ($\times 10^2$)
0-7	330±5±5	156±3±3
7-13	968±5±11	444±54±6
13-18	1241±6±14	554±6±7
18-22	1223±5±14	542±6±8
22-25	970±4±11	413±5±5
25-30	1541±5±18	650±6±9
30-35	1389±5±16	573±6±8
35-45	2117±7±25	847±7±12
45-55	1230±6±14	482±5±8
55-150	1066±7±13	411±5±7

Table 5.5: Prompt J/ψ and ψ(2S) yields.

The ratio between prompt ψ(2S) and J/ψ production has then been plotted as a function of N_{ch} (see Fig. 5.5b) and of $\frac{dN_{ch}}{d\eta}$ (Fig. 5.6). The latter has been reconstructed for $p_T > 0$ from a Monte Carlo as described in section 4.5 and dividing for the total pseudorapidity amplitude (2.4). The N_{ch} values of the plot points are the average calculated in the respective bin. The ratios have a decreasing trend incompatible with a constant value, even if they tend to stabilize at higher multiplicities. Consequently, the ratio between the mean value at lower multiplicities ($N_{ch} \leq 12$) and the one at higher ($N_{ch} > 30$) is $0.885 \pm 0.009 \pm 0.003$ (88.5%), smaller than unity.

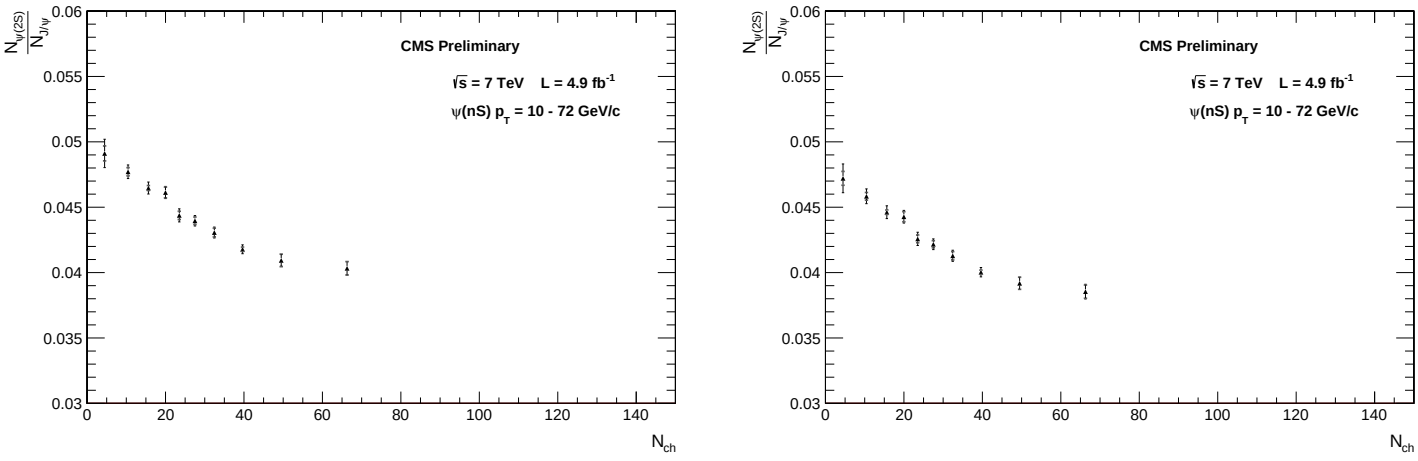

(a) (b)

Figure 5.5: Prompt ψ(2S) and J/ψ yield ratio, before (a) and after (b) the corrections.

5.1.4 Statistical and systematic uncertainties

An error of statistical nature is due to the fit uncertainties, automatically provided by the fitting algorithm, which assigns an error to every free parameter. The systematical error instead has three sources:

- the uncertainty in the determination of the efficiency and acceptance corrections;
- the choice of the invariant mass fitting function (signal + background);
- the choice of the fit function used to separate prompt and non-prompt charmonium signal.

These uncertainty sources have been evaluated separately in Tab. 5.6 and 5.7.
The first one has been extracted together with the correction themselves and has been added to the statistical uncertainty, as it also depends on the statistical distribution. The second has been evaluated as the maximum difference between the results obtained with the fit function described above, the same one with the background described by a third degree Chebyshev polynomial, and the sum of a Gaussian and a Crystal Ball distribution. For the third one, the model used for the ℓ resolution has been modified, changing from the default value of 1 to 2 its "scale factor", a parameter that indicates the scale of the individual Gaussian components.

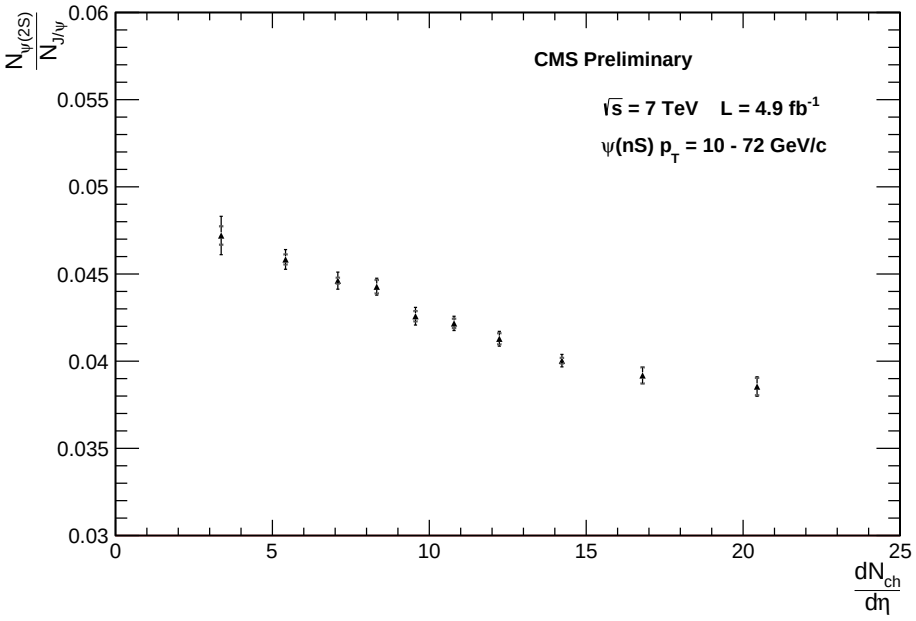

Figure 5.6: Prompt ψ(2S) and J/ψ yield ratio, as a function of reconstructed $\frac{dN_{ch}}{d\eta}$ with track $p_T > 0$.

$\mathbf{N_{ch}}$ **bin**	**Signal**	**Background**	**Non-prompt**
0-7	1.4	0.5	0.02
7-13	1.1	0.2	0.03
13-18	1.1	0.3	0.04
18-22	1.1	0.3	0.03
22-25	1.1	0.3	0.03
25-30	1.1	0.3	0.04
30-35	1.1	0.3	0.04
35-45	1.1	0.3	0.04
45-55	1.1	0.3	0.04
55-150	1.2	0.3	0.04

Table 5.6: Prompt J/ψ yield difference (%) from different extraction methods of signal, background and non-prompt part.

$\mathbf{N_{ch}}$ **bin**	**Signal**	**Background**	**Non-prompt**
0-7	1.6	0.7	0.0001
7-13	1.4	0.4	0.0079
13-18	1.3	0.1	0.0006
18-22	1.3	0.6	0.0130
22-25	1.2	0.5	0.0054
25-30	1.4	0.4	0.0015
30-35	1.4	0.5	0.0058
35-45	1.4	0.1	0.0107
45-55	1.4	0.9	0.0247
55-150	1.4	1.1	0.0037

Table 5.7: Prompt ψ(2S) yield difference (%) from different extraction methods of signal, background and prompt part.

Every analysis has been repeated with the variations described above, and have been compared to the main results. The total systematic uncertainty (see Tab. 5.8) for every bin has then been calculated as the root sum squared of these three differences. In Fig. 5.7 systematic and statistical uncertainties for the prompt ψ(2S)/J/ψ ratio are compared.

Bin	0-7	7-13	13-18	18-22	22-25	25-30	30-35	35-45	45-55	55-150
Systematic error	1.2	0.7	0.4	0.9	0.8	0.7	0.8	0.5	1.2	1.4

Table 5.8: Systematic error (%) on the prompt ψ(2S)/J/ψ ratio for each multiplicity bin.

Additionally, the size of the last bin has been modified from $N_{ch} = 55 - 150$ to $N_{ch} = 55 - 70$ to check for a possible systematic uncertainty due to the binning: it resulted to be of 1.5%.

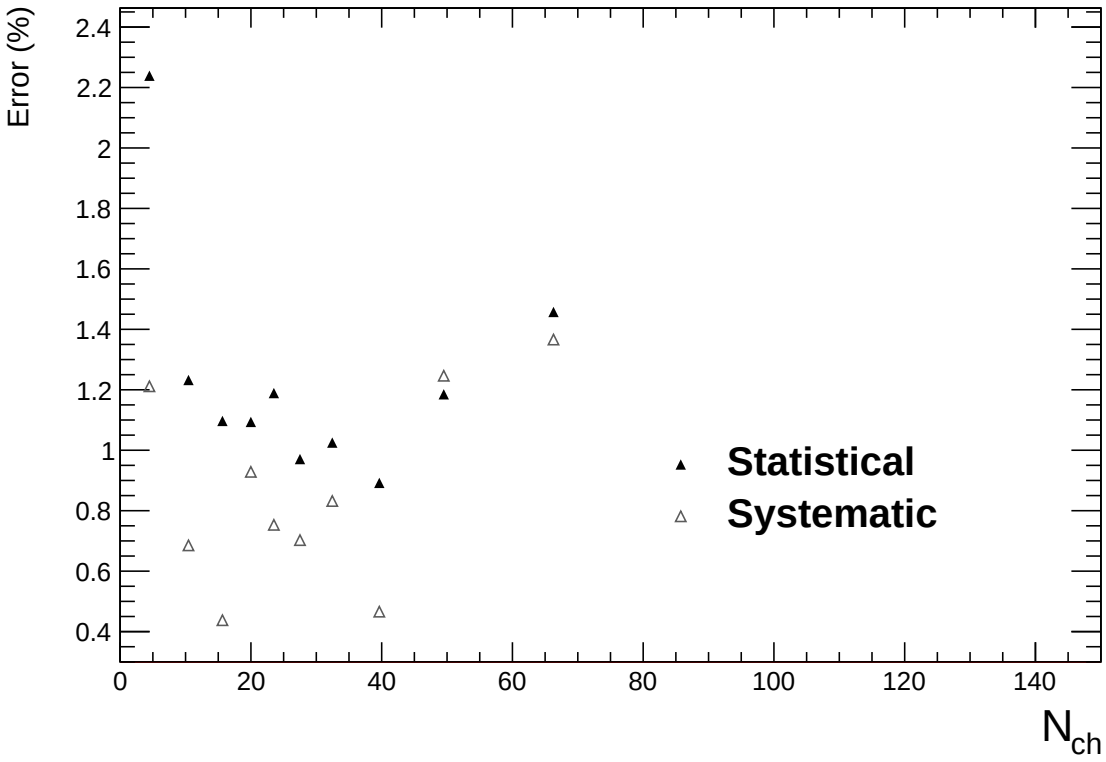

Figure 5.7: Systematic and statistical errors on the prompt $\psi(2S)/J/\psi$ ratio as a function of multiplicity.

5.1.5 Normalized results

The ψ(2S) and J/ψ proper yields have then been plotted as a function of multiplicity, normalizing the axes in the following way:

- for each bin in which there are N_i Minimum Bias events, the fraction of all Minimum Bias events contained in this particular bin is extracted: $f_i = \frac{N_i}{N}$;
- in each bin, its J/ψ or ψ(2S) production yield Y_i is extracted and divided by f_i and the whole yield Y: $\frac{Y_i}{Y f_i}$. This is done in order to take into account that in some bins the yield is higher only because there are more events, or viceversa;
- the horizontal axis is normalized with the average Minimum Bias multiplicity.

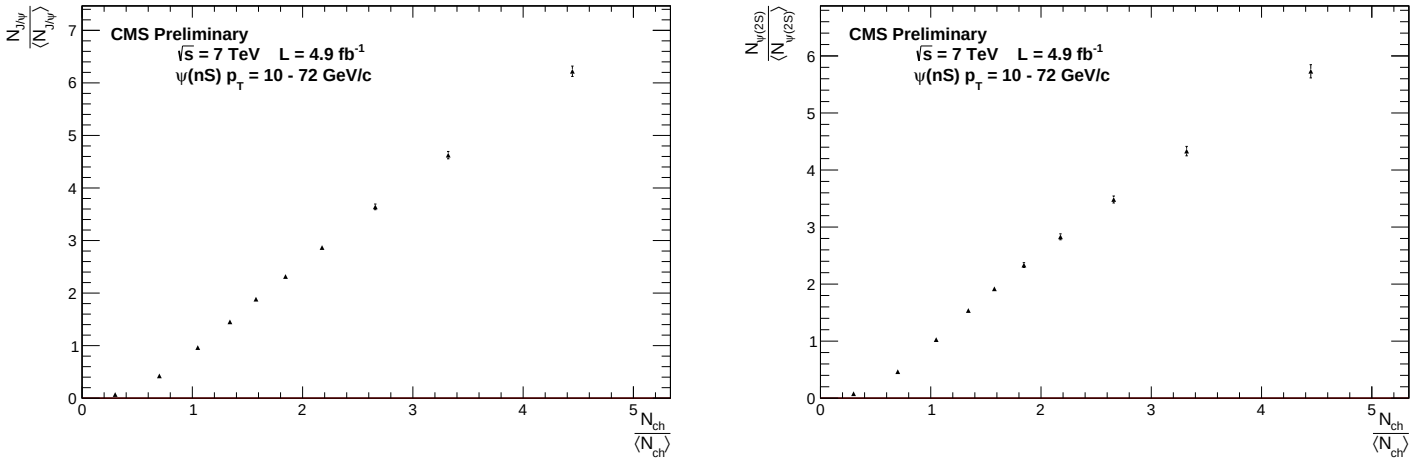

(a) (b)

Figure 5.8: Normalized prompt yields of ψ(2S) (a) and J/ψ (b) as a function of normalized multiplicity.

5.1.6 Results with finer binning

The results obtained so far show that the value of ψ(2S)/J/ψ seems to differ between lower and higher multiplicities. In order to check the compatibility of the trend with two constant values at lower and higher multiplicity and a central decrease zone, the typical signature that a transition has occurred, the ratios have been calculated with a higher number of bins, extrapolating the B fraction for $N_{ch} < 7$ from the points at higher multiplicity. For this task, the plot has been fitted in two ways: with three separated ranges and with a single sigmoid curve, defined as $S(t) = \frac{a}{1+e^{-b(t+c)}}$, where a, b and c are

the fit parameters and t corresponds to the main variable, N_{ch}. The results showed a certain degree of compatibility, but the errors are too high to draw definitive conclusions (see Fig. 5.9).

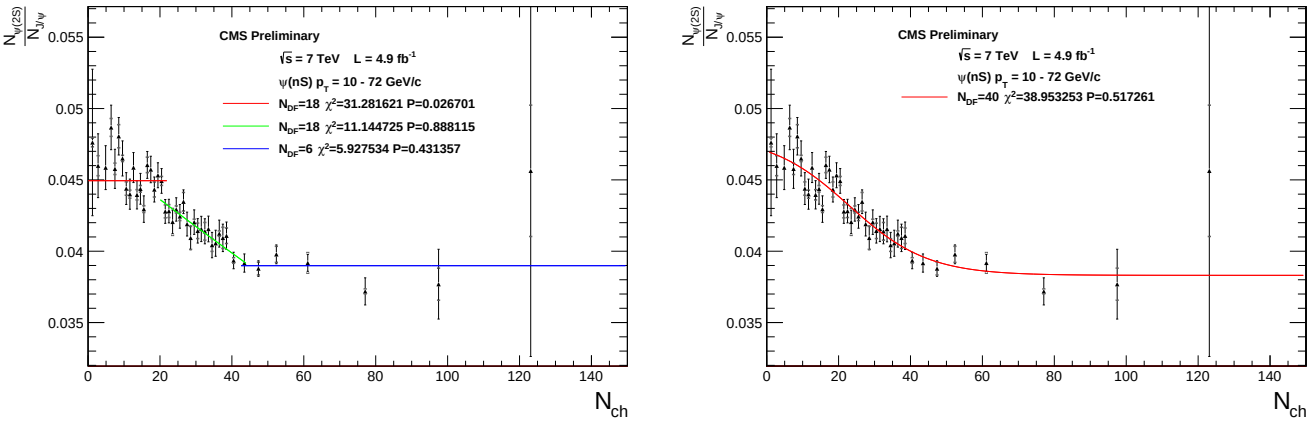

(a) (b)

Figure 5.9: Prompt $\psi(2S)/J/\psi$ ratios fitted with two constant functions and a second grade polynomial (a) and a sigmoid curve (b), with respective χ^2 probabilities.

5.2 Inclusive non-prompt studies

The same plots have been made also for the non-prompt part of the data (see Fig. 5.10, 5.6 and 5.12, and Tab. 5.9), to look for different behaviors characteristic of one of the two sources. However, no great differences have been noticed. The values of $\psi(2S)/J/\psi$ ratios are higher on average, but their trend, reflected by the high/low N_{ch} ratio, is in fact quite unchanged.

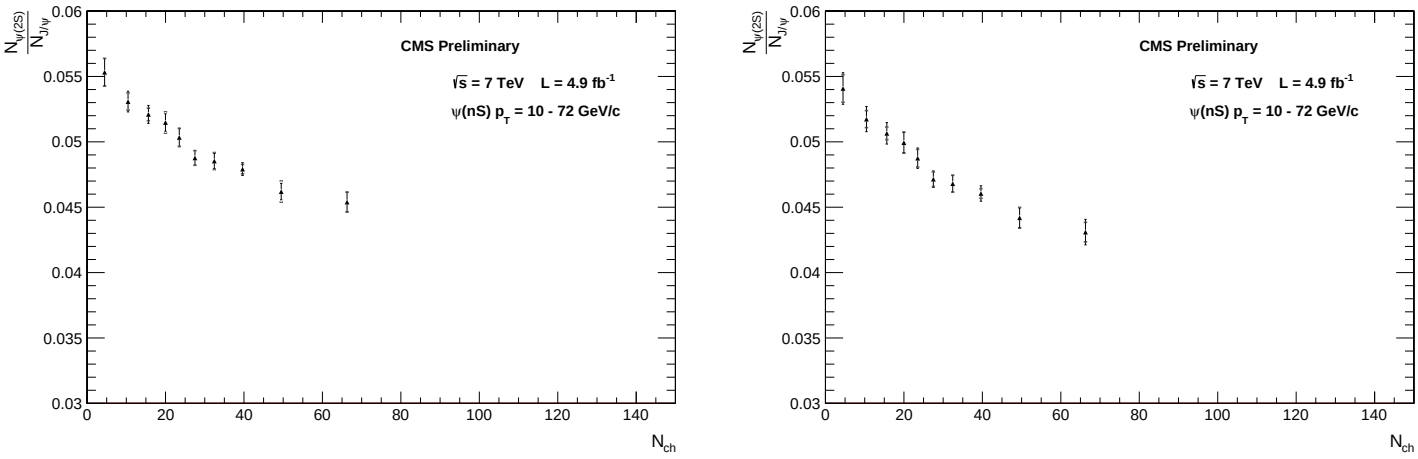

(a) (b)

Figure 5.10: Non-prompt ψ(2S) and J/ψ yield ratio, before (a) and after (b) the corrections.

N_{ch} bin	**Non-prompt** ψ(2S)/J/ψ
0-7	0.0541±0.0012±0.0011
7-13	0.0517±0.0010±0.0007
13-18	0.0507±0.0008±0.0005
18-22	0.0499±0.0008±0.0008
22-25	0.0488±0.0008±0.0007
25-30	0.0471±0.0006±0.0006
30-35	0.0468±0.0006±0.0007
35-45	0.0460±0.0006±0.0004
45-55	0.0442±0.0007±0.0008
55-150	0.0431±0.0010±0.0007
High/Low ratio	0.8801±0.0121±0.0014

Table 5.9: Acceptance correction on non-prompt ψ(2S)/J/ψ ratios, already corrected with the efficiency.

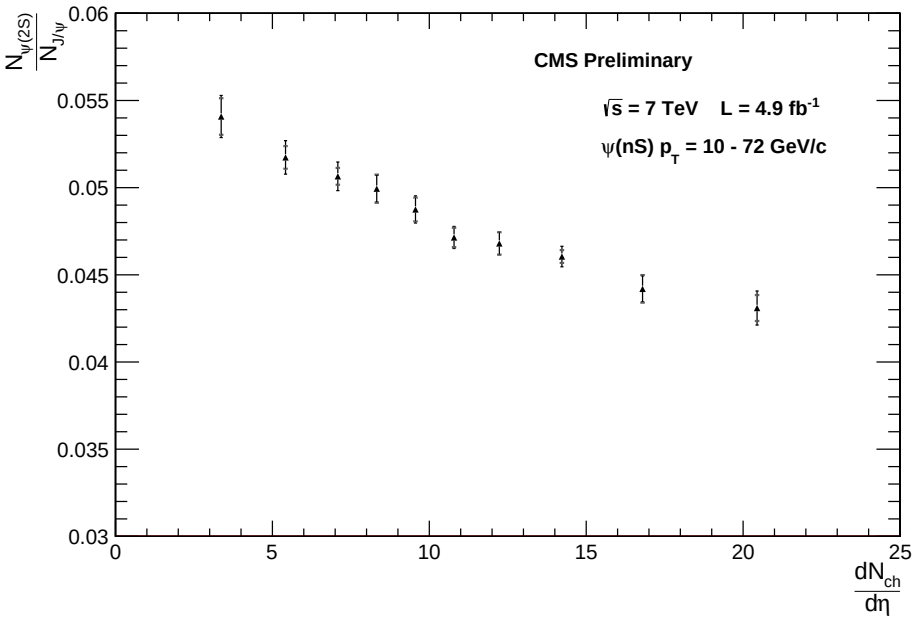

Figure 5.11: Non-prompt ψ(2S) and J/ψ yield ratio, as a function of reconstructed $\frac{dN_{ch}}{d\eta}$ with track $p_T > 0$.

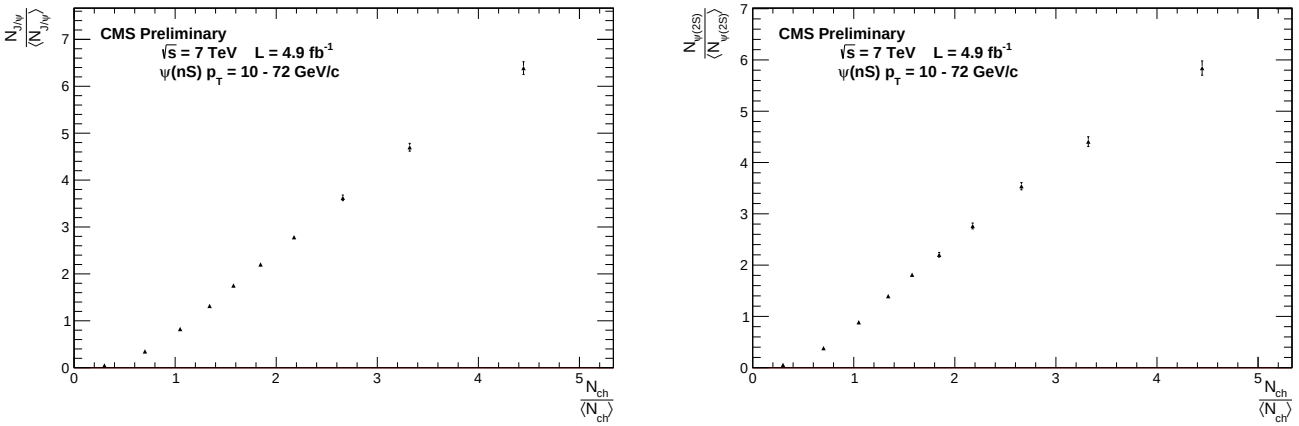

(a) (b)

Figure 5.12: Normalized non-prompt yields of ψ(2S) (a) and J/ψ (b) as a function of normalized multiplicity.

5.3 Mean p_T vs multiplicity

The mean p_T calculated in bins of multiplicity (listed in Table 4.1) for $p_T > 10$ GeV/c is shown in Fig. 5.14. It has been extracted with the sideband subtraction method, described in Section 3.4, then efficiency and acceptance corrections have been applied to the p_T spectrum of every bin (see for example Fig. 5.13) before calculating the mean value. Prompt trends are almost linearly increasing and do not show much difference between each other. However, this may be because J/ψ and ψ(2S) masses do not differ enough to notice significantly the mass ordering of $\langle p_T \rangle$ predicted in case of expansion of a hot medium (see section 1.3.2). The non-prompt ψ(2S) $\langle p_T \rangle$ instead grows faster than non-prompt J/ψ and both have a little discrepancy in the first N_{ch} bin.
The higher $\langle p_T \rangle$ for non-prompt charmonia is expected, as the B fraction reportedly increases with p_T [35].

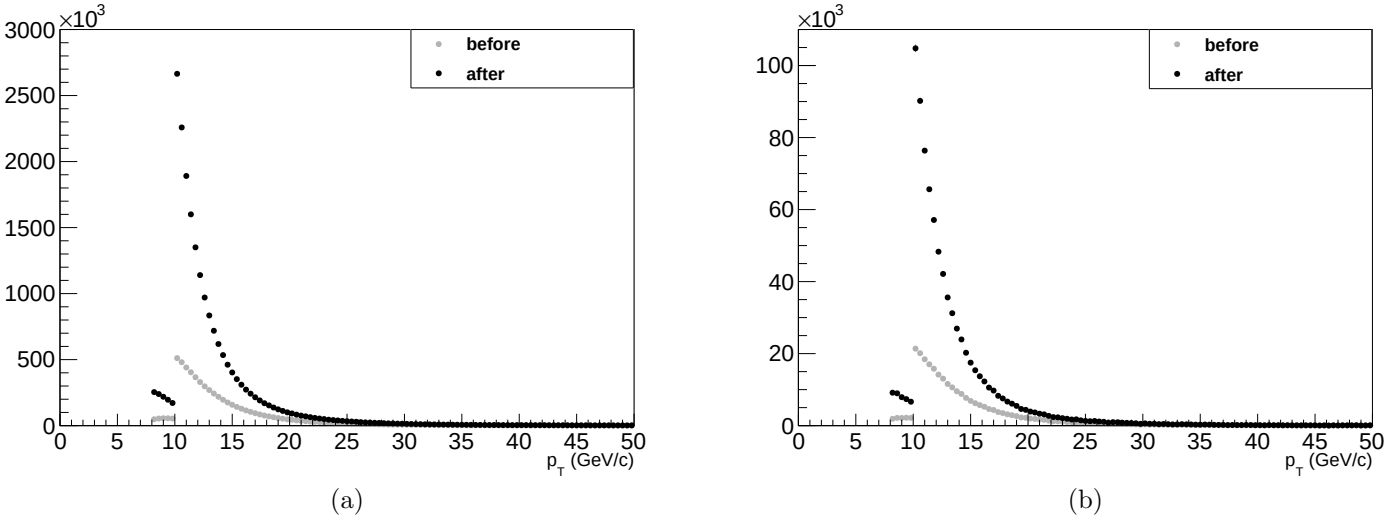

(a) (b)

Figure 5.13: p_T spectra for prompt J/ψ (a) and ψ(2S) (b) in the range $8 < p_T \leq 72$ GeV/c and $7 < N_{ch} \leq 150$, before and after efficiency and acceptance corrections.

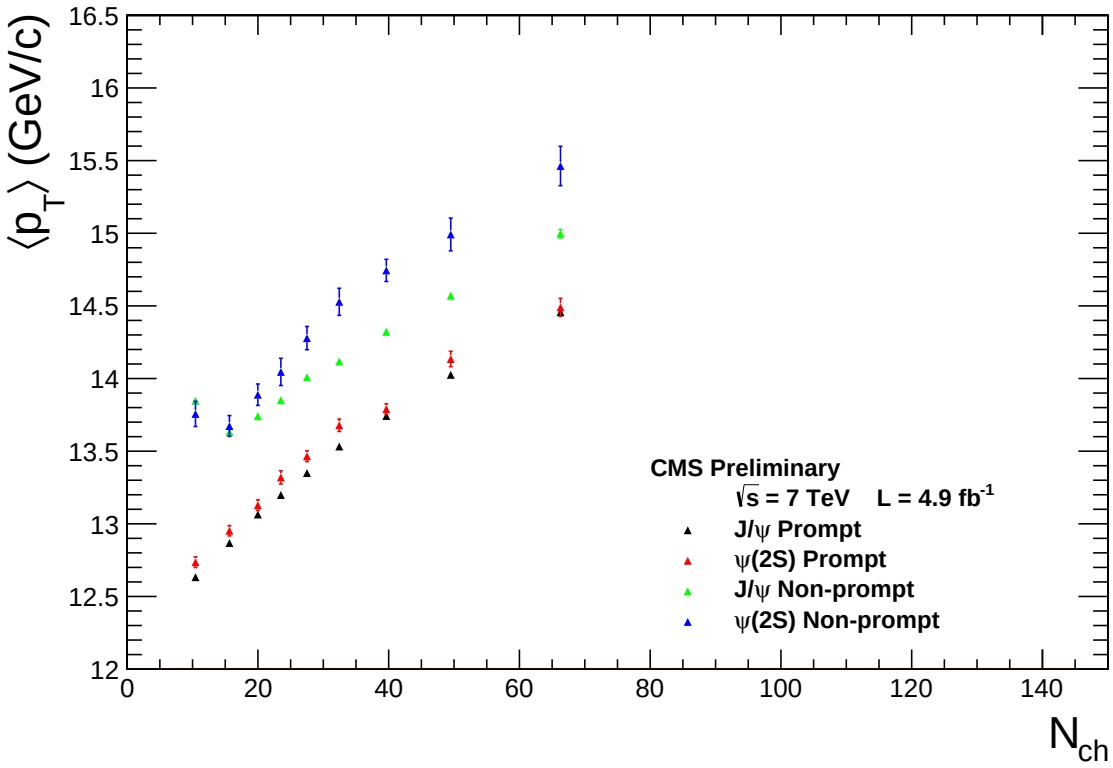

Figure 5.14: Mean p_T in bins of multiplicity for ψ(2S) and J/ψ.

5.4 Results in ranges of p_T

To investigate more in detail the former results, the same plots have been obtained in bins of p_T (see Fig. 5.15 and 5.16), this time including also the range $8 < p_T \leq 10$ GeV/c, but with a lower integrated luminosity ($L_{int} \simeq 200$ pb^{-1}). Guide lines have been added to the normalized yield plots.

The ratio of the two yields evidently increases with p_T. It also appears that the J/ψ and

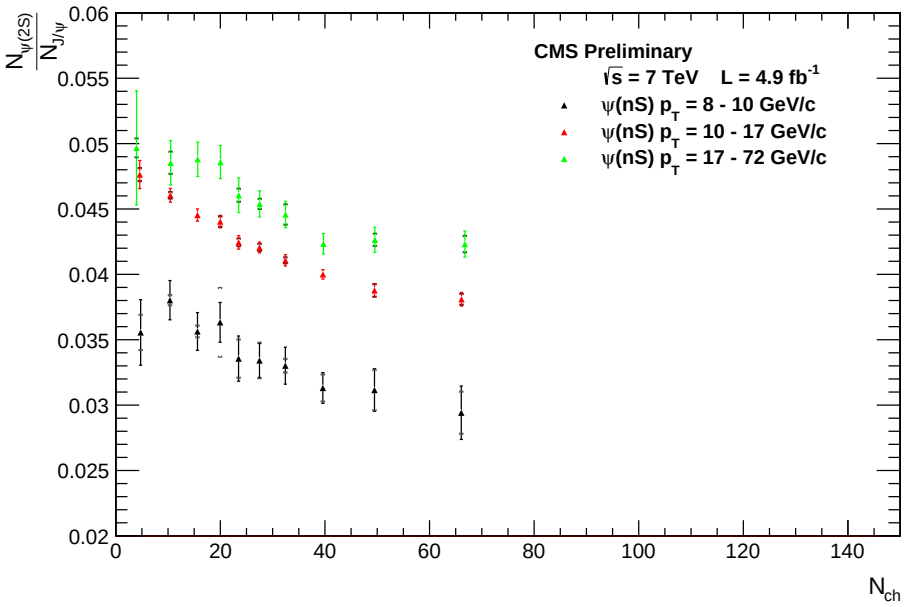

Figure 5.15: ψ(2S) and J/ψ prompt yield ratio, in different p_T ranges.

ψ(2S) yield grow similarly at low multiplicities, while the yield of the second one begins to increase more slowly for $\frac{N_{ch}}{\langle N_{ch} \rangle} > 2$, as highlited in Fig. 5.17. The double ratio between the prompt ψ(2S)/J/ψ ratios at higher (> 30) and lower (≤ 12) multiplicities has been calculated as a function of p_T (see Fig 5.18), and the numerical values are shown in Tab. 5.10. These values are approximately constant with p_T.

$\mathbf{p_T}$ **bin**	$\langle \mathbf{p_T} \rangle$	**Prompt ratio**	**Non-prompt ratio**
8-10	9.0	0.86±0.03±0.02	0.81±0.04±0.07
10-17	12.7	0.871±0.008±0.002	0.8835±0.0102±0.0013
17-72	23.7	0.8767±0.0220±0.0012	0.9072±0.0188±0.0007

Table 5.10: Double ratios between the last and the first bins of multiplicity.

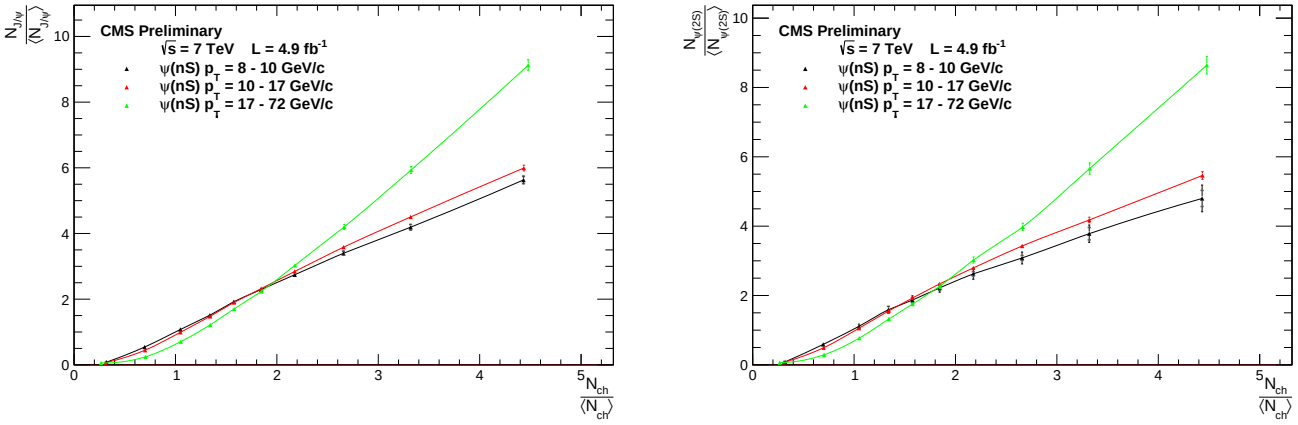

(a) (b)

Figure 5.16: Normalized yields of prompt J/ψ (a) and ψ(2S) (b) as a function of normalized multiplicity, in different p_T ranges.

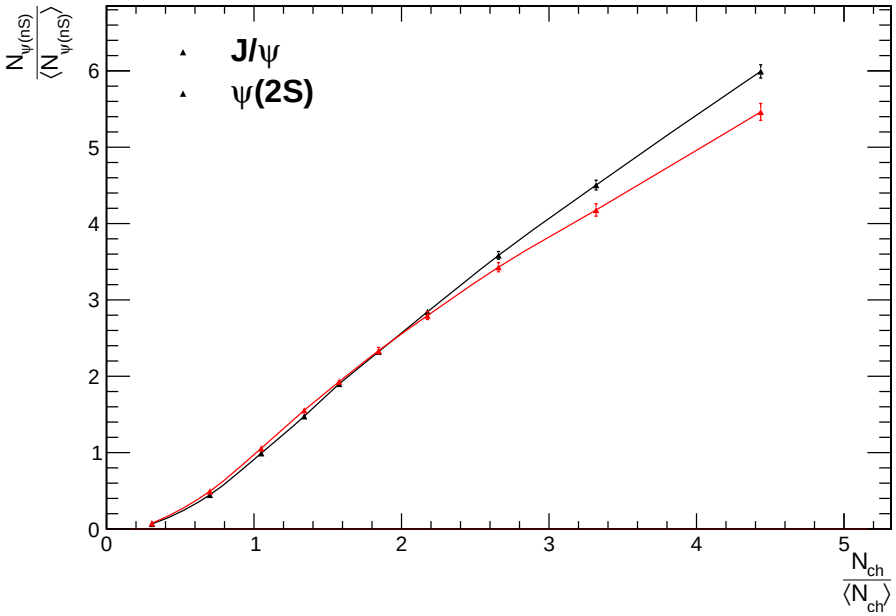

Figure 5.17: Comparison between ψ(2S) and J/ψ yields. The interval $10 < p_T \leq 17$ GeV/c is considered as an example.

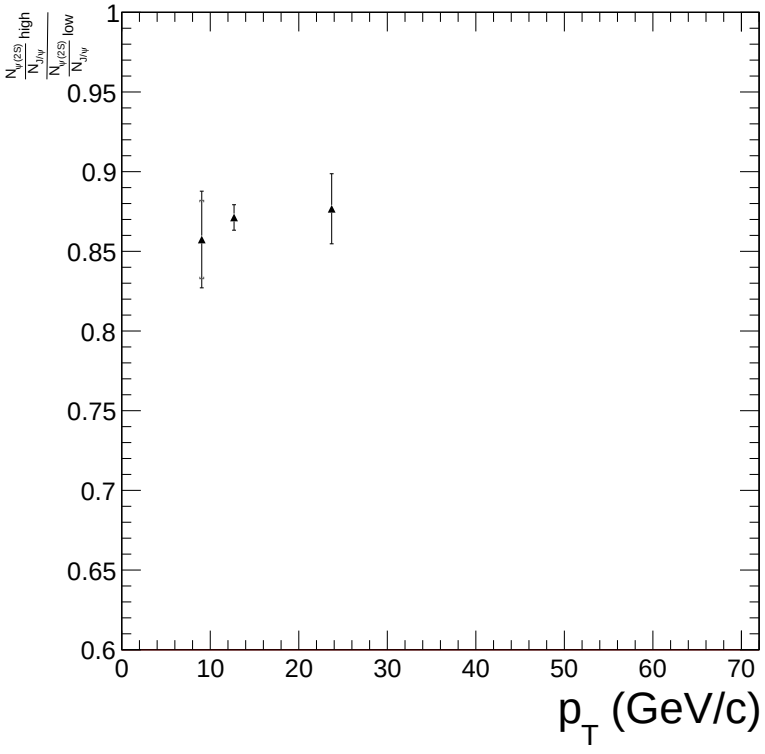

Figure 5.18: Double ψ(2S)/J/ψ prompt ratios as a function of p_T.

5.5 Feed-down and comover studies

A possible issue in the calculation of these ratios is the presence of charmonia producted by the decay of higher mass states (feed-down contribution), because they are usually accompanied by a couple of pions, whose products can bias the evaluation of the charged particle multiplicity towards higher values. As these products must follow the charmonia at a close angle, the prompt $\psi(2S)/J/\psi$ ratios and high/low N_{ch} ratios have been compared (see Fig. 5.19 and Tab. 5.11) for a different number of tracks in the cone around the direction of the charmonium ($\Delta R = \sqrt{\Delta\phi^2 + \Delta\eta^2} < 0.5$).

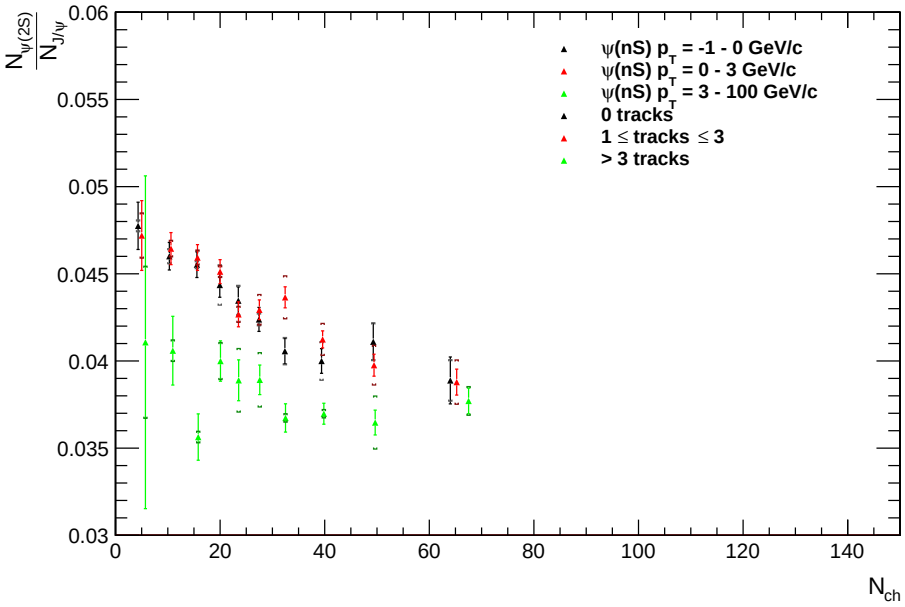

Figure 5.19: Prompt $\psi(2S)/J/\psi$ ratios for 0, 1 to 3 and more than 3 tracks in the cone.

Tracks	Prompt ratio
0	0.882±0.015±0.005
1-3	0.895±0.013±0.012
> 3	0.99±0.03±0.03

Table 5.11: Double ratios between the last and the first bins of multiplicity, as a function of the number of tracks in the cone.

The presence of the same decrease seen before even for 0 tracks seems to exclude that this phenomenon is due to the interaction of the charmonia with comovers, and the lower

ratios for more than 3 tracks in the cone is the opposite of what one could expect from a significant feed down contribution, which would make the last bins more similar to the first ones. Inspecting multiplicity in these three cases, the discrepancy could instead be caused by a more homogeneous multiplicity distribution, less peaked at a low value.

Chapter 6

Results comparison

6.1 Normalized yields

The statistics available for this study has allowed for the first time to directly analyze the variation with p_T of the J/ψ and ψ(2S) normalized yields dependence from charged particle multiplicity. It can be noticed that it departs more significantly from linearity for increasing p_T. Even though it has not been possible to make this same comparison in other analyses, a similar departure from linearity, starting from $\frac{dN_{ch}}{d\eta} \simeq 15 - 20$ likewise, has already been observed [42]. Anyway, the results of chapter 5 are also fully compatible with previous studies in different ranges of p_T (see Fig. 6.1).

This result possibly consistent with the predictions of the percolative model for string interactions introduced in section 1.3.2, as the screening effect is dependent on the observable hardness. Alternatively, this has also shown agreement with calculations made with EPOS 3 + Hydro, assuming the energy density high enough to apply hydrodynamic evolution to the core of the collisions. On the contrary, PYTHIA 8 has generally underestimated similar measurements [42, 44].

6.2 Charmonium ratios

The lower increase rate with multiplicity of the ψ(2S) yield compared to the one of J/ψ could be reflected by the decrease of the ψ(2S)/J/ψ ratio at higher multiplicities. This behaviour has already been observed in p-p collisions for Υ production [34] (Fig. 6.2), comparing the base Υ(1S) state to the excited states Υ(2S) and Υ(3S), and also in p-Pb collisions at ATLAS. [51], even though using a different observable to parametrize centrality (Fig. 6.3). This phenomenon has often been explained in Pb-Pb and p-Pb collisions as an effect of the creation of QGP.

A suppression of the J/ψ with increasing multiplicity had already been predicted [45] as a consequence of dissociation and melting in a hot medium, even if at very high $\frac{dN_{ch}}{d\eta}$.

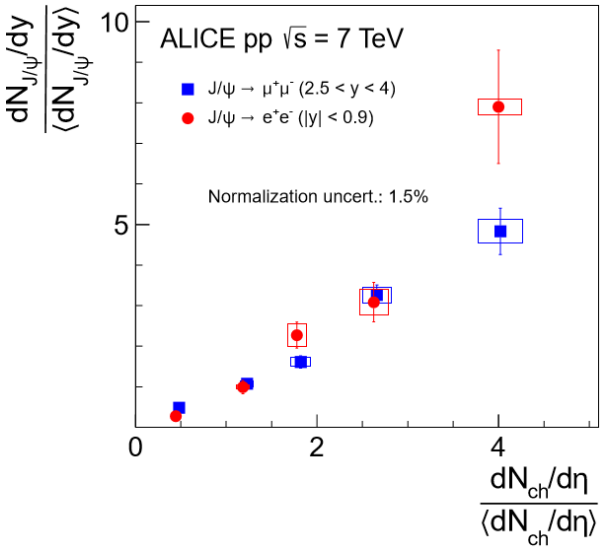

Figure 6.1: A measurement of J/ψ normalized production by the ALICE collaboration, performed with lower average p_T [43].

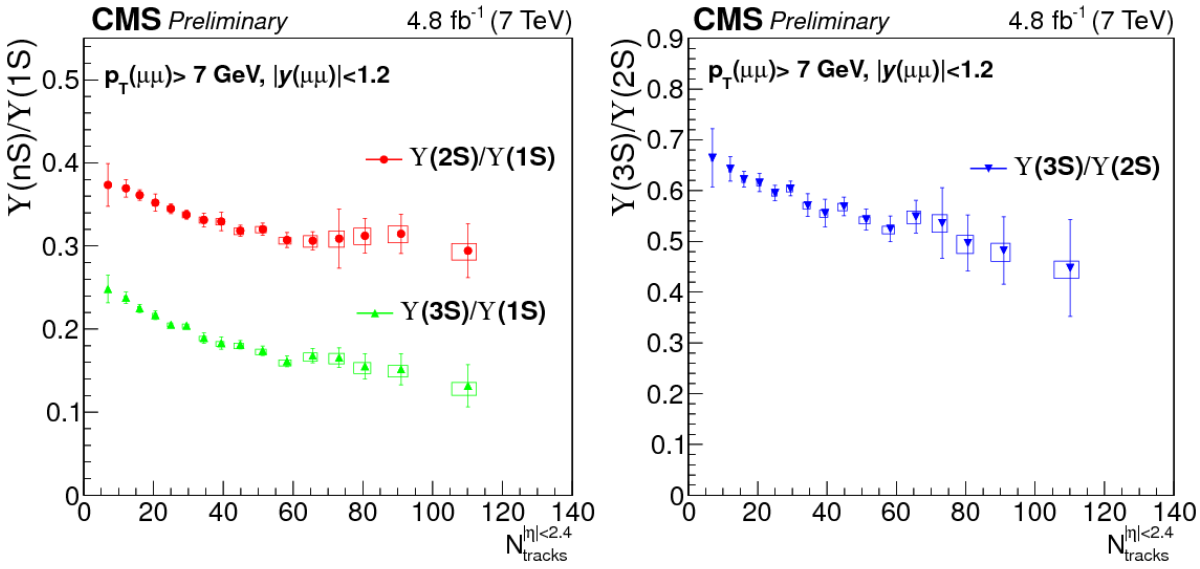

Figure 6.2: Ratios between the Υ(nS) states, measured by CMS [34].

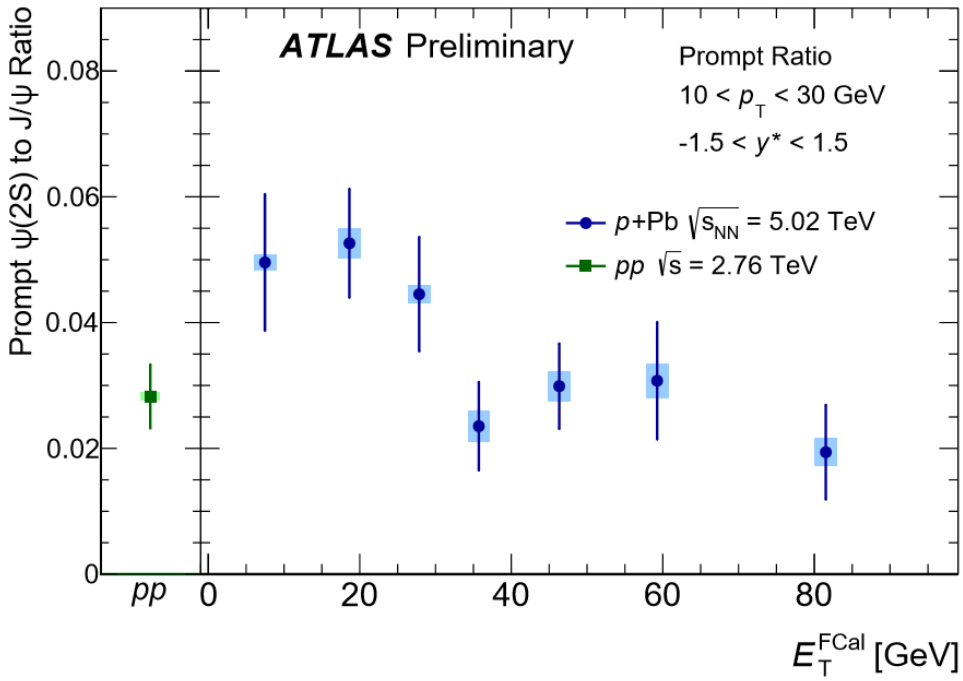

Figure 6.3: Prompt ψ(2S)/J/ψ ratio as a function of the total transverse energy measured in the ATLAS Forward Calorimeter in the direction of the lead beam.

However, with the same arguments a ψ(2S) earlier suppression can be expected, and thus be compatible with the observed ratios.
This suppression in p-A collisions has also been explained using the interaction with comovers [20], but at the particle density produced in p-p this effect is not expected to be significant [46]. In fact, as previously seen in section 5.5, even the ratios with no tracks in the cone around the quarkonium show a decrease similar to the others.
The ψ(2S)/J/ψ ratio trend can also be viewed in analogy with the strangeness enhancement, another multiplicity-dependent observable previously described, recently highlighted at ALICE [53] (Fig. 6.4).

The p_T trend of the double ratio is similar, though less distant from unity, to the one observed in previous analyses [52] at CMS but between Pb-Pb and p-p ratios (Fig. 5.18). This is possibly due to the higher energy density reached at higher multiplicities that may trigger suppression effects.

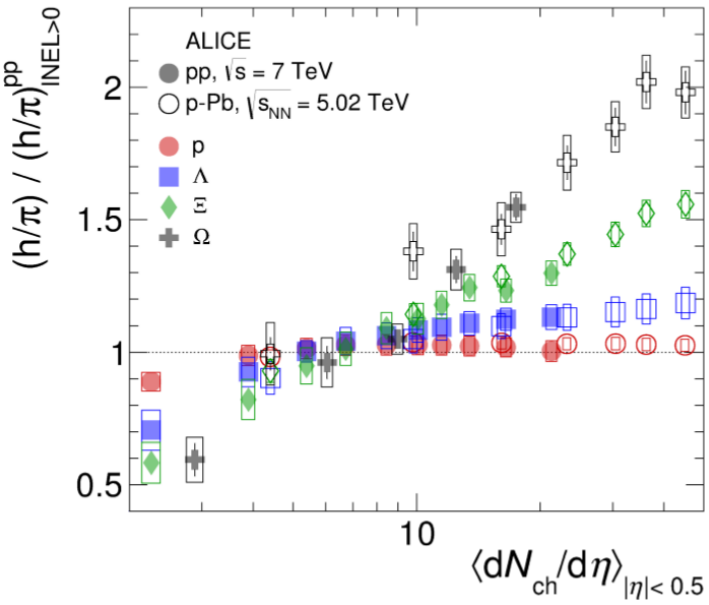

Figure 6.4: Strange baryon and proton to pion ratios in pp and p-Pb as a function of charged particle multiplicity density normalized to inclusive baryon to pion ratios for pp and p-Pb collisions, measured by ALICE [53].

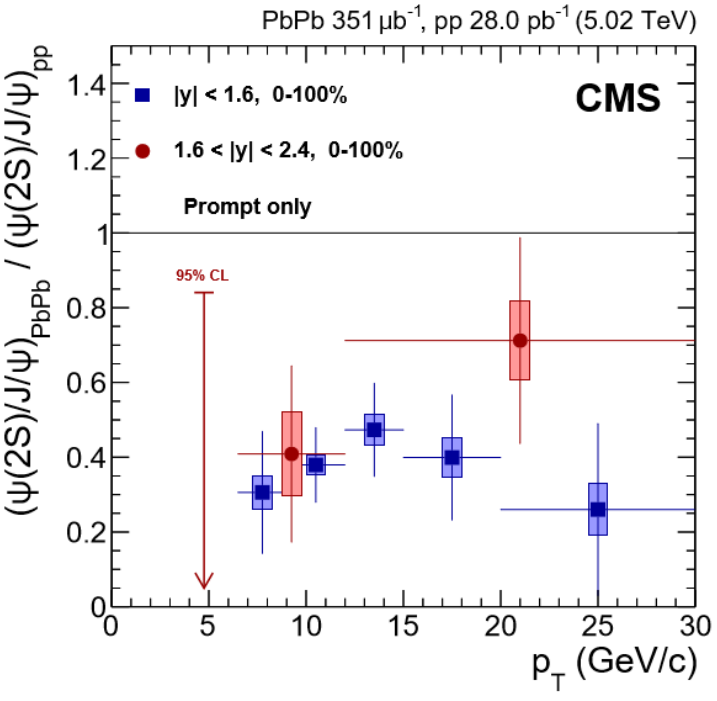

Figure 6.5: A previous result at CMS for heavy-ion collisions [52].

6.2.1 Non-prompt suppression

A very similar suppression has been observed also in non-prompt $\psi(2S)/J/\psi$ ratios. As for the non-prompt charmonium, the suppression of J/ψ has already been noticed in recent heavy-ion studies [41], but the reason behind the decrease of the $\psi(2S)/J/\psi$ yield ratio is unclear: this behavior should be better investigated in future.

6.3 Interpretations

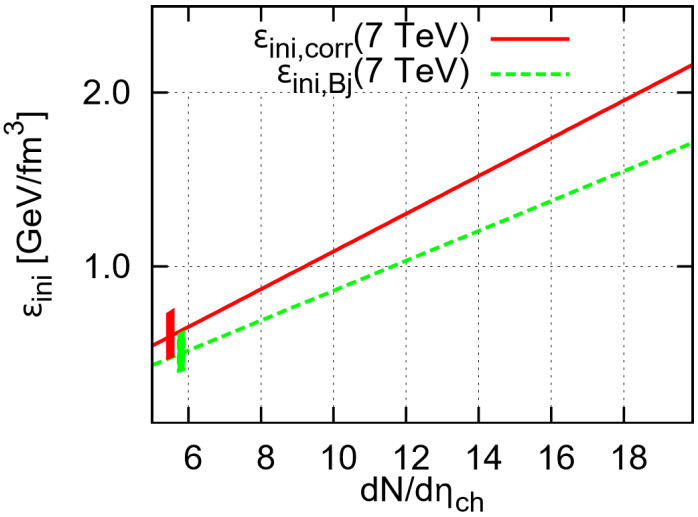

Figure 6.6: Initial energy density according to the Bjorken model, with and without corrections for acceleration effects [47].

Calculations [47] based on the Bjorken model (see Fig. 6.6), show that the energy density reached by the system exceeds 1 GeV/fm^3 already at low multiplicities ($\frac{dN_{ch}}{d\eta} \sim 10$). These value are compatible with a multiplicity of 20 for charged track $p_T > 0.4$ GeV/c, according to the results of section 4.5, therefore this matches with the beginning of slope variation in the prompt $\psi(2S)/J/\psi$ ratios of Fig. 5.9. Moreover, it is in this same multiplicity zone that the strangeness enhancement of Fig. 6.4 and the $\frac{\Upsilon(nS)}{\Upsilon(mS)}$ decrease of Fig. 6.2 begin to show. Inspecting the average p_T of charged tracks (Fig. 6.7), a slope change can be noticed around $N_{ch} = 20$. This could be a hint to a gradual kind of phase transition (possibly a cross-over as foreseen in [48]), provided that also the v_2 Fourier coefficients associated to azimuthal anisotropies ([54], Fig. 6,7) start to appear next to this multiplicity value.
In fact, a similarity in the dependence from multiplicity of the Fourier coefficients of the two-particle correlation function, namely an increase of azimuthal anisotropy with N_{ch},

has recently been observed between p-Pb and p-p collisions [54]. This could match with the collective phenomena explained in section 1.3.2.
The behaviors observed above can also be explained by other models, but none is fully compatible with all af these. For example, PYTHIA can reproduce the p_T slope change with the addition of multiparton interactions, and the still positive slope after that point with color reconnection, but does not predict the increase of strange baryons with respect to pions as a function of multiplicity [49]. This is instead predicted by the color rope model [50], which conversely can not describe well the p_T spectra of the various particles and above all the K/π and p/π ratios as a function of p_T.

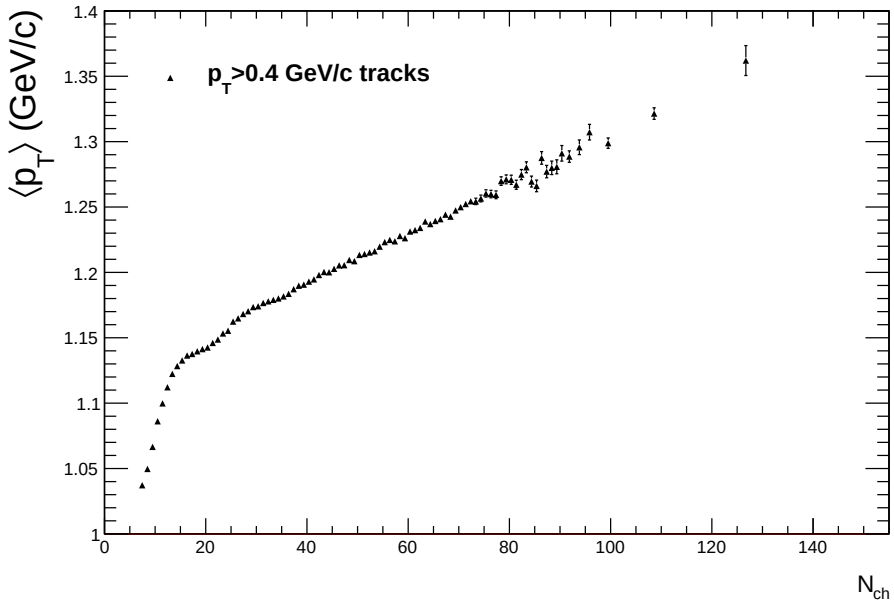

Figure 6.7: Average p_T of the charged tracks used for the computation of multiplicity ($p_T > 0.4$ GeV/c), in multiplicity bins from 7 to 150.

Conclusions

The J/ψ and ψ(2S) production yields and ratios have been studied as a function of multiplicity.
The normalized yields showed a more significant departure from linearity for increasing p_T. This could be consistent with the predictions of the string interaction percolative model [21], as the screening effect is dependent on the hardness. Alternatively, this has been seen to be approximately reproduced by applying hydrodynamic evolution to the produced medium.
The ratio between ψ(2S) and J/ψ resulted to be the most interesting observable. The decrease can be seen in the framework of several other multiplicity-dependent observables such as Υ(nS)/Υ(mS) ratios decrease, strangeness enhancement, a slope modification in the average p_T of the charged tracks and the appearance of azimuthal correlations at low multiplicities. Most of these signatures are often referred to as possible effects of collectivity in heavy-ion studies.
Among these, the decrease of ψ(2S)/J/ψ and Υ(nS)/Υ(mS) ratios as a function of multiplicity could be a peculiar clue of the creation of a hot, dense and color-conductor medium even in p-p collisions. However, further theoretical and experimental studies are needed, also to rule out possible contributions from other phenomena.

Bibliography

[1] S. Braibant, G. Giacomelli, M. Spurio, *Particelle e interazioni fondamentali*, Springer, June 2010

[2] A. Pich, *Quantum Chromodynamics*, arXiv:hep-ph/9505231v1 (1995)

[3] LHCb Collaboration, *Observation of* $J/\psi p$ *resonances consistent with pentaquark states in* $\Lambda_b^0 \to J/\psi K^- p$ *decays*, Phys. Rev. Lett. 115, 072001 (2015)

[4] DØ Collaboration, *Evidence for a* $B_s^0\pi^\pm$ *State*, Phys. Rev. Lett. 117, 022003 (2016)

[5] A. S. Kronfeld, *Quantum chromodynamics with advanced computing*, Journal of Physics: Conference Series 125 (2008)

[6] M. Troyer, U. Wiese, *Computational complexity and fundamental limitations to fermionic quantum Monte Carlo simulations*, Phys. Rev. Lett. 94, 170201 (2004)

[7] J. Dias de Deus, *The search for the Quark-Gluon Plasma*, CERN-2001-003 (2001)

[8] T. Lappi, *Theory overview of Heavy-ion collisions*, PoS LHCP2016 016 (2016)

[9] D. Kharzeev, *Quarkonium Production In Nuclear Collisions*, `http://lpsc.in2p3.fr/hadrons/ct97/Dkha/Dkha.html`

[10] F. Karsch, E. Laermann, *Thermodynamics and in-medium hadron properties from lattice QCD*, arXiv:hep-lat/0305025 (2003)

[11] J. D. Bjorken, *Highly relativistic nucleus-nucleus collisions: The central rapidity region*, Phys. Rev. D, vol. 27, no. 1, pp. 140–151, 1983

[12] L. Massacrier, *Heavy-flavour and quarkonium production in the LHC era: from proton-proton to heavy-ion collisions*, Eur. Phys. J. C 76:107 (2016)

[13] O. Linnyk, E. L. Bratkovskaya, W. Cassing, *Charmed hadron signals of partonic medium*, Journal of Physics G: Nuclear and Particle Physics, Volume 36, Number 6 (2008)

[14] P. Foka, M. A. Janik, *An overview of experimental results from ultra-relativistic heavy-ion collisions at the CERN LHC: bulk properties and dynamical evolution*, Reviews in Physics 1 (2016) 154-171

[15] M. Nardi, M. Lombardo, *Quark-gluon Plasma and Heavy ion Collisions*, World Scientific, 2002

[16] J. P. Lansberg, J/ψ *production at* $\sqrt{s}$ = 1.96 *and 7 TeV: Color-Singlet Model, NNLO* and polarisation*, J. Phys., vol. G38, p. 124110, 2011

[17] CMS Collaboration, *Measurement of momentum flow relative to the dijet system in PbPb and pp collisions at* $\sqrt{s_{NN}} = 2.76$ *TeV*, CERN-PH-EP-2015-260 (2014)

[18] K. Dusling, W. Li, B. Schenke, *Novel Collective Phenomena in High-Energy Proton-Proton and Proton-Nucleus Collisions*, Int. J. Mod. Phys. E25 (2016) 01, 1630002

[19] N. Brambilla, S. Eidelman, B. K. Heltsley, R. Vogt, *Heavy quarkonium: progress, puzzles, and opportunities*, Eur. Phys. J. C 71:1534 (2011)

[20] E. G. Ferreiro and C. Pajares, *High multiplicity pp events and* J/ψ *production at LHC*, Phys. Rev. C 86, 034903 (2012)

[21] E. G. Ferreiro and C. Pajares, *Open charm production in high multiplicity proton-proton events at the LHC*, arXiv:1501.03381v1 (2015)

[22] Y. Ko, *Derivation of a Quark Confinement Potential from QCD*, arXiv:nucl-th/9901025v3 (1999)

[23] The Large Hadron Collider:
`http://home.web.cern.ch/topics/large-hadron-collider`

[24] CMS Collaboration, *The CMS experiment at the CERN LHC*, JINST 3 (2008) S08004

[25] R. Frühwirth, *Application of Kalman filtering to track and vertex fitting*, Nucl. Instrum. Meth. A 262 (1987) 444

[26] K. Rose, *Deterministic Annealing for Clustering, Compression, Classification, Regression and related Optimisation Problems*, Proceedings of the IEEE 86 (1998)

[27] P. Adzic et al., *Energy resolution of the barrel of the CMS electromagnetic calorimeter*, JINST 2 (2007) P04004

[28] CMS Collaboration, *Description and performance of track and primary-vertex reconstruction with the CMS tracker*, JINST 9 (2014) P10009

[29] CMS Collaboration, *Energy resolution of the barrel of the CMS Electromagnetic Calorimeter*, JINST 2 (2007) P04004

[30] ZDC Wiki: `https://twiki.cern.ch/twiki/bin/viewauth/CMS/ZDCWikiHome`

[31] CMS Collaboration, *The performance of the CMS muon detector in proton–proton collisions at* $\sqrt{s} = 7$ *TeV at the LHC*, JINST 8 (2013) P11002

[32] CMS Collaboration, *Performance of CMS muon reconstruction in pp collision events at* $\sqrt{s} = 7$ *TeV*, JINST 7 (2012) P10002

[33] R. Schmidt, R. Assmann, E. Carlier, et al. *Protection of the CERN large hadron collider*, New Journal of Physics, 8, 2006

[34] CMS Collaboration, *Dependence of the* Υ(nS) *production ratios on charged particle multiplicity in pp collisions at* $\sqrt{s} = 7$ *TeV*, CMS-PAS-BPH-14-009 (2015)

[35] CMS Collaboration, *Measurement of the* J/ψ *and* ψ(2S) *cross section in pp collisions at* $\sqrt{s} = 7$ *TeV*,
`https://twiki.cern.ch/twiki/bin/view/CMSPublic/PhysicsResultsBPH10014`

[36] CMS Collaboration, *Measurement of Tracking Efficiency*, CMS PAS TRK-10-002 (2010)

[37] CDF Collaboration, *Measurement of the* J/ψ *Meson and b-Hadron Production Cross Sections in* $p\bar{p}$ *Collisions at* $\sqrt{s} = 1960$ *GeV*, Phys. Rev. D 71, 032001 (2004)

[38] CMS Collaboration, *Measurement of the prompt* J/ψ *and* ψ(2S) *polarizations in pp collisions at* $\sqrt{s} = 7$ *TeV*, Phys. Lett. B 727 (2013) 381

[39] CMS Collaboration, *Measurement of prompt* J/ψ *and* ψ(2S) *double-differential cross sections in pp collisions at* $\sqrt{s} = 7$ *TeV*, Phys. Rev. Lett. 114, 191802 (2015)

[40] S. Gupta, *A short introduction to heavy-ion physics*, TIFR/TH/15-24 (2015)

[41] CMS Collaboration, *Suppression of non-prompt* J/ψ*, prompt* J/ψ*, and* Υ(1S) *in PbPb collisions at* $\sqrt{s_{NN}} = 2.76$ *TeV*, JHEP 05 (2012) 063

[42] ALICE Collaboration, *Measurement of charm and beauty production at central rapidity versus charged-particle multiplicity in proton–proton collisions at* $\sqrt{s} = 7$ *TeV*, JHEP 09 (2015) 148

[43] ALICE Collaboration, J/ψ *Production as a Function of Charged Particle Multiplicity in pp Collisions at* $\sqrt{s} = 7$ *TeV*, Phys. Lett. B 712 (2012) 165

[44] Z. Ye, *Dependence of* J/ψ *Production on Charged-Particle Multiplicity in p+p Collisions at* $\sqrt{s} = 200$ *GeV with the STAR Experiment*, 8th International Workshop on Multiple Parton Interactions at the LHC, 2016

[45] T. Lang, M. Bleicher, *Possibility for* J/ψ *suppression in high multiplicity proton-proton collisions at* $\sqrt{s_{NN}} = 7$ *TeV*, Phys. Rev. C 87, 024907 (2013)

[46] E. G. Ferreiro, private communication

[47] M. Csanád, T. Csörgő, Z. Jiang, C. Yang, *Initial energy density of* $\sqrt{s} = 7$ *and 8 TeV p+p collisions at the LHC*, arXiv:1609.07176v2 (2017)

[48] R. Campanini, G. Ferri, *Experimental equation of state in pp and* $p\bar{p}$ *collisions and phase transition to quark gluon plasma*, Phys. Lett. B 703 (2011) 237

[49] N. Fischer, T. Sjöstrand, *Thermodynamical String Fragmentation*, LU TP 16-57 (2016)

[50] C. Bierlich, G. Gustafson, L. Lönnblad, *A shoving model for collectivity in hadronic collisions*, LU-TP 16-64 (2016)

[51] ATLAS Collaboration, *Study of* J/ψ *and* ψ(2S) *production in* $\sqrt{s_{NN}} = 5.02$ *TeV p+Pb and* $\sqrt{s} = 2.76$ *TeV pp collisions with the ATLAS detector*, ATLAS-CONF-2015-023, 2015

[52] CMS Collaboration, *Relative modification of prompt* ψ(2S) *and* J/ψ *yields from pp to PbPb collisions at* $\sqrt{s_{NN}} = 5.02$ *TeV*, CERN-EP-2016-258 (2016)

[53] ALICE Collaboration, *New results related to QGP-like effects in small systems with ALICE*, PoS LHCP2016 117 (2016)

[54] ATLAS Collaboration, *Measurements of long-range azimuthal anisotropies and associated Fourier coefficients for pp collisions at* $\sqrt{s} = 5.02$ *and 13 TeV and p+Pb collisions at* $\sqrt{s_{NN}} = 5.02$ *TeV with the ATLAS detector*, CERN-EP-2016-200 (2016)